



National Library
of Canada

Acquisitions and
Bibliographic Services Branch

395 Wellington Street
Ottawa, Ontario
K1A 0N4

Bibliothèque nationale
du Canada

Direction des acquisitions et
des services bibliographiques

395, rue Wellington
Ottawa (Ontario)
K1A 0N4

Your file - Votre référence

Our file - Notre référence

NOTICE

The quality of this microform is heavily dependent upon the quality of the original thesis submitted for microfilming. Every effort has been made to ensure the highest quality of reproduction possible.

If pages are missing, contact the university which granted the degree.

Some pages may have indistinct print especially if the original pages were typed with a poor typewriter ribbon or if the university sent us an inferior photocopy.

Reproduction in full or in part of this microform is governed by the Canadian Copyright Act, R.S.C. 1970, c. C-30, and subsequent amendments.

AVIS

La qualité de cette microforme dépend grandement de la qualité de la thèse soumise au microfilmage. Nous avons tout fait pour assurer une qualité supérieure de reproduction.

S'il manque des pages, veuillez communiquer avec l'université qui a conféré le grade.

La qualité d'impression de certaines pages peut laisser à désirer, surtout si les pages originales ont été dactylographiées à l'aide d'un ruban usé ou si l'université nous a fait parvenir une photocopie de qualité inférieure.

La reproduction, même partielle, de cette microforme est soumise à la Loi canadienne sur le droit d'auteur, SRC 1970, c. C-30, et ses amendements subséquents.

Canada

UNIVERSITY OF ALBERTA

***Characterization of a High Sensitivity X-ray Resist and
Resultant Process Latitude***

BY
© RAYMOND KWOK-WAI TAM

**A thesis submitted to the Faculty of Graduate Studies and
Research in partial fulfillment of the requirements for the degree
of MASTER OF SCIENCE.**

DEPARTMENT OF ELECTRICAL ENGINEERING

EDMONTON, ALBERTA

Fall 1994



National Library
of Canada

Acquisitions and
Bibliographic Services Branch

395 Wellington Street
Ottawa, Ontario
K1A 0N4

Bibliothèque nationale
du Canada

Direction des acquisitions et
des services bibliographiques

395, rue Wellington
Ottawa (Ontario)
K1A 0N4

Votre file - Votre référence

Votre file - Notre référence

The author has granted an irrevocable non-exclusive licence allowing the National Library of Canada to reproduce, loan, distribute or sell copies of his/her thesis by any means and in any form or format, making this thesis available to interested persons.

L'auteur a accordé une licence irrévocable et non exclusive permettant à la Bibliothèque nationale du Canada de reproduire, prêter, distribuer ou vendre des copies de sa thèse de quelque manière et sous quelque forme que ce soit pour mettre des exemplaires de cette thèse à la disposition des personnes intéressées.

The author retains ownership of the copyright in his/her thesis. Neither the thesis nor substantial extracts from it may be printed or otherwise reproduced without his/her permission.

L'auteur conserve la propriété du droit d'auteur qui protège sa thèse. Ni la thèse ni des extraits substantiels de celle-ci ne doivent être imprimés ou autrement reproduits sans son autorisation.

ISBN 0-315-95120-6

Canada

UNIVERSITY OF ALBERTA

RELEASE FORM

NAME OF AUTHOR: **RAYMOND KWOK-WAI TAM**

TITLE OF THESIS: **Characterization of a High Sensitivity X-ray Resist and
Resultant Process Latitude**

DEGREE: **Master of Science**

YEAR THIS DEGREE GRANTED: **1994**

Permission is hereby granted to the University of Alberta Library to reproduce single copies of this thesis and to lend or sell such copies for private, scholarly or scientific research purposes only.

The author reserves all other publication and other rights in association with the copyright in the thesis, and except as hereinbefore provided neither the thesis nor any substantial portion thereof may be printed or otherwise reproduced in any material form whatever without the author's prior written permission

Raymond Tam

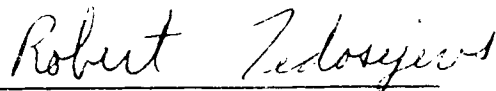
3B, Tung Tau Yuen
Old Market
Yuen Long, N.T.
Hong Kong

Date: July 22, 1994

UNIVERSITY OF ALBERTA

FACULTY OF GRADUATE STUDIES AND RESEARCH

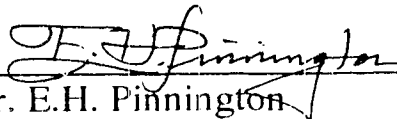
The undersigned certify that they have read, and recommend to the Faculty of Graduate Studies and Research for acceptance, a thesis entitled **CHARACTERIZATION OF A HIGH SENSITIVITY X-RAY RESIST AND RESULTANT PROCESS LATITUDE** submitted by **RAYMOND KWOK-WAI TAM** in partial fulfillment of the requirements for the degree of **MASTER OF SCIENCE** in **ELECTRICAL ENGINEERING**.



Dr. R. Fedosejevs (Supervisor)



Dr. M.J. Brett



Dr. E.H. Pinnington

Date : July 19 1994

To my parents

Abstract

This project demonstrated the feasibility of high resolution proximity x-ray lithography using a high repetition rate, excimer laser-plasma x-ray source. In this work a 20 Hz 15 μm diameter, 46 mW point source of keV x-rays has been employed. The efficiency of conversion of laser light into x-rays is approximately 2 %.

High sensitivity resists will be required in order to make laser-plasma sources competitive as production facilities for x-ray lithography. A negative resist (Shipley XP90104C) has been characterized at exposures of 1 - 30 mJ cm^{-2} in order to determine the exposure response of the resist and the appropriate sensitivity and contrast parameters to use in a modelling code (XD3) calculation of the exposure and etching process. The sensitivity of the resist is found to be on the order of 10 mJ cm^{-2} . Detailed studies are carried out to compare the lineshapes produced in the resist under a variety of exposures and mask to wafer gap distances, for 1.0, 0.25, 0.20 and 0.1 μm line feature sizes. The optimized modelling parameters are then used to calculate the allowed process window to reliably produce a lineshape of a given linewidth.

The best results obtained were the production of 0.1 μm linewidth patterns on the Shipley XP90104C resist with a height of 1.3 μm for an aspect ratio of 13:1. The resulting profile is in good agreement with the modeling calculation XD3.

Acknowledgement

I would like to take this opportunity to thank my supervisor Professor Robert Fedosejevs for his overwhelming enthusiasm, patient guidance, valuable advice and ideas, constant discussions and encouragement through this study. His success and dedication to science widen my horizon and inspire my insight.

I am particularly grateful to Dr. Romauld Bobkowski for his help in doing the exposures and valuable suggestions. I really appreciate his patient explanations, discussions, support and encouragement throughout my study. I am also grateful to Professor Mike Brett for his expertise in thin film technology.

I would like to thank Mr. Blair Harwood and Mr. Al Haromy for their excellent technical support and would like to acknowledge the help of Graham McKinnon and Glen Fitzpatrick of the Alberta Microelectronic Center in the processing of the x-ray resists.

I give thanks to Mr. George Braybrook for his help in viewing the resist profiles using the scanning electron microscope. I would also like to acknowledge the postgraduate scholarship to support my research from the Natural Sciences and Engineering Research Council of Canada.

I wish to thank my parents for their love, encouragement and understanding. Their support over years have made it possible for me to pursue graduate studies. Special thanks are due Fung-Chu Wong for tolerating the long hours. Her love and friendship has brought me much joy and has helped me through this time in my life.

Finally, I would like to thank Ying Tsui and Yanmin Li for their support and useful discussion for this study.

Table of contents

| | |
|---------------------------------------------------------------------|-----------|
| 1. Introduction | 1 |
| 2. Microlithography | 2 |
| 2.1 Semiconductor device manufacturing | 2 |
| 2.2 Lithographic Process | 3 |
| 2.3 Basic Configurations for Lithography | 4 |
| 2.3.1 Contact printing (Hard contact printing) | 4 |
| 2.3.2 Proximity printing (Soft contact printing) | 5 |
| 2.3.3 Projection printing | 9 |
| 2.4 The Physics of the Lithographic Process | 10 |
| 2.4.1 Coherence | 10 |
| 2.4.2 Luminance | 10 |
| 2.4.3 Image formation | 10 |
| 2.4.4 Diffraction | 10 |
| 2.4.5 Aberration, astigmatism and chromatic aberrations | 12 |
| 2.4.6 F number and Numerical aperture..... | 12 |
| 2.4.7 Depth of focus (Depth of field) | 13 |
| 2.5 Lithographic Strategies | 14 |
| 2.5.1 Limitation of resolution | 14 |
| 2.5.2 Backscatter Problem with Various Lithographic Strategies..... | 15 |
| 2.5.3 Advantages of X-ray Lithography | 16 |
| 3. Requirements for Proximity X-ray Lithography | 18 |
| 3.1 Introduction..... | 18 |
| 3.2 X-ray Sources | 18 |
| 3.2.1 Electron impact Sources (X-ray tubes) | 18 |
| 3.2.2 Synchrotron storage ring | 19 |
| 3.2.3 Laser plasma sources | 20 |
| 3.3 X-ray Masks | 22 |
| 3.4 Exposure Tools | 23 |

| | |
|-----------------------------------------------------------------------------------------|-----------|
| 4. Resists | 24 |
| 4.1 Resist Hierarchy | 24 |
| 4.2 Resist Requirements | 25 |
| 4.2.1 Solubility | 25 |
| 4.2.2 Adhesion | 25 |
| 4.2.3 Etch resistance | 25 |
| 4.2.4 Sensitivity | 25 |
| 4.2.5 Contrast | 26 |
| 4.2.6 Resolution | 26 |
| 4.2.7 Linewidth Control | 27 |
| 4.3 PMMA - Positive chain scission resist | 27 |
| 4.4 Negative crosslinking resists | 28 |
| 4.5 The Chemistry of two component Positive Photoresists | 29 |
| 4.5.1 Solvent | 29 |
| 4.5.2 Resin | 29 |
| 4.5.3 PAC | 29 |
| 4.6 Chemically amplified three component resists | 31 |
| 5. Simulation of X-ray Lithography Process - XD3 Modelling Code | 32 |
| 5.1 Introduction | 32 |
| 5.2 Structure of the XD3 modelling code | 32 |
| 5.3 Development Model of chemically amplified negative resists | 33 |
| 5.4 Output files of XD3 modelling code | 36 |
| 5.4.1 Output graphs and files of x-ray deposition program (xdepos) | 36 |
| 5.4.2 Output graphs and files of x-ray diffraction program (xprof) | 40 |
| 5.4.3 Output graphs of x-ray development program (xetch) | 41 |
| 6. X-ray Exposure Station | 43 |
| 6.1 Introduction | 43 |
| 6.2 KrF Laser System | 43 |
| 6.3 X-ray Emission Characterization | 45 |
| 6.4 X-ray Lithography Exposures at high repetition rate in a Helium flow target chamber | 48 |

| | |
|---------------------------------------------------------------------------------------------------|----------------|
| 7. Experimental Measurements of a Negative X-ray Resist | 51 |
| 7.1 Introduction | 51 |
| 7.2 Spincoat of the resist on the wafer | 52 |
| 7.3 Etch rate of XP90104C resist | 53 |
| 7.3.1 Experimental details | 53 |
| 7.3.2 Results | 55 |
| 7.4 Plasma etch resistance of XP90104C | 57 |
| 7.5 Contrast and Sensitivity of XP90104C | 57 |
| 7.6 Exposure measurement on XP90104C resist for contact printing | 59 |
| 7.6.1 Masks | 59 |
| 7.6.2 Experimental details | 61 |
| 7.6.3 Results for thick resists | 62 |
| 7.6.4 Results for thin resists | 65 |
| 7.7 Effect of Fresnel diffraction on the resist profile | 69 |
| 7.8 Effect of vapor prime of the wafer on the resist profile | 72 |
| 7.9 Resolution of the XP90104C | 73 |
| 8. Simulation of the experimental results and prediction of process latitude | 77 |
| 8.1 Extraction of parameters from experiment | 77 |
| 8.2 Comparison of the experimental and simulated lineshape | 78 |
| 8.3 Process Latitude for Sub-micron Pattern Replication | 82 |
| 8.3.1 Process latitude for a laser-plasma x-ray source | 83 |
| 8.3.2 Process latitude for a synchrotron x-ray source | 95 |
| 8.3.3 Discussion of the process latitude ranges | 108 |
| 8.4 Alignment Techniques | 109 |
| 8.5 Throughput calculation of the laser-plasma x-ray source | 109 |
| 8.6 Future Fabrication of 0.1 μm Surface Acoustic Wave Devices | 111 |
| 8.7 Radiation Damage | 112 |
| 9. Conclusion | 113 |
| References | 115 |

| | | |
|-------------------|-------------------------------------------------------------------------------|------------|
| Appendix 1 | Summary of operating procedures for the X-ray Lithography System | 124 |
| | A1.1 Laser System | 124 |
| | A1.2 Vacuum Chamber | 124 |
| | A1.3 Computer data acquisition system | 125 |
| | A1.4 X-ray energy at the samples | 126 |
| | A1.5 X-ray transmission program | 127 |
| Appendix 2 | Resist Exposure and Processing | 129 |
| | A2.1 Flowchart summary of the lithographic processing | 129 |
| | A2.2 Substrate Cleaning | 129 |
| | A2.3 Spincoat of the resist on the wafer | 130 |
| | A2.4 Prebake of the resist coated wafer | 131 |
| | A2.5 Exposure of the resist | 132 |
| | A2.6 Post-exposure bake of the exposed resist | 132 |
| | A2.7 Development of the Shipley 90104C resist | 132 |
| | A2.8 Measurement of the thickness of the resist | 132 |
| Appendix 3 | Explanation of Parameter files of XD3 modelling code · | 133 |
| | A3.1 Explanation for the x-ray deposition parameter file | 133 |
| | A3.2 Explanation for the x-ray diffraction parameter file | 135 |
| | A3.3 Explanation for the x-ray development parameter file | 137 |

List of Tables

Chapter 2

| | | |
|------------------|--------------------------------------------------------|-----------|
| Table 2.1 | Microprocessors currently being shipped | 2 |
| Table 2.2 | Submicrometer lithography characteristics | 17 |

Chapter 6

| | | |
|------------------|----------------------------------------------------------------------|-----------|
| Table 6.1 | Transmission of B10 filters for copper and iron spectra | 49 |
|------------------|----------------------------------------------------------------------|-----------|

Chapter 7

| | | |
|-------------------|----------------------------------------------------|-----------|
| Table 7.1. | Characteristics of Commercial resists | 76 |
|-------------------|----------------------------------------------------|-----------|

Chapter 8

| | | |
|-------------------|--------------------------------------------------------------------------------------------------------------------------------------------------------------|------------|
| Table 8.1. | Exposure and Gap Latitude in printing 0.25 and 0.1 μm using laser-plasma and synchrotron source with different biases. | 108 |
|-------------------|--------------------------------------------------------------------------------------------------------------------------------------------------------------|------------|

Appendix 1

| | | |
|-------------------|-------------------------------------------------------------|------------|
| Table A1.1 | Proportion of gas mixture in KrF laser module | 124 |
| Table A1.2 | Transmission of Helium for copper spectrum | 126 |
| Table A1.3 | Transmission of B10 filter for copper spectrum | 126 |

List of Figures

| | |
|-------------------|--------------------------------------------------------------------------------------------------------------------------------------------------------------------------------------------------------------------------------------|
| Chapter 2 | |
| Figure 2.1 | Schematic diagram of the photolithographic process 3 |
| Figure 2.2 | Light distribution profile on a photoresist surface 4 |
| Figure 2.3 | Proximity x-ray lithography 6 |
| Figure 2.4 | Geometric consideration of (a) penumbra blur, δ and (b) run-out error, Δp 7 |
| Figure 2.5 | Point source x-ray lithography 8 |
| Figure 2.6 | Projection x-ray lithography 9 |
| Figure 2.7 | Diffraction patterns for different Fresnel number N ranging from 2.0 to 0.25 11 |
| Figure 2.8 | Geometry used for definition of the numerical aperture (NA) and f/number (F) of a lens 13 |
| Figure 2.9 | Principle of phase shift mask 14 |
| Chapter 3 | |
| Figure 3.1 | Electron Impact Source (X-ray tube) 18 |
| Figure 3.2 | Synchrotron source 20 |
| Figure 3.3 | Laser-plasma x-ray source 21 |
| Figure 3.4 | X-ray lithography mask 22 |
| Figure 3.5 | Sequence of steps used in the fabrication of Si_3N_4 membrane masks .. 23 |
| Chapter 4 | |
| Figure 4.1 | Types of x-ray resist 24 |
| Figure 4.2 | Typical lithographic response or contrast plots for resists in terms of the developed thickness normalized to initial resist thickness (p) as a function of $\log_{10}(\text{dose})$ 26 |
| Figure 4.3 | Crosslinkage between polymers 28 |
| Figure 4.4 | Response of chemically amplified three component resist 31 |
| Chapter 5 | |
| Figure 5.1 | Output graph of XD3 - xmnspec.out 37 |
| Figure 5.2 | Output graph of XD3 - xlkspc.out 38 |
| Figure 5.3 | Output graph of XD3 - xprbsp.out 38 |
| Figure 5.4 | Output graph of XD3 - xmndep.out and xlkdep.out 39 |

| | | |
|------------|--------------------------------------------------------------------|----|
| Figure 5.5 | Output graph of XD3 - xprof.out | 40 |
| Figure 5.6 | Output graph of XD3 - contour plot | 41 |
| Figure 5.7 | Output graph of XD3 - resist profile at (a) 60s and (b) 120s | 42 |

Chapter 6

| | | |
|------------|-------------------------------------------------------------------------------------------------------------------------------------------|----|
| Figure 6.1 | Schematic diagram of the picosecond KrF laser system | 43 |
| Figure 6.2 | (a) Photodiode trace of the output ps pulse train (200mV, 2ns /division) (b) Streak camera trace of a single pulse in the train. | 45 |
| Figure 6.3 | Schematic diagram of target chamber and diagnostics | 45 |
| Figure 6.4 | X-ray pinhole picture of the plasma produced by the laser at normal incidence | 46 |
| Figure 6.5 | Spectra of keV x-rays from (a) Iron, (b) nickel and (c) copper | 47 |
| Figure 6.6 | Transmission of 10 cm Helium and 2B10 filter versus photon energy .. | 48 |
| Figure 6.7 | Block diagram of the component in x-ray lithography laboratory | 50 |

Chapter 7

| | | |
|-------------|-----------------------------------------------------------------------------------------------------|----|
| Figure 7.1 | Typical PBS developing time versus relative humidity | 51 |
| Figure 7.2 | Dependence of resist thickness on the spin speed for XP90104C | 52 |
| Figure 7.3 | Measurement of the resist thickness as a function of time | 53 |
| Figure 7.4 | Stylus profile monitor trace using 6 mJ cm^{-2} at (a) 25s and (b) 50s | 54 |
| Figure 7.5 | Dissolving of exposed (2 mJ cm^{-2}) and unexposed resist with time | 55 |
| Figure 7.6 | Dissolution rate as a function of surface x-ray flux for XP90104C resist | 56 |
| Figure 7.7 | Plasma etch of XP90104C resist and silicon wafer | 57 |
| Figure 7.8 | Resist height versus x-ray exposure | 58 |
| Figure 7.9 | 500 μm free standing gold bar grating (a) top view and (b) cross-section | 59 |
| Figure 7.10 | 1000 μm free standing gold bar grating (a) top view and (b) cross-section | 60 |
| Figure 7.11 | Mounting of the resist sample and mask | 61 |
| Figure 7.12 | Thick resist profile using 500 μm mask and 2.5 mJ cm^{-2} exposure flux | 62 |
| Figure 7.13 | Thick resist profile using 500 μm mask and 3.8 mJ cm^{-2} exposure flux | 62 |
| Figure 7.14 | Thick resist profile using 500 μm mask and 5.0 mJ cm^{-2} exposure flux | 63 |
| Figure 7.15 | Thick resist profile using 500 μm mask and 7.0 mJ cm^{-2} exposure flux | 63 |
| Figure 7.16 | Thick resist profile using 500 μm mask and 9.0 mJ cm^{-2} exposure flux | 64 |
| Figure 7.17 | Thick resist profile using 1000 μm mask and 7.0 mJ cm^{-2} exposure flux | 64 |
| Figure 7.18 | Thin resist profile using 1000 μm mask and 7.0 mJ cm^{-2} exposure flux | 65 |

| | | |
|---------------|-------------------------------------------------------------------------------------------------------------------------------------------------------------------------------------------------------------------------------------------------------------------------------------------------------|----|
| Figure 7.19 | Thin resist profile using 1000 $\mu\text{m}/\text{mm}$ mask and 9.0 mJ cm^{-2} exposure flux | 65 |
| Figure 7.20 | Thin resist profile using 1000 $\mu\text{m}/\text{mm}$ mask and 13.0 mJ cm^{-2} exposure flux | 66 |
| Figure 7.21 | Thin resist profile using 1000 $\mu\text{m}/\text{mm}$ mask and 15.0 mJ cm^{-2} exposure flux | 66 |
| Figure 7.22 | Thin resist profile using 1000 $\mu\text{m}/\text{mm}$ mask and 20.0 mJ cm^{-2} exposure flux | 67 |
| Figure 7.23 | Thin resist profile using 1000 $\mu\text{m}/\text{mm}$ mask and 25.0 mJ cm^{-2} exposure flux | 67 |
| Figure 7.24 | Thin resist profile using 1000 $\mu\text{m}/\text{mm}$ mask and 30.0 mJ cm^{-2} exposure flux | 68 |
| Figure 7.25 | Calculated diffraction (left) and resultant resist profile (right) patterns versus mask to wafer gap | 70 |
| Figure 7.26 | Diffraction effect for 350 μm spacing at 9 mJ cm^{-2} | 71 |
| Figure 7.27 | 0.2 μm lineshape (a) without vapor prime and (b) with vapor prime process | 72 |
| Figure 7.28 | 1 μm linewidth imprinted in Shipley XP90104C resist | 73 |
| Figure 7.29 | 0.3 μm linewidth imprinted in Shipley XP90104C resist | 74 |
| Figure 7.30 | 0.2 μm linewidth imprinted in Shipley XP90104C resist | 74 |
| Figure 7.31 | 0.15 μm linewidth imprinted in Shipley XP90104C resist | 75 |
| Figure 7.32 | 0.1 μm linewidth imprinted in Shipley XP90104C resist using a 0.7 μm thick starting thickness of resist. | 75 |
| Figure 7.33 | 0.1 μm linewidth imprinted in Shipley XP90104C resist using a 1.4 μm thick starting thickness of resist. | 76 |
| Chapter 8 | | |
| Figure 8.1 | Dissolution rate as a function of surface x-ray flux, both measured (solid circles) and calculated (hollow circles) | 77 |
| Figure 8.2 | (a) Experimentally measured 1 μm lineshape at an exposure flux of 7 mJ cm^{-2} . (b) Comparison of a digitized experimental 1 μm line profile in XP90104C resist (solid dots) with that calculated with the XD3 simulation code (solid line) | 79 |
| Figure 8.3 | (a) Experimentally measured 0.2 μm lineshape at an exposure flux of 7 mJ cm^{-2} . (b) Comparison of a digitized experimental 0.2 μm line profile in XP90104C resist (solid dots) with that calculated with the XD3 simulation code (solid line) | 80 |

Figure 8.4 (a) Experimentally measured 0.1 μm lineshape at an exposure flux of 7 mJ cm^{-2} .
 (b) Comparison of a digitized experimental 0.1 μm line profile in XP90104C resist (solid dots) with that calculated with the XD3 simulation code (solid line) 81

Figure 8.5 (a) Fresnel diffraction pattern and resultant resist lineshape at gap = 20, 50, and 80 μm and corresponding exposures of 40, 30 and 20 mJ cm^{-2} .
 (b) Exposure-gap plots of $\pm 10\%$ linewidth contours to indicate allowed operating regimes and process latitude for the printing of 0.25 μm wide lines in XP90104C resist with 0.0 μm bias. Also shown is a potential operating window with an allowed exposure range of 40 - 59 mJ cm^{-2} and a gap of 10 - 15 μm 84

Figure 8.6 (a) Fresnel diffraction pattern and resultant resist lineshape at gap = 20,50, and 80 μm and corresponding exposures of 28, 27 and 20 mJ cm^{-2} .
 (b) Exposure-gap plots of $\pm 10\%$ linewidth contours to indicate allowed operating regimes and process latitude for the printing of 0.25 μm wide lines in XP90104C resist with 0.05 μm bias. Also shown is a potential operating window with an allowed exposure range of 24.5 - 36 mJ cm^{-2} and a gap of 10 - 15 μm 86

Figure 8.7 (a) Fresnel diffraction pattern and resultant resist lineshape at gap = 20,50, and 80 μm and corresponding exposures of 17, 20 and 20 mJ cm^{-2} .
 (b) Exposure-gap plots of $\pm 10\%$ linewidth contours to indicate allowed operating regimes and process latitude for the printing of 0.25 μm wide lines in XP90104C resist with 0.1 μm bias. Also shown is a potential operating window with an allowed exposure range of 14 - 22.5 mJ cm^{-2} and a gap of 10 - 15 μm 88

- Figure 8.8** (a) Fresnel diffraction pattern and resultant resist lineshape at gap = 5, 20, and 40 μm and corresponding exposures of 32, 19 and 17 mJ cm^{-2} .
 (b) Exposure-gap plots of $\pm 10\%$ linewidth contours to indicate allowed operating regimes and process latitude for the printing of 0.1 μm wide lines in XP90104C resist with 0.0 μm bias. Also shown is a potential operating window with an allowed exposure range of 32 - 34 mJ cm^{-2} and a gap of 5 - 7 μm 90
- Figure 8.9** (a) Fresnel diffraction pattern and resultant resist lineshape at gap = 5, 20, and 40 μm and corresponding exposures of 28, 19 and 17 mJ cm^{-2} .
 (b) Exposure-gap plots of $\pm 10\%$ linewidth contours to indicate allowed operating regimes and process latitude for the printing of 0.1 μm wide lines in XP90104C resist with 0.01 μm bias. A potential operating window with an exposure range of 28 - 31 mJ cm^{-2} and a gap range of 5 - 7 μm is shown. 92
- Figure 8.10** (a) Fresnel diffraction pattern and resultant resist lineshape at gap = 5, 20, and 40 μm and corresponding exposures of 28, 18 and 16 mJ cm^{-2} .
 (b) Exposure-gap plots of $\pm 10\%$ linewidth contours to indicate allowed operating regimes and process latitude for the printing of 0.1 μm wide lines in XP90104C resist with 0.02 μm bias. A potential operating window with an exposure range of 26 - 30 mJ cm^{-2} and a gap range of 5 - 7 μm is shown. 94
- Figure 8.11.** (a) Spectrum of keV x-rays from a synchrotron 95
- Figure 8.12.** (a) Fresnel diffraction pattern and resultant resist lineshape at gap = 20, 50, and 80 μm and corresponding exposures of 100, 68 and 52 mJ cm^{-2} .
 (b) Exposure-gap plots of $\pm 10\%$ linewidth contours to indicate allowed operating regimes and process latitude for the printing of 0.25 μm wide lines in XP90104C resist with 0.0 μm bias. A potential operating window with an exposure range of 78 - 114 mJ cm^{-2} and gap range of 10 - 15 μm is shown. 97

- Figure 8.13.** (a) Fresnel diffraction pattern and resultant resist lineshape at gap = 20, 50, and 80 μm and corresponding exposures of 56, 50 and 42 mJ cm^{-2} .
- (b) Exposure-gap plots of $\pm 10\%$ linewidth contours to indicate allowed operating regimes and process latitude for the printing of 0.25 μm wide lines in XP90104C resist with 0.05 μm bias. A potential operating window with an exposure range of 40 - 74.5 mJ cm^{-2} and gap range of 10 - 15 μm is shown. 99
- Figure 8.14.** (a) Fresnel diffraction pattern and resultant resist lineshape at gap = 20, 50, and 80 μm and corresponding exposures of 37, 35 and 33 mJ cm^{-2} .
- (b) Exposure-gap plots of $\pm 10\%$ linewidth contours to indicate allowed operating regimes and process latitude for the printing of 0.25 μm wide lines in XP90104C resist with 0.10 μm bias. A potential operating window with an exposure range of 23 - 39 mJ cm^{-2} and gap range of 10 - 15 μm is shown. 101
- Figure 8.15** (a) Fresnel diffraction pattern and resultant resist lineshape at gap = 5, 20 and 40 μm and corresponding exposures of 60, 46 and 35 mJ cm^{-2} .
- (b) Exposure-gap plots of $\pm 10\%$ linewidth contours to indicate allowed operating regimes and process latitude for the printing of 0.10 μm wide lines in XP90104C resist with 0.0 μm bias. A potential operating window with an exposure range of 60.5 - 65.5 mJ cm^{-2} and gap range of 5 - 7 μm is shown. 103
- Figure 8.16** (a) Fresnel diffraction pattern and resultant resist lineshape at gap = 5, 20 and 40 μm and corresponding exposures of 56, 46 and 35 mJ cm^{-2} .
- (b) Exposure-gap plots of $\pm 10\%$ linewidth contours to indicate allowed operating regimes and process latitude for the printing of 0.10 μm wide lines in XP90104C resist with 0.01 μm bias. A potential operating window with an exposure range of 56 - 64 mJ cm^{-2} and gap range of 5 - 7 μm is shown. 105

| | |
|--------------------------------------------------------------------------------------------------------------------------------------------------------------------------------------------------------------------------------------------------------------------------------------------------------------------------------------------------------------|-----|
| Figure 8.17 (a) Fresnel diffraction pattern and resultant resist lineshape at gap = 5, 20 and 40 μm and corresponding exposures of 53, 44 and 33 mJ cm^{-2} . | |
| (b) Exposure-gap plots of $\pm 10\%$ linewidth contours to indicate allowed operating regimes and process latitude for the printing of 0.10 μm wide lines in XP90104C resist with 0.02 μm bias. A potential operating window with an exposure range of 52 - 59 mJ cm^{-2} and gap range of 5 - 7 μm is shown. | 107 |
| Figure 8.18 Outline of a basic SAW filter on a piezoelectric substrate | 111 |
| Appendix 2 | |
| Figure A2.1 Dependence of resist thickness on the spin speed | 130 |

List of Abbreviations

| Abbreviation | Full Name |
|---------------------|------------------------------------------|
| ADC | Analog to digital converter |
| ALF | Advanced lithography facility |
| AR | Anti-reflection |
| ASE | Amplified spontaneous emission |
| BCS | Beamline control system |
| CD | Critical dimensions |
| CPU | Central processing unit |
| CXrL | Center for x-ray lithography |
| DOF | Depth of focus |
| DRAM | Dynamic random access memory |
| FWHM | Full width half maximum |
| ESR | Electron storage rings |
| HMDS | Hexamethyldisilazane |
| IC | Integrated circuit |
| IPA | Isopropyl alcohol |
| LW | Linewidth |
| MIBK | Methylisobutyl ketone |
| MOS | Metal-on-silicon |
| NA | Numerical aperture of the optical system |
| PAC | Photoactive compound |
| PAG | Photoacid generator |
| PBS | Polybutene-1 sulfone |
| PC | Personal computer |
| PCMS | Polychloromethylstyrene |
| PEB | Post exposure bake |
| PMMA | Polymethylmethacrylate |
| PPM | Revolutions per minute |

| | |
|---------------|-----------------------------------------------------------------|
| SAW | Surface acoustic wave |
| SRA | Step and repeat aligner |
| SRAM | Static random access memory |
| TAP | Thallium hydrogen phthalate |
| TGS | Transmission grating spectrometer |
| ULSI | Ultra large scale integrated |
| XD3 | X-ray diffraction, deposition and development code |
| XLIMAS | X-ray lithography modelling of laser plasma sources code |
| XMAS | X-ray lithography modelling and simulation code |
| XRD | X-ray diode |
| XRL | X-ray lithography |

List of Symbols

| Symbol | Meaning | Unit |
|------------------------------|----------------------------------------------------|---------------------|
| 2w | Grating period | μm |
| a | Half linewidth | μm |
| d | Photoresist thickness | μm |
| f | Focal length of the lens | mm |
| g | mask to wafer gap width | μm |
| h | Planck's constant (= 6.6262×10^{-34}) | J s |
| k | empirical constant | |
| D | Diameter of the lens | cm |
| E | Energy | mJ |
| F | f / number | |
| Φ | X-ray flux | mJ cm^{-2} |
| L | Distance between radiation source and mask | cm |
| M | Monomer | |
| N | Fresnel number | |
| θ | Opening angle of the cone of synchrotron radiation | rad |
| S | Diameter of the radiation source | μm |
| T | Transmission | % |
| w | Linewidth | μm |
| Δg | Variation of the mask to wafer gap | μm |
| Δp | Run-out error | μm |
| γ | Relativistic energy factor; resist contrast | |
| λ | Wavelength of the exposing radiation | nm |
| δ | Penumbra blur | μm |
| η | Refractive index | |
| ν | Frequency | Hz |

Chapter 1 : Introduction

Microelectronic circuit patterns can be printed with a higher resolution and greater line density with x-ray lithography (XRL) than is possible with conventional photolithography. This high resolution is due to the virtual elimination of diffraction effects by using short wavelength (0.4 - 15 nm) x-rays rather than the longer wavelength photons (200 - 450 nm) usually employed in optical photolithography⁽¹⁾. One of the key components of the lithographic process is a radiation sensitive material called a resist which is used to transfer the pattern onto the semiconductor substrate.

A research project has been carried out to investigate the application of an x-ray source based on laser produced plasmas for x-ray lithography. One of the goals of the project was to characterize a high sensitivity resist (Shipley XP00104C) for various linewidths ranging from 1.0 μm down to 0.1 μm . It involved an intensive study of the effects of various parameters such as exposure dose, development time and the separation distance between mask and wafer on the linewidth control. Parameters found from these studies were used as input data for an x-ray lithography modelling code developed at the University of Alberta called XD3. The predicted process latitude of the tested resist using a laser-plasma x-ray source is then compared with that of the same resist using a synchrotron x-ray source. The x-ray source used in the exposure is the University of Alberta laser-plasma x-ray source developed by Professor R. Fedosejevs.

Once the x-ray resist has been characterized in terms of its sensitivity and contrast, it can be assessed to determine if it can have reasonable throughput which is one of the main issue in x-ray lithography employing laser-plasma sources. As very large scale integrated (VLSI) circuitry becomes more and more complex, fabrication of feature sizes of 0.2 μm or less is required. The investigation of the resolution of a high sensitivity resist is another goal of this project so as to determine if it can meet these future linewidth requirement.

In the rest of this thesis, a review of microlithography will be given, followed by an outline of proximity x-ray printing and resist technologies, a detailed description of the research project including the modelling code, exposure station, resist processing, experimental results, relevant parameters extracted from the experiments, simulation of the experimental results and prediction of process latitude. Discussion of the results and conclusions of this thesis will be presented at the end. Summaries of the operation of the laser system and resist processing are included in appendices 1 and 2. Details of the input parameter files for the modelling code XD3 are given in appendix 3.

Chapter 2 : Microlithography

2.1 Semiconductor device manufacturing

In microelectronic fabrication, complex circuits are built into and on the surface of a semiconductor substrate such as silicon in a succession of process steps. These circuits are defined by a lithographic process⁽²⁾ in which the desired pattern is first generated in a radiation sensitive resist layer (usually a polymeric film $\sim 0.5 - 1.0 \mu\text{m}$ thick which is spin-coated onto the substrate). After developing the resist to give the desired pattern, the pattern is then transferred, via techniques such as etching, ion implantation and/or diffusion, to the underlying substrate. Similar processes are used for patterning the metal layers to interconnect the semiconductor devices. The definition of the features in the resist layer is achieved by exposing the resist to some suitable form of patterned radiation such as ultraviolet light, electrons, x-rays or ions.

Photoresist materials can be classified as either positive or negative tone according to their response to light. A positive-tone photoresist dissolves more readily in solvents in exposed regions than in unexposed regions, whereas in negative resists, the exposed region remains insoluble and the background is dissolved away.

Microminiaturization has made it possible to employ millions of transistors in a single circuit. For example, the dimension of a metal-on-silicon (MOS) device have shrunk from $5.0 \mu\text{m}$ in 1975 to $0.6 \mu\text{m}$ currently^(3, 4). Today these techniques have advanced towards the production of very large scale integrated (VLSI) circuits with 10^6 transistors on a chip and ultra large scale integrated (ULSI) circuits with $> 10^8$ transistors per chip will appear within the next decade. The benefit of the size reduction is the reduction in cost per circuit element and the increase in the speed of operation. The current state of the art for central processing unit (CPU) chips is shown in table 2.1.

| Microprocessor | Company | Transistors (millions) | Linewidth (μm) | Die size (mm) | Clock speed (MHz) |
|----------------|-----------------------------------------|-----------------------------|--------------------------------|--------------------|------------------------|
| Super Sparc | Sun Microsystems / Texas Instruments | 3.1 | 0.7 | 16×16 | 60 |
| Pentium | Intel Corp. | 3.1 | 0.8 | 17.2×17.2 | 66 |
| Alpha 21064 | Digital Equipment Corp. | 1.68 | 0.68 | 15.3×12.7 | 200 |
| PowerPC 601 | IBM / Motorola | 2.8 | 0.65 | 11×11 | 80 |

Table 2.1 : Microprocessors currently being shipped⁽⁴⁾

2.2 Lithographic Process

The term microlithography is used to describe the lithographic process of making micrometer-sized electronic devices. Semiconductor lithography is concerned with the production of electronic components based on thin films ($\leq 1.0 \mu\text{m}$ in thickness).⁽⁵⁾

The general lithographic process is comprised of the following elements:

1. Exposure to radiation (light, x-rays, electrons or ions);
2. A means of patterning the radiation (shadowgraphic mask, optical imaging or direct beam steering);
3. A resist material whose removal rate depends on exposure to radiation;
4. A developing process to remove resist from the patterned area;
5. An etching or ion doping process.

The basic steps of the lithographic process based on contact or proximity printing are shown schematically in Figure 2.1⁽⁶⁾.

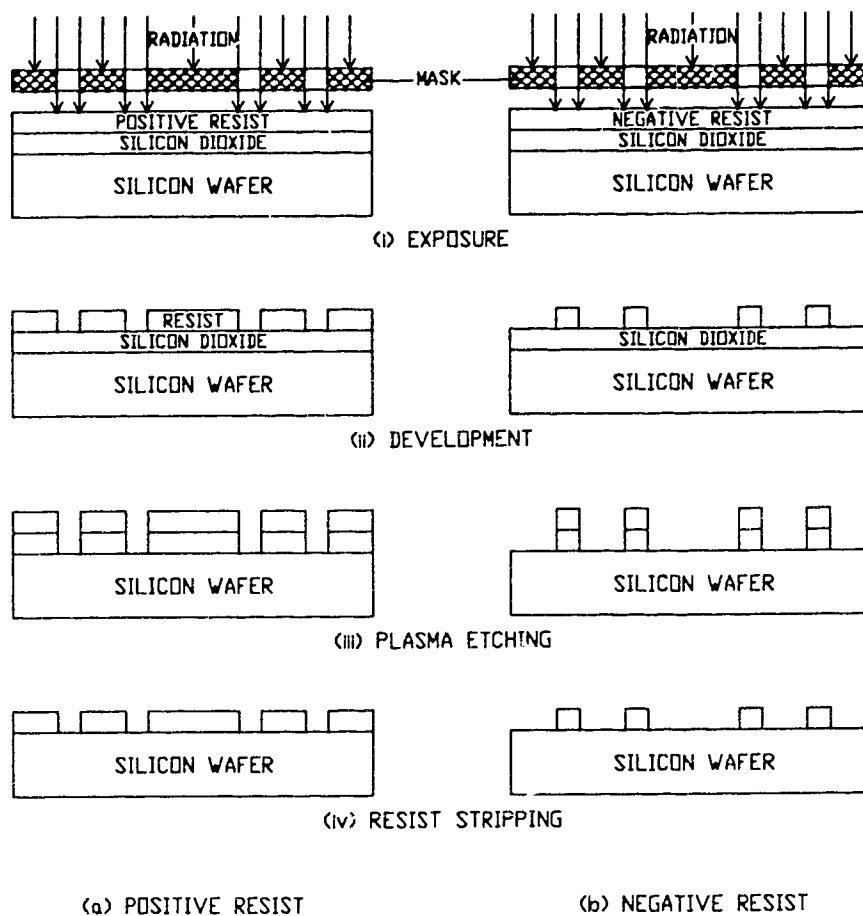


Figure 2.1. Schematic diagram of the photolithographic process.

2.3 Basic Configurations for Lithography

There are three basic configurations for lithography as outlined in the following sections.

2.3.1 Contact printing (Hard contact printing)⁽⁷⁾

Contact printing involves holding a mask just off the wafer surface and visually aligning the mask to the previous pattern on the wafer. After the alignment is achieved, the mask is pressed into hard contact with the resist coated wafer which is then exposed through the mask with a flood beam of ultraviolet light.

The primary resolution limitation of such shadowgraphic printing is diffraction of light at the edge of an opaque feature on the mask as the light passes through an adjacent clear area. This depends on the wavelength of the radiation, the width of the pattern and the remaining gap, g , between the mask and resist. A typical intensity distribution of light incident on a photoresist surface after passing through a mask consisting of opaque and transparent lines or spaces of equal width, w , and gap distance, g , is shown in Figure 2.2.

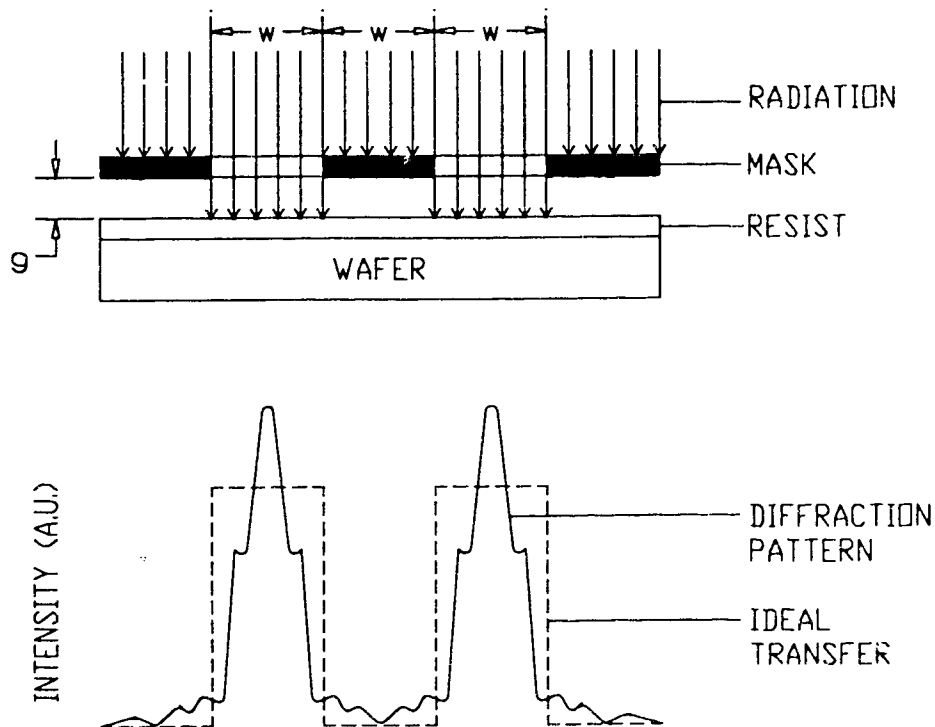


Figure 2.2. Light distribution profile on a photoresist surface.

Diffraction causes the image of a perfectly delineated edge to become blurred or diffused at the resist surface. The theoretical resolution capability of shadowgraphic printing with a mask consisting of equal lines and spaces of width w is given by

$$2w_{\min} = 3\sqrt{\lambda(g + \frac{1}{2}d)} \quad (2.1)$$

where $2w$ = grating period ($1/2w$ = spatial frequency)

g = gap width (= 0 for hard contact printing)

λ = wavelength of the exposing radiation

d = photoresist thickness

For contact printing, g is close to 0 and thus provides the highest resolution.

The advantages of contact printing are the following: it yields the highest resolution with the lowest total cost since both the equipment and process are simple, and throughput is large. The primary disadvantage is low yield caused by damage to the mask from repeated forceful intimate contact between the resist and mask.

The maximum resolution capability is seldom achieved because of other consideration such as resist swelling, difficulty in alignment, and debris between mask and wafer. The lack of flatness in either mask or wafer can create in-plane distortion on contact leading to misalignment errors and thereby degrading further the useful resolution capability of the technique.

2.3.2 Proximity printing (Soft contact printing)

The mask used to expose the circuit pattern is placed very close to the photoresist and the exposure is made in the manner of a contact print. This minimizes mask/wafer damage caused by contact, but at the expense of resolution⁽⁸⁾ by diffraction which increases rapidly with mask-to-resist spacing as given by equation 2.1. The key components of a proximity x-ray lithography system are illustrated in Figure 2.3.

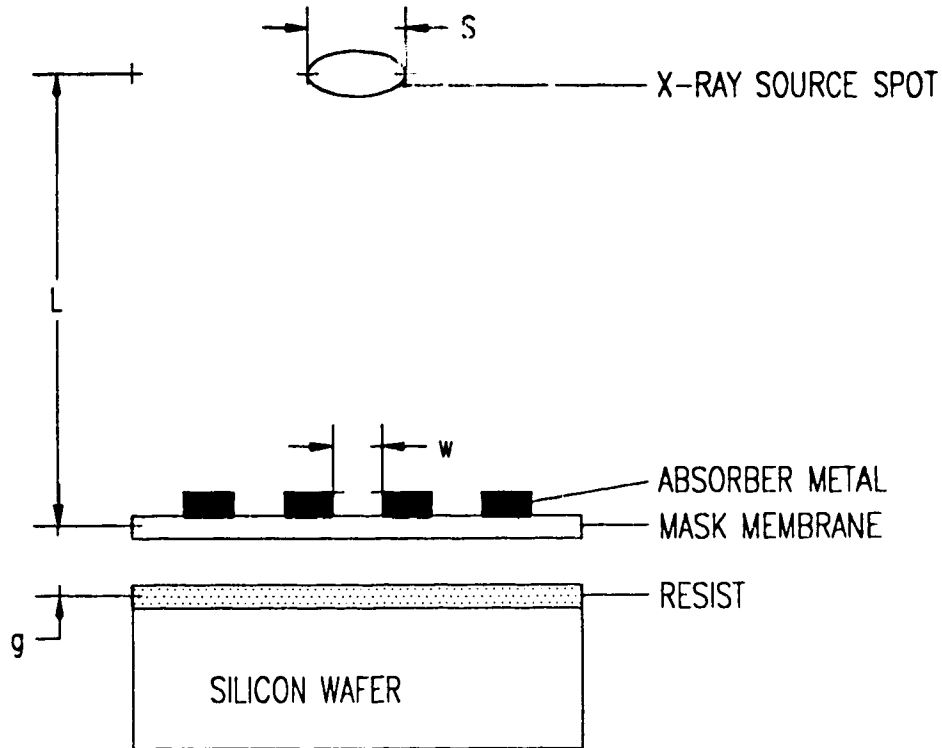


Figure 2.3. Proximity x-ray lithography.

For the x-ray lithography process, the radiation source is located at a relatively large distance, L , away, on the order of $L = 5 \text{ cm}$ to 5 m , depending on the source size S . The mask is made of a thin membrane of silicon, silicon nitride, silicon carbide or related material. The thickness of this substrate is $1 - 2 \text{ }\mu\text{m}$ to give about 50 % transmission of the 1-2 keV photon energy x-rays. A thin layer of the order of $0.3 - 1.0 \text{ }\mu\text{m}$ of high atomic number metal such as gold or tungsten is used as the absorber material on the mask to give the desired opaque region.

For any gap the minimum transferable period is approximately given by

$$2w_{\min} \approx 3\sqrt{g\lambda} \quad (2.2)$$

Proximity printing using x-rays requires a small and very constant spacing, typically on the order of $g = 5 - 50 \text{ }\mu\text{m}$, which can be achieved only with extremely flat wafers and masks⁽⁷⁾.

Point-source XRL is the simplest form of x-ray proximity lithography and has achieved very high resolution (30 nm feature size)^(9, 10, 11). However, the geometric size of the source gives an image of the source demagnified by the factor g/L on the wafer plane as shown in Figure 2.4(a). The overlay of all such images from the line pattern gives the final image on the wafer which will have a central region of uniform exposure and edge regions where the exposure falls off, called penumbra blur, which is given by the demagnified source size, δ . Furthermore, the source divergence causes pattern overlay to depend on precise control of mask-to-substrate gap as shown in Figure 2.4(b). The penumbra blur due to finite source size is given by equation (2.3) and run-out error due to variations of the proximity gap is given by equation (2.4).

$$\text{Penumbra blur: } \delta = \frac{g}{L} \times S \quad (2.3)$$

$$\text{Run-out error: } \Delta p = \left(\frac{R+r}{L} \right) \Delta g \quad (2.4)$$

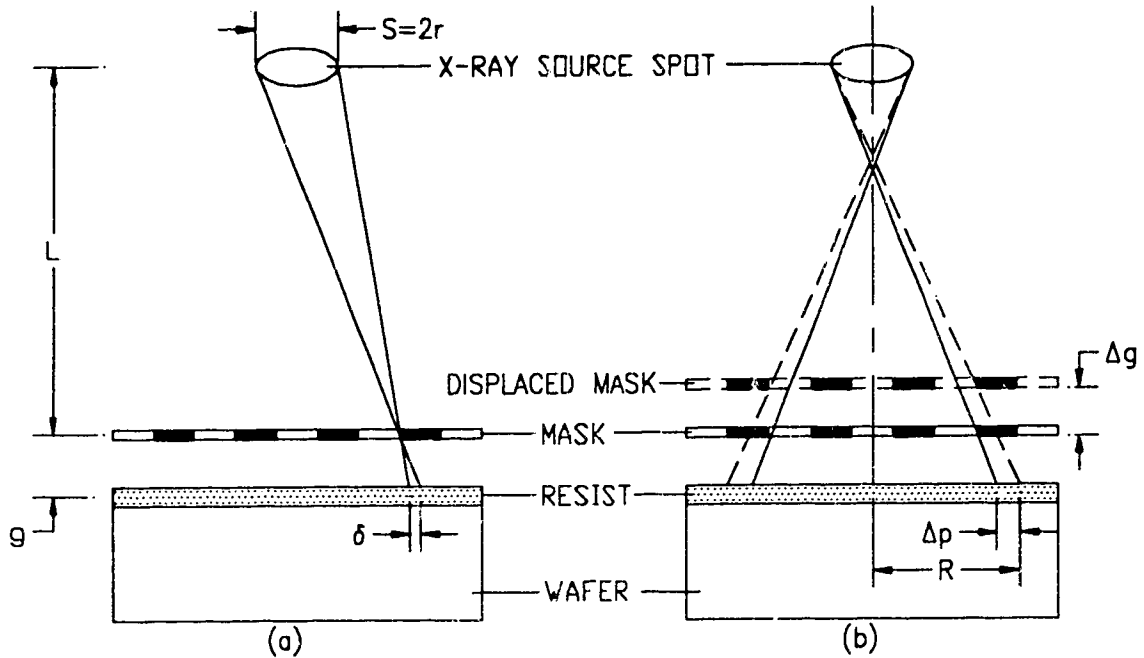


Figure 2.4. Geometric consideration of (a) penumbra blur, δ and (b) run-out error, Δp .

A point source can be collimated as depicted in Figure 2.5(b), by various techniques such as

(1) with a multilayer paraboloid^(12, 13, 14), or

(2) by grazing incidence reflection from a nested array of glass tubes^(15, 16).

None of these techniques has been fully developed yet to give the required throughput efficiency or uniform x-ray flux distribution.

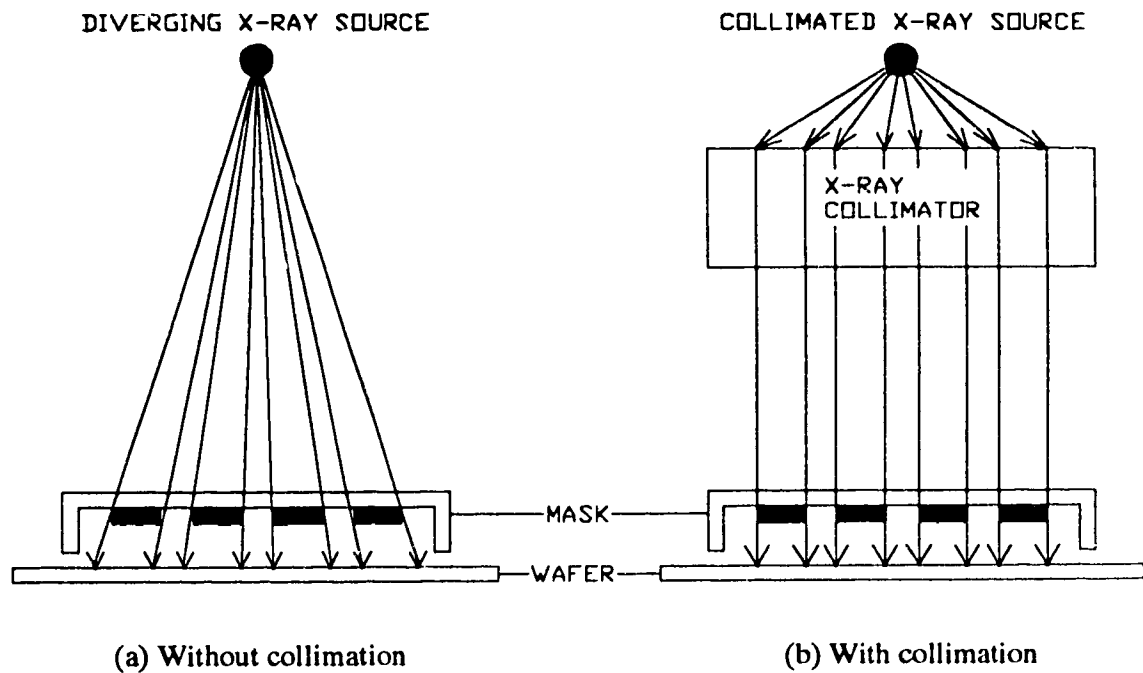


Figure 2.5. Point source x-ray lithography.

2.3.3 Projection printing

In traditional projection printing using visible or ultraviolet radiation, lens elements are used to focus the mask image onto a wafer substrate which is separated from the mask by many centimeters. Because of lens imperfections and diffraction considerations, projection techniques generally have lower resolution capability than that provided by shadow printing⁽⁷⁾.

Projection x-ray lithography uses x-ray radiation in the wavelength range of 10 nm to form the exposure image^(8, 17-20). Because of the lack of refractive optics for x-ray radiation in the range of 10 nm, optical systems for x-ray projection printing are based on reflective optics.

The design shown in Figure 2.6 is similar to conceptual designs from the Sandia National Laboratory and from the Livermore National Laboratory in USA. Reflection from the several surfaces requires multilayer dielectric mirrors. Reasonable reflection efficiency can be achieved only at wavelengths of 13 nm or greater at the present time⁽²¹⁾.

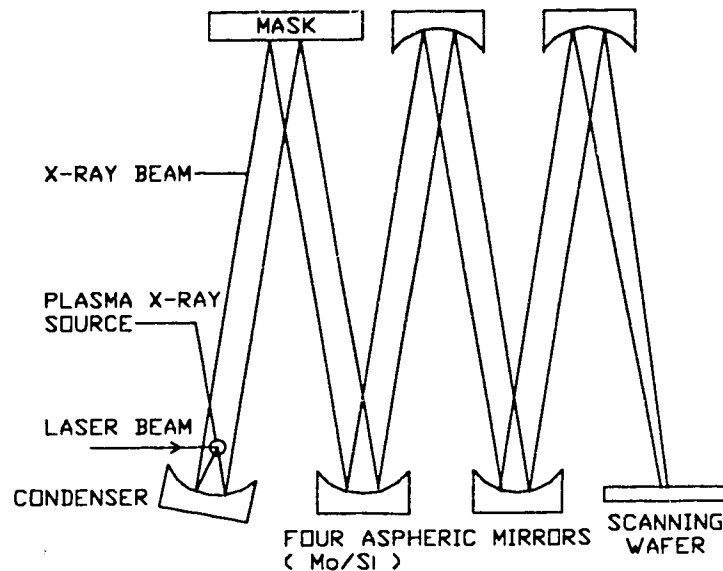


Figure 2.6. Projection x-ray lithography.

The resolution of a projection system is given by the relationship:

$$\text{minimum feature size: } w = \frac{k\lambda}{NA} \quad (2.5)$$

where k = empirically determined constant ranging from 0.6 to 0.8

λ = exposing radiation wavelength

NA = numerical aperture of the optical system

2.4 The Physics of the Lithographic Process⁽⁷⁾

The following outlines the important terms and theory commonly used in the lithographic process:

2.4.1 Coherence

The coherence of the radiation source falls into two categories.

Temporal coherence refers to photons that are related to each other in time, i.e. they are emitted with a well defined phase relation in time relative to photons which are emitted earlier or later.

Spatial coherence refers to the phase relationship of one photon to another at different points across the wavefront. A spatially coherent source is one whose photons are in phase at every point along any wavefront with the phase of the wave being described by a uniform mathematical function at any positions. For incoherent sources the traditional means of achieving coherency requires passing the light through a small pinhole and observing the wavefront at a large distance from the pinhole. Therefore, achieving perfect coherency reduces the intensity to zero and would require infinite exposure time. Fortunately, we do not require coherency for lithography and in fact do not want interference structures produced by coherent beams.

2.4.2 Luminance

Luminance for a finite source is defined as power per unit area per unit solid angle.

2.4.3 Image formation

The optical quality of the image is evaluated in terms of resolution (minimum size of object that can be imaged), contrast and size of the useful image field.

2.4.4 Diffraction

The bending of light around an obstacle is called diffraction. The resulting intensity distribution observed depends upon whether we are viewing the diffraction pattern under conditions where the source and /or screen on which the pattern is displayed, are located a short distance from the slit (Fresnel diffraction) where the pattern arises from interference of many spherical wavefronts or at large distance (Fraunhofer diffraction) where the pattern arises from interference of a number of planar wavefronts. The diffraction effect in shadowgraphic printing falls into the Fresnel class since the mask (slit) and wafer (screen) are separated by only a very short distance.

A mask consisting of lines and spaces constitutes a diffraction grating and when illuminated will produce a diffraction pattern. The diffraction from any source can be calculated by Huygen's principle with the summation of wavelets from every point of the secondary wavelet.

For an x-ray source located a large distance from the mask, the shape of the diffraction pattern is governed entirely by the Fresnel number N which gives the number of Fresnel zones subtended by the aperture. This is given by the equation (2.6).

$$N = \frac{a^2}{g\lambda} \quad (2.6)$$

where $a = w/2$ is the half linewidth for a slit pattern or radius in the case of a circular pattern, g is the mask to wafer gap and λ is the wavelength of the exposing radiation.

Plots of lineshapes as a function of Fresnel number are shown in Figure 2.7 for four equispaced slits as calculated using the XD3 code as presented later in chapter 5.

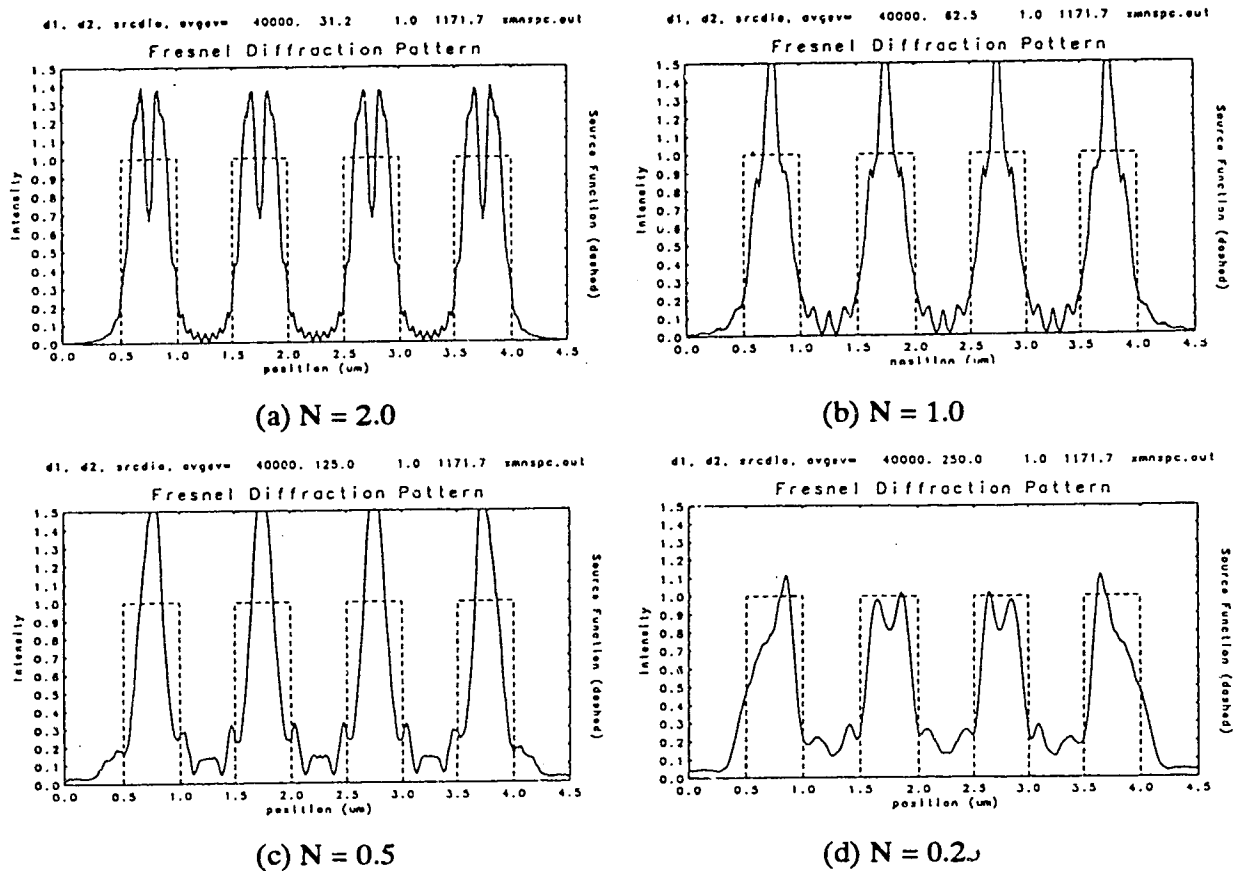


Figure 2.7. Diffraction patterns for different Fresnel number N ranging from 2.0 to 0.25.

It can be seen from Figure 2.7 that as N decreases the slope at the edge becomes less and more power diffracts into the shadow regions between the slits leading to lower contrast. The Fresnel number should be chosen to give good edge slope definition and very little energy spread outside of the desired linewidth. Also as seen above, the diffraction patterns have their half intensity points inside of the mask linewidth. If the exposure intensity which demarks where the resist is removed and where it remains is half of the illumination intensity then for each Fresnel number N the mask linewidth must be bigger than the desired final pattern linewidth by a certain fractional amount. This is called biasing the mask pattern. The amount of biasing depends on the Fresnel number and exposure level chosen for the resist.

2.4.5 Aberration, astigmatism and chromatic aberrations

Aberration is a defect in the image forming capability of a lens or optical system. Astigmatism is a lens aberration that causes off-axis light bundles to focus to vertical and horizontal lines at different positions along the optic axis leading in general to an elliptical, rather than circular, spot. Chromatic aberration is where light of different wavelengths images at slightly different focal planes leading to blurring of the image if a broadband source is employed.

2.4.6 *F number and Numerical aperture*⁽²²⁾

Lenses are characterized by their focal length f and their f /number F or numerical apertures (NA). The f /number and NA of a lens are defined in Figure 2.8 for an object in a medium of refractive index η

$$NA = \eta \sin \theta \quad (2.7)$$

$$F = \frac{S}{D} \quad (2.8)$$

They are related by

$$NA \sqrt{4F^2 + 1} = \eta \quad (2.9)$$

$$\text{or } 2NA \times F \approx \eta \quad (2.10)$$

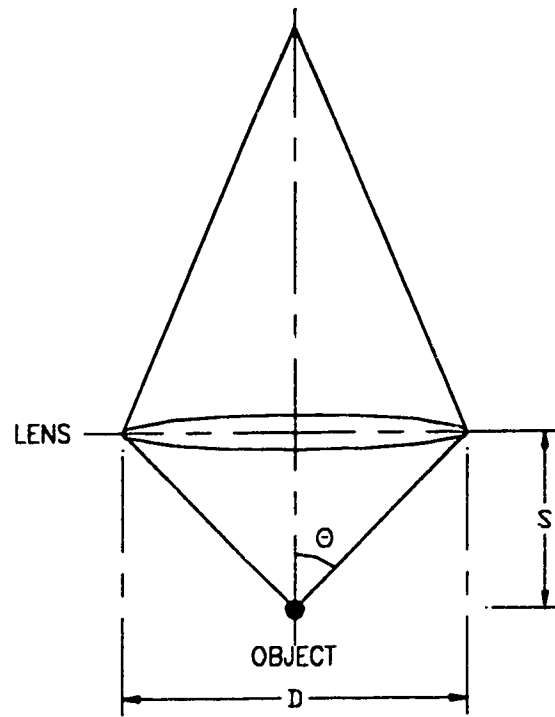


Figure 2.8. Geometry used for definition of the numerical aperture (NA) and f /number (F) of a lens.

NA is thus a quantitative measure of the " acceptance " angle of a lens. The larger the NA of the projection lens, the greater is the amount of diffracted information that can be collected and subsequently imaged leading to higher resolution.

2.4.7 Depth of focus (Depth of field)⁽²²⁾

Depth of focus (DOF) is the range over which an optical instrument will produce a distinct image of an object. For projection optics:

$$DOF = \frac{\lambda}{2(NA)^2} \quad (2.11)$$

From equation (2.11), resolution gains through the use of high NA optics or shorter wavelengths have a deleterious effect on the depth of focus.

2.5 Lithographic Strategies

2.5.1 Limitation of resolution

There are different types of lithography such as optical lithography, ion-beam lithography, electron-beam lithography and x-ray lithography depending on the type of radiation used in exposing the resist^(23, 24). The major limitation in the resolution of each type is due to the diffraction of the radiation given by equation 2.5. Thus the minimum resolvable feature size is proportional to the wavelength of the exposing radiation. Hence, it should be possible to improve the resolution by decreasing the wavelength.

In order to improve the resolution of optical systems another new technique called phase shifting has been under development over the last several years. By introducing 180° phase shifted light on the opaque side of a given line edge (rim shifter) or by alternating by 180° phase shift for successive lines in a grating line pattern (Levenson shifter)^(25, 26) the phase shifted light will cancel out the diffracted light which spills over into the opaque image region giving a much sharper line edge image than could otherwise be obtained. This requires the fabrication of a transparent layer of thickness $t = \frac{\lambda}{2(\eta - 1)}$, where λ is

the wavelength of the exposure light and η is the refractive index of the transparent layer, with a phase shift of 180° on the mask in addition to chrome line patterns. Such techniques have been applied in research work where the effect has been to reduce the allowed k value in the resolution equation 2.5 to the order of $k \sim 0.4$. This effect is illustrated in Figure 2.9.

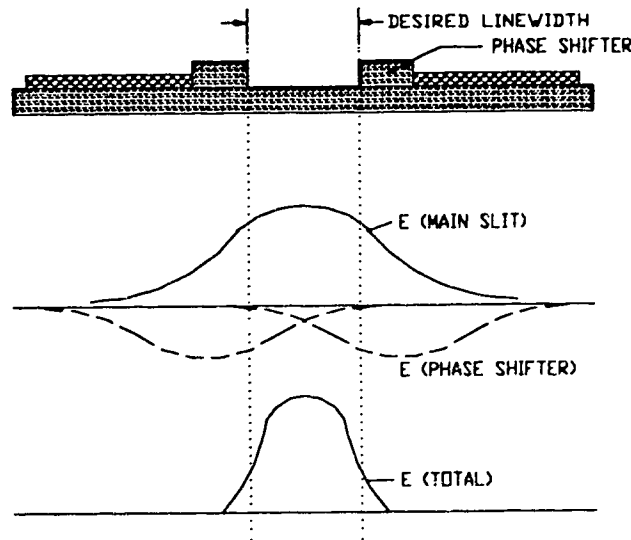


Figure 2.9. Principle of phase shift mask.

2.5.2 Backscatter Problem with Various Lithographic Strategies

Optical lithography uses state of the art imaging systems to form a demagnified image of the mask or reticle onto the resist layer. It is being used to make advanced IC chips, with 0.35 μm geometries in research, and 0.5 μm in production. However, the reflection of light from an underlying metal layer causes standing wave patterns in the exposed resist. These standing waves lead to substantial rippled side walls on the developed resist patterns which in turn leads to poor control of final patterned linewidths. The reflection problem can be addressed by depositing an anti-reflection (AR) coating⁽²⁷⁾ on the wafer prior to the resist coating which costs extra time and expense in processing.

Electron-beam lithography, in which electrons trace a pattern in photoresist, can achieve high resolution and resolve details as small as 0.01 μm . But it is slow (wafer throughput is low) for mass production and the equipment is expensive. (An electron-beam lithography machine costs about US \$4 - \$5 million, a high resolution optical lithography machine costs about \$1.6 million.) It is primarily suitable for making masks and test devices to be replicated by either optical or x-ray lithography. Electrons also tend to scatter in the photoresist and wafer substrate during patterning - causing what is called the proximity effect, where dense patterns become distorted unless proximity correction techniques are used.

Ion-beam lithography has also been pursued as a potential submicrometer lithography system. Because ions are more massive than electrons, they scatter much less and therefore require virtually no proximity corrections, providing inherently better resolution than electron-beam lithography. However, ion-beam lithography is used only in research and development work because of the slow throughput, lack of readily available, reliable ion sources and the greater maturity of competitive electron-beam equipment.

Scattering of x-ray photons at an interface depends on the index of refraction mismatch, essentially the impedance mismatch. The index of refraction , η , has two terms, a real part, $n(\lambda)$, which expresses the change in wavelength inside matter, and an imaginary part, $k(\lambda)$, which expresses attenuation with distance:

$$\eta(\lambda) = n(\lambda) + i k(\lambda) \quad (2.12)$$

In the x-ray regime all materials have η very close to 1. This means that we cannot make refractive optical elements for x-rays. However, this also means that with x-rays we can get absorption in resist without reflection or scattering⁽⁹⁾. Thus, they require no proximity corrections and x-ray lithography overcomes many of the above mentioned limitations.

2.5.3 Advantages of X-ray Lithography⁽²⁸⁾

X-ray lithography (XRL) has very high resolution due to its short wavelength and high contrast aerial image. XRL is able to resolve 0.1 μm geometries when using a 10 μm proximity printing gap. To obtain high resolution, optical lithographers have pursued shorter wavelength exposure light. It will lead to smaller linewidth due to reduced diffraction, but these wavelengths are also more readily absorbed by any material. It means that any particulates on the reticle or wafer will absorb the exposure light and be printed into the photoresist, resulting in defects. X-rays of about 1 nm wavelength are absorbed weakly in many submicron particles because of the high penetration of x-rays and will print fewer such defects.

With XRL, the control of critical dimensions (CD) is straightforward. Because of the very high contrast aerial image in a typical x-ray exposure and the uniform exposure from top to bottom of the resist layer, the transition between unexposed and exposed photoresist is very sharp, leading to near-vertical photoresist sidewall slope with high aspect ratio. This high contrast exposure also gives rise to a wide tolerance in development parameters with little effect on linewidth. This degree of uniformity and control of small CDs is potentially better than optical lithography, where small changes in exposure or development parameters can lead to unwanted changes of 100 nm or more in linewidths.

Another technical advantage of XRL over optical lithography is field size. Most optical steppers have used field sizes with diagonal measurements between 22 and 28 mm. Predictions for advanced optical steppers indicate a future diagonal field measurement of about 33 mm. In contrast, synchrotron-based XRL has long been working with diagonal field measurements in excess of 35 mm, with dimensions expected to increase to 55 mm diagonal within a few years.

In summary, x-ray lithography has the following advantages:

1. high resolution with large depth of focus using simple resist schemes,
2. transparency of defects,
3. excellent linewidth control, and
4. large field size.

Thus, x-ray lithography is predicted to be the required technique for future nano-devices fabrication. However, the only available x-rays sources with high exposure fluxes are synchrotron sources which are quite expensive (more than \$ 40 M)⁽²⁹⁾. Therefore, there is a clear need for cheaper x-ray sources for small and medium scale ULSI production facilities. This requirement can be met using a laser-plasma source to convert

laser energy into x-ray energy. The resist used must have high sensitivity for reasonable throughput in order to be competitive as an industrial facility.

A comparison of the different lithographic strategies is summarized in table 2.2⁽³⁰⁾.

| System | Source | Wavelength / energy | Resolution (μm) | Limitations |
|--------------------------------|-------------------------------------------------|--------------------------------------------------|------------------|---------------------------------------------------------------------------------------------------------------|
| Optical projection | - g-line - i-line - mid UV. - deep UV. | 436 nm 365 nm 290 - 350 nm 200 - 290 nm | 0.20 | - AR coatings required - phase shift masks required to improve resolution - sensitive to submicron dust |
| Electron beam | electrons | 1 - 50 keV | ≤0.01 | - slow |
| Ion beam | ions | 100 keV | ≤0.01 | - slow |
| X-ray proximity and projection | x-ray | 0.4 - 15.0 nm | 0.02 | - yet to be proven - masks/alignment |

Table 2.2 : Submicrometer lithography characteristics

The final choice as to which strategy will be adopted will depend not only on the capabilities in terms of performance, resolution and registration accuracy, but also on the cost effectiveness involved in manufacturing integrated circuits.

Chapter 3 : Requirements for Proximity X-ray Lithography

3.1 Introduction

In 1972, Spears and Smith demonstrated that one could obtain high resolution patterns using x-ray proximity printing and suggested that this technique could be used for high throughput, high resolution semi-conductor device fabrication⁽³¹⁾.

The basic idea of x-ray lithography (XRL) is to reduce the diffraction effects (relative to photolithography) by shortening the wavelength. A simple analysis of the absorption of x-rays shows that for lithography one must work with x-rays that are much softer than those used in x-ray diffraction or medical x-ray analysis. X-ray proximity lithography is generally considered to cover the wavelength range 0.4 to 2 nm.⁽³²⁾

An x-ray lithography system consists mainly of four components⁽³³⁾:

1. a high power x-ray source,
2. an x-ray mask,
3. an x-ray sensitive resist material, and
4. the exposure tool (which also includes the mask-wafer alignment subsystem).

The design of an x-ray lithography system must consider all the components working together.

3.2 X-ray Sources^(34, 35, 36)

Present XRL sources in the 0.4 - 2 nm wavelength range, may be classified under three general categories:

3.2.1 Electron impact Sources (X-ray tubes)

These devices consist of a source of electrons, a gap, and a target as shown in Figure 3.1.

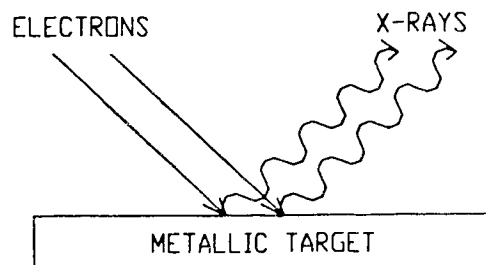


Figure 3.1. Electron Impact Source (X-ray tube).

The electrons may be ejected from the source (cathode) by thermal or field-emission effects, with heated filaments being most common. The gap, across which a high (keV) potential is applied to accelerate the electrons, is in a vacuum of at least 10^{-5} torr. The x-ray source size (anode target area) is typically a few mm^2 , depending on the electron focusing in both the source and the gap. Spectral intensities depend on the electron energy and current, the anode material, and the viewing angle from the target. The absolute x-ray intensity from a given focal spot is limited by space charge effects at low voltages ($< 1 \text{ kV}$) and by anode heat dissipation at higher voltages ($> \text{few keV}$).

The energetic electrons produce uncollimated x-rays in the anode by two basic mechanisms:

- (i) bound-to-bound electron transitions, which follow the production of core-hole vacancies, give x-ray lines, and
- (ii) free-to-free transitions, which are due to the acceleration of incident electrons in the coulomb field of the nucleus (electronic bremsstrahlung), yielding the x-ray continuum.

Electron impact sources are inefficient with most of the input energy producing heat and only about 0.1 % or less of the incident electron energy is converted into x-ray line and continuum energy. Using aluminum anodes the emission consists of the Aluminum K_α line at 0.834 nm and Bremsstrahlung background. The most powerful sources to date have been built with water cooled rotating Palladium anodes producing L_α radiation at 0.437 nm.

The main advantages of such sources are their relative simplicity and low cost. The main disadvantages are limited anode lifetime of ~ 1000 hours and limited source brightness giving exposure flux $< 5 \mu\text{W cm}^{-2}$.

3.2.2 Synchrotron storage ring⁽³⁷⁾

A synchrotron is a cyclic accelerator which uses a constant-frequency electric field and a changing magnetic field. An increasing magnetic field strength H compensates for the relativistic increase in mass at high energies to maintain a constant angular frequency of the charged particle since the angular frequency is given by $\omega = qH/m$, where q , m are the charge and mass of the particle. While the magnetic field is increasing, a high frequency electric field is applied across a gap in a metallic cavity inside the circular vacuum tube. The frequency is in synchronism with the constant angular frequency of the particles, which are accelerated while in the cavity.⁽³⁸⁾

Radiation produced by the curved motion of energetic electrons in a magnetic field is called synchrotron radiation⁽³⁹⁾ as shown in Figure 3.2. The opening angle of the cone of

radiation is given by $\theta \approx \gamma^{-1}$ where γ is the relativistic energy factor given by $\frac{E_e}{mc^2}$ where E_e is the electron energy. The electrons moving at relativistic energies of the order of 700 MeV produce x-rays with a wide wavelength spectrum. The x-rays emanate from a relatively small source region given by the electron beam (≈ 1 mm) in a horizontal fan with a very small vertical divergence. The x-ray beam that reaches the mask/wafer assembly at the end of a long beam line (10 m) is usually collimated by a grazing incidence mirror giving an approximately rectangular but slightly curved beam. Conventional storage rings using normal magnets are very large (> 15 m in diameter), and may not be very attractive for an IC production environment. Presently, superconducting magnet, compact storage rings of less than 5 m in diameter, suitable for production of ICs, have been developed in England and Japan.

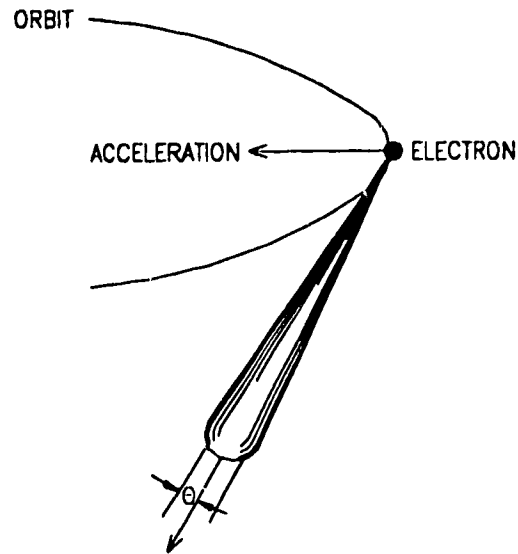


Figure 3.2. Synchrotron source.

3.2.3 Laser plasma sources

Laser plasma sources, generate x-rays by heating a solid target with very short pulses (femtoseconds - nanoseconds) from a high power laser to achieve $10^6 - 10^7$ K temperatures ($kT \sim 300 - 500$ eV) and produce ionization. A key advantage of the laser plasma source is its x-ray wavelength tunability which can enhance the contrast of a mask/resist combination by a convenient choice of the target atomic number⁽⁴⁰⁾. The setup is as shown in Figure 3.3.

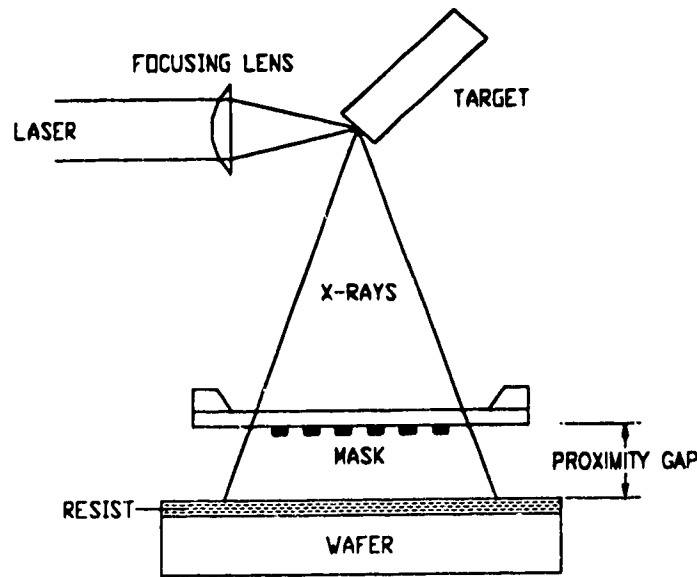


Figure 3.3. Laser-plasma x-ray source.

The x-ray output performance falls between that of conventional electron impact and the storage ring sources. One of the characteristics of these sources is a relatively small spot size (≤ 0.2 mm).

X-ray emission from multimillion degree plasmas is due to three mechanisms⁽⁴¹⁾:

- (i) bound-to bound transitions, which give discrete lines,
- (ii) free-to-bound, or recombination, transitions, which yield continua,
- (iii) free-to-free, or bremsstrahlung, transitions, which yield a continuum.

X-ray Spectra from hot plasmas vary widely, depending on the relative importance of the three mechanisms in a particular source which in turn depend on the plasma composition, geometry and details of the plasma heating.

Considerable enhancement of emission can be obtained by choosing a closed ion shell for the emitting species in the plasma. For example, copper targets ($A = 29$) can be ionized to a charge state $Z = +19$ leaving 10 attached electrons. This forms a neon-like ion with a closed 2p orbital. There are many emission lines of the excited states of 2p electrons with energies in the range of 1150 eV. Collisional excitation of these emission lines in the hot plasma leads to efficient generation of keV x-ray emission.

The main problems with such sources involve:

- (i) developing a high average power laser capable of operation at high repetition rates
- (ii) debris generating from the hot spot at the target⁽⁴²⁾.

High average power excimer lasers exist commercially up to the 200 W level. If efficiently extracted in short pulse trains as discussed later these would potentially make useful sources. Debris can be stopped by a background helium gas atmosphere and thin plastic windows.

3.3 X-ray Masks

The x-ray mask consists of an x-ray absorber pattern deposited on a thin x-ray transparent substrate which is supported by a rigid frame, shown schematically in Figure 3.4.

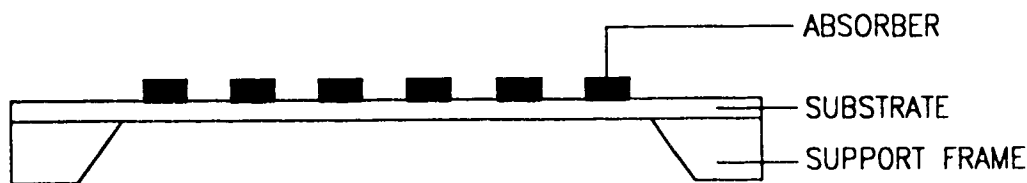


Figure 3.4. X-ray lithography mask.⁽³³⁾

An x-ray mask capable of replicating IC patterns in a production environment must meet certain requirements⁽⁴³⁾. These include high x-ray transmission, high optical transmission for alignment, mechanical stability against distortion to ± 20 nm over 6 months, resistance to radiation damage, low coefficient of thermal expansion and high thermal conductivity to avoid heating when e-beam writing. Among the possible materials, which may satisfy the requirements for an ideal x-ray mask, silicon carbide (SiC) and silicon nitride (Si_3N_4) are commonly used as substrate materials whereas tungsten (W) and gold (Au) are the most promising absorber for x-rays^(44, 45).

One particular process for the fabrication of a mask from reference (46) starts with a silicon wafer which is nitrided with a silicon nitride deposition layer. The silicon wafer is etched back by KOH and epoxy mounted to a Pyrex or glass ring. After depositing a thin film of chromium and a thin film of gold, an x-ray resist is coated. The chromium serves as an adhesion layer and the gold as a plating base for the gold pattern. The pattern is defined in the resist by x-ray or e-beam lithography. Gold about $0.5 \mu\text{m}$ thick is then deposited in the exposed areas by electroplating techniques. The resist is then stripped, followed by removal of the gold plating base. The resulting gold x-ray mask absorber patterns have steep line edge wall profiles. The sequence of steps is shown in Figure 3.5.

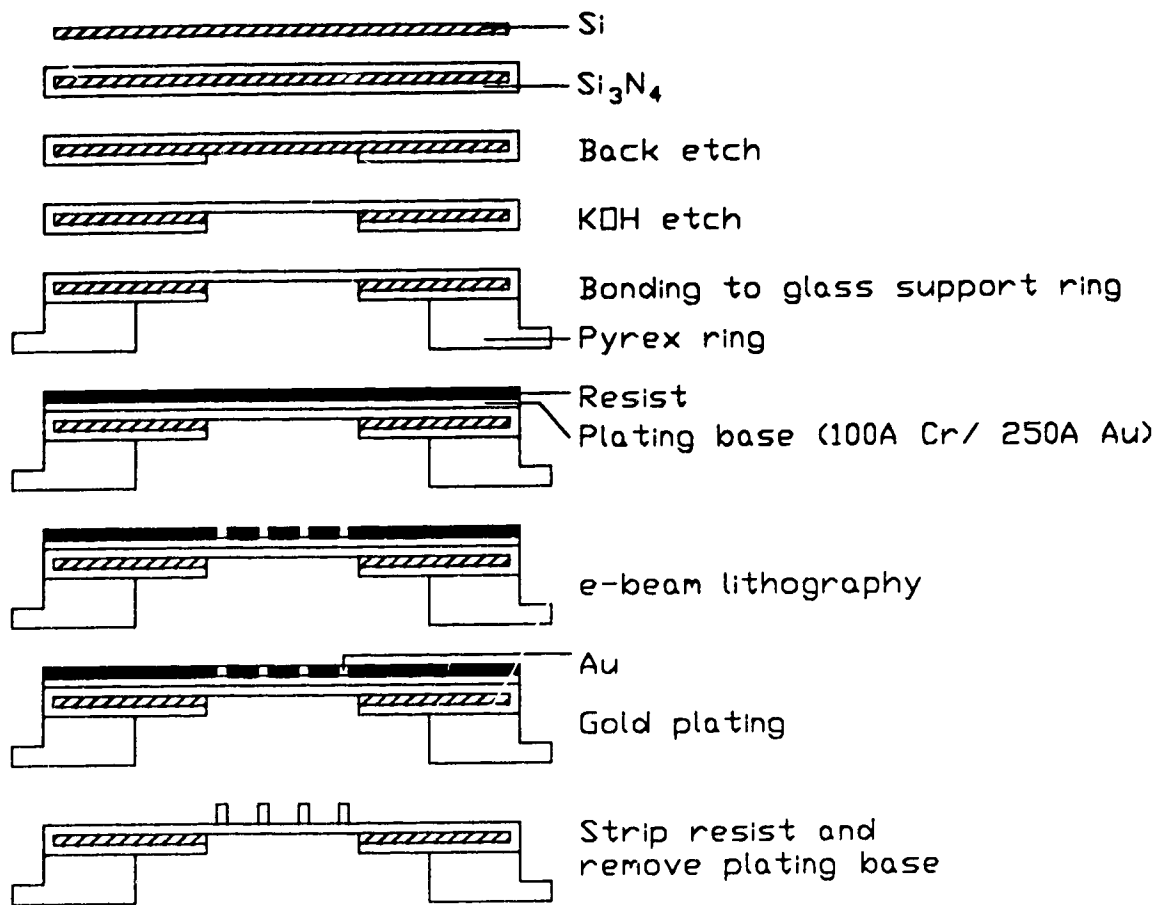


Figure 3.5. Sequence of steps used in the fabrication of Si_3N_4 membrane masks.⁽⁴⁶⁾

3.4 Exposure Tools⁽³³⁾

Presently, most of the commercially available XRL systems include a step and repeat tool (stepper). Horizontal steppers for non-storage ring sources have been fabricated by Perkin Elmer, NTT, and Hampshire Instruments. The storage ring steppers operating at an angle close to vertical have been fabricated by IBM, Karl Suss in Germany, and NTT in Japan. The resolution of these stepper systems is currently limited to approximately $0.35 \mu\text{m}$.

4. Resists

4.1 Resist Hierarchy

Resist materials can be classified as positive and negative on the basis of their radiation response as described in Section 2.2 and illustrated in Figure 2.1. Both resist type can be subdivided into three categories (one-component, two-component and three component systems) depending upon the basic nature of their design⁽⁴⁷⁾.

One-component systems are polymers that combine radiochemical reactivity with etch resistance and film-forming characteristics. In two-component systems, the resist is formulated from an inert matrix resin (which serves as a binder and film-forming material) and a sensitizer molecule which, in general, is monomeric in nature and undergoes the radiochemical transformations that are responsible for imaging⁽⁴⁸⁾. Three component system combines the host polymer which in many cases is Novolak resin, a crosslinking molecule and a dormant catalyst molecule called a photoacid generator (PAG).

X-ray resists can be roughly divided into five classes. Three of these are primarily positive-tone resists and the remaining are negative-tone resists as shown in Figure 4.1.

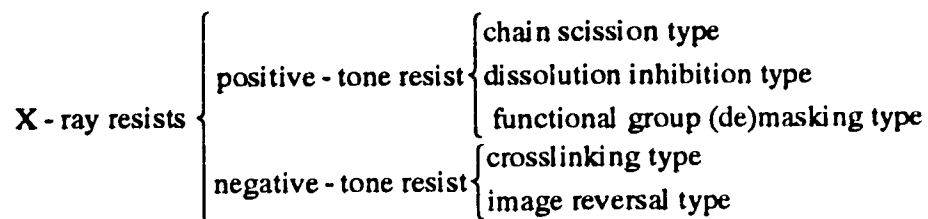


Figure 4.1. Types of x-ray resist.

A comprehensive review of the above resist families can be found in the paper by Lingnau⁽⁴⁹⁾.

The exposure of polymer films in electron beam and in x-ray lithography is a very similar process. The energy of the incident particles in both cases is much larger than the energy required to form or to break a chemical bond. Once an x-ray photon is absorbed, it produces a shower of secondary electrons which carry most of the energy of the incident photon and which interact strongly with the resist material. These secondary electrons are responsible for practically all the chemical changes in the resist. X-ray exposure of a resist is in essence an exposure by electrons, the only difference between an x-ray and an

electron beam exposure system is that in an electron beam system the incident electrons have an energy in the range between 10 and 50 keV. These primary electrons produce a shower of lower energy secondary electrons which interact with the resist in the same manner as for the x-ray exposure. Therefore all electron beam resists are also usable as x-ray resists and nearly all the work on electron beam resists is also useful for x-ray resists and vice-versa⁽⁵⁰⁾.

4.2 Resist Requirements^(51, 52)

There are many general requirements for resist and seven of them are more important requirements.

4.2.1 Solubility

Solubility in organic solvents is a necessary requirement. If wet etching is contemplated, solubility in aqueous media may be undesirable. However, resists for use with plasma etching may use aqueous developers.

4.2.2 Adhesion

The resist must possess adequate adhesion to withstand all processing steps in order to minimize undercutting and maintain edge acuity and feature size control. In some cases, adhesion between the resist and substrate may be enhanced with adhesion promoters such as hexamethyldisilazane (HMDS).

4.2.3 Etch resistance

Etch resistance refers to the ability of the resist to withstand the etching environment during the pattern transfer process. Etchant solutions may be either acidic or basic, depending on the type of substrate to be etched. However, lateral penetration of the chemical etchant is significant for thick substrate films and results in unacceptable line width control for feature sizes < 2 μ m. The need to pattern fine features in thick substrate has led to the development of anisotropic etching methods such as reactive-ion etching, plasma etching, ion milling and sputter etching in which energetic particles bombard the surface, breaking the bonds and removing material.

4.2.4 Sensitivity^(53, 54)

The resist sensitivity for the negative system is defined by that dose where 50 - 90 % (the exact number should be explicitly specified) of the original resist thickness is

maintained. Of course, the unexposed areas of resist are completely developed away and only the exposed images remain. For the positive system, sensitivity is defined as the dose where the image is cleared to the substrate (i.e. the energy dose at the flux intercept) as shown in Figure 4.2. Sensitivity increases as the dose required to produce the lithographic image decreases.

The sensitivity of a resist should be commensurate with machine design parameters to allow optimized throughput.

4.2.5 Contrast

The pattern resolution attainable with a given resist for a particular set of processing conditions is determined in large part by the resist contrast γ . High contrast is important since it minimize the deleterious effect due to diffraction and scattering of radiation in the resist film. Consider a plot of normalized film thickness remaining as a function of $\log_{10}(\text{dose})$ as shown in Figures 4.2.

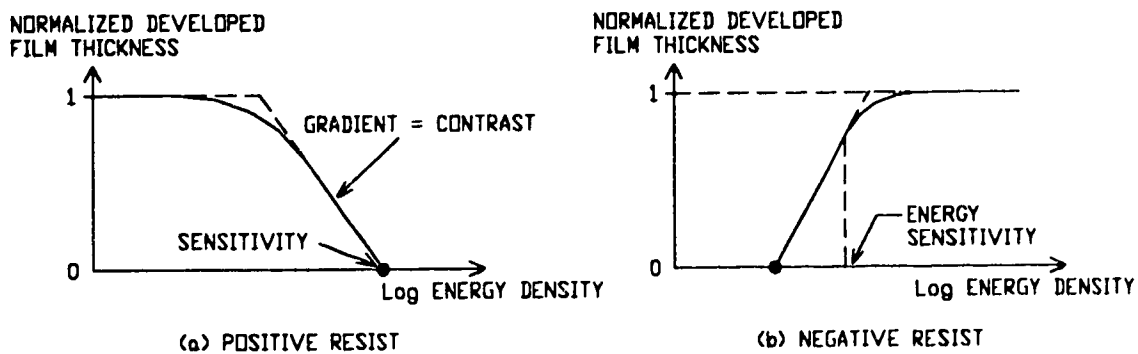


Figure 4.2. Typical lithographic response or contrast plots for resists in terms of the developed thickness normalized to initial resist thickness (p) as a function of $\log_{10}(\text{dose})$.

The numerical value of γ is obtained from the slope of the linear portion of the response curves shown in Figures 4.2 (a) and (b).

4.2.6 Resolution

The resolution capabilities are determined by resist properties such as swelling (deformation during development), sensitivity and contrast. The effect of radiation scattering, which results in the deposition of energy in regions outside the intended

patterned area, can be minimized by using high contrast resist. Also, the resolution is degraded if the resist is too sensitive.

4.2.7 Linewidth Control

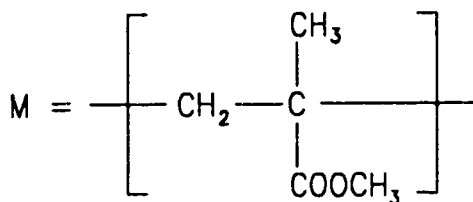
This parameter refers to the necessity of maintaining the correct feature size across an entire substrate and from one substrate to another. The allowable size variation on structures is generally a fixed fraction of the nominal feature size, typically on the order of 10 %.

4.3 PMMA - Positive chain scission resist^(55, 56)

PMMA [poly(methylmethacrylate)], one of the earliest resists, was first used for high resolution e-beam lithography in 1969 and later for x-ray lithography. PMMA is a long linear polymer:



where M represents a methylmethacrylate unit cell with a molecular weight of 100 AMU:

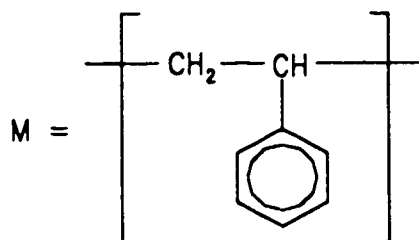


Typically the polymers start with a molecular weight of around 100,000, that is a chain of ~1000 cells. During exposure about 1 % of the linear bonds are broken using about 140 eV of deposited energy per broken bond. Thus after exposure the average molecule consists of about 100 cells. This process is called chain scission. The dissolution rate of PMMA in a developer such as a mixture of MIBK/IPA (methyl isobutyl ketone/isopropyl alcohol) varies approximately inversely as the square of the molecular weight. Thus, the exposed polymer dissolves approximately 100 times faster than the unexposed resist.

The sensitivity of this resist is ~1 J cm⁻² using keV x-rays. This is quite a high dose of x-rays and thus PMMA is considered to be an insensitive resist. At the same time, PMMA has poor resistance to plasma etching. The one outstanding feature of PMMA is its very high resolution. Patterns have been produced down to 30 nm in width using PMMA resist both with x-rays and electrons.

4.4 Negative crosslinking resists

This family of negative resists uses crosslinking in order to form an image. The resist contains linear polymers, such as PCMS [poly(chloromethylstyrene)], which are soluble in an organic developer. The structure of the unit cell of PCMS is as follows:



During exposure crosslinks are formed between adjacent polymers as shown in Figure 4.3.

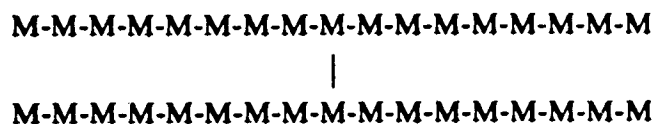


Figure 4.3. Crosslinkage between polymers.

Once there is an average of one crosslink per polymer chain the dissolution rate of the resist decreases dramatically and thus the resist remains where exposed as required for a negative resist. The sensitivity depends on the molecular weight of the polymer chains since the number of crosslinks required decreases. The estimated keV x-ray sensitivities range from ~ 40 to 400 mJ cm^{-2} for molecular weights ranging from 26,000 to 381,000 based on e-beam sensitivity measurements⁽⁵⁷⁾. This family of resists has good resistance to plasma etching which is related to the fact that the molecule contains benzene rings.

However, these resists suffer from one major drawback which is the severe swelling which occurs upon development. The organic solvent molecules get trapped in the spaces between the crosslinked polymers which act as a loosely coupled stringy matrix. The swelling increases for the higher sensitivity, longer polymer chains since the matrix is even more loosely coupled. Thus, it has been found from e-beam exposure measurements that the obtainable resolution ranges from ~ 0.7 to $\sim 2 \mu\text{m}$ for molecular weights of 26,000 to 380,000 and a resolution of better than $0.5 \mu\text{m}$ can not be obtained.

4.5 The Chemistry of two component Positive Photoresists⁽⁵⁸⁾

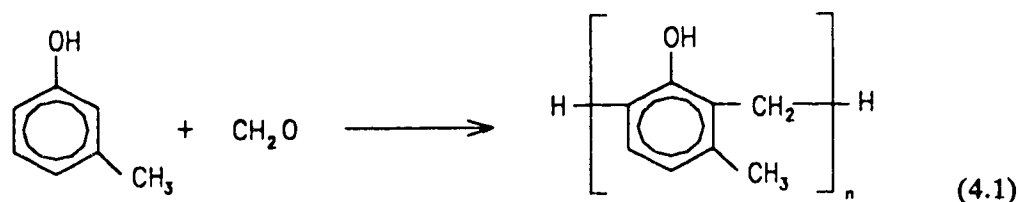
The standard diazo-type positive photoresist is composed of a solvent and two parts: a resin and a photoactive compound (PAC).

4.5.1 Solvent

The solvent renders the resin and PAC into a liquid form which can be easily applied to a planar surface. The solvent is then removed by heating (called prebaking), leaving the resin and PAC in a thin film, chemically unchanged.

4.5.2 Resin

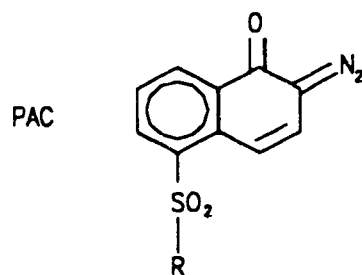
The resin is used as a base polymer which gives the resist its structural properties and its resistance to chemical etching (masking properties). The resin most commonly employed in positive systems is a Novolac-type resin (often called a phenolic resin) which is formed by the polymerization of a phenol (3-Methylphenol) with formaldehyde as indicated in equation 4.1.



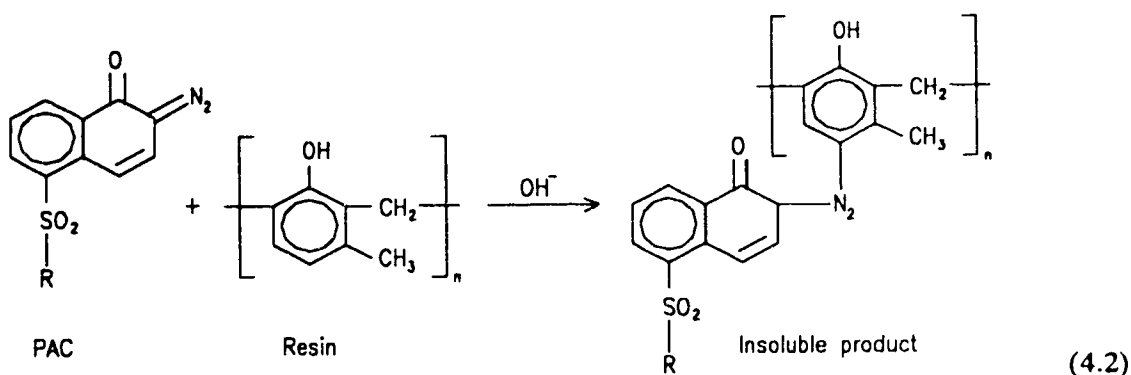
Typically, the chain length, n , is on the order of $3 < n < 10$. By itself, the resin is moderately soluble in developer and is not light sensitive.

4.5.3 PAC

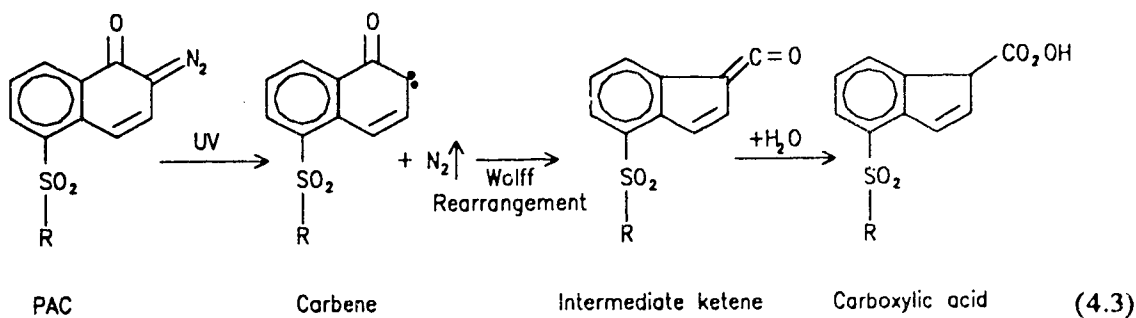
The PAC is added to inhibit the dissolution of the unexposed resist and to enhance the dissolution of the resist which has been exposed to UV radiation. Thus, the PAC is often called an inhibitor as well as a sensitizer. The most common PAC's are from the naphthoquinone family. An example of PAC shown here is a substituted naphthalene 2,2-diazooxide.



In order to inhibit resin dissolution for unexposed resist, the PAC reacts with the resin to form a relatively insoluble compound when in the presence of a basic developer. The reaction of equation 4.2 is one possible mechanism.



In order to enhance resin dissolution for the exposed resist, the PAC undergoes a chemical reaction when exposed to ultra-violet (UV) radiation in the 300 - 500 nm wavelength range. The final product is a carboxylic acid which is very soluble in the basic developer solution as indicated in equation 4.3. The resin is then soluble in the developer.



4.6 Chemically amplified three component resists

In the mid 1980's a new family of resists was developed which uses chemical amplification to enhance their sensitivity⁽⁵⁹⁾. These are based on combining three chemical components and are called three component or chemically amplified resists. The main component is the host polymer which in many cases is Novolak resin. The chemical formula for Novolak is indicated in equation 4.1. This base material does not swell upon development, primarily since a non-organic aqueous alkali developer is used. Also it is very resistant to plasma etching and has proven industrial robustness from optical lithography applications. The second component is a crosslinking molecule such as melamine. The third component is a dormant catalyst molecule called a photoacid generator (PAG).

Upon exposure of the resist the catalyst molecule is activated, i.e. generates an acid molecule as shown in Figure 4.4. Shortly after exposure, the resist is baked at an elevated temperature for a short period of time, typically at 100 - 110 °C for 1 - 2 minutes. This post exposure bake allows the catalyst molecule to diffuse through the resist and a catalytic reaction causes the crosslinker component to attach to the polymer molecules. One catalyst molecule can cause a number of such links giving an amplification of the deposited energy in the resist. These crosslinks greatly reduces the solubility of the exposed resist to the developer solution.

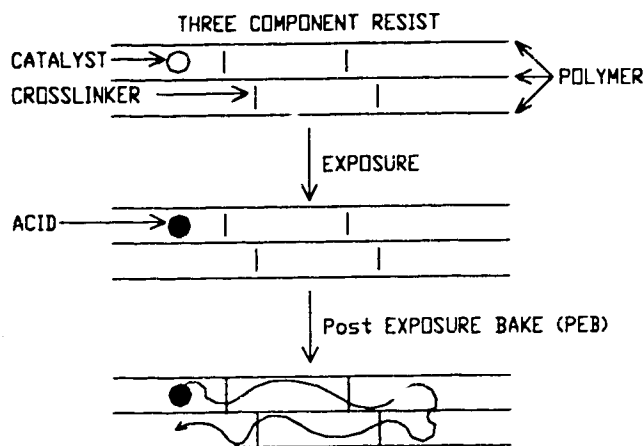


Figure 4.4. Response of chemically amplified three component resist.

The x-ray sensitivity of such resists is very high, in the range of 1 - 50 mJ cm⁻². Typically linewidths down to 0.1 µm can be obtained with such resists as has been demonstrated using x-ray lithography in this project in section 7.9.

Chapter 5:Simulation of X-ray Lithography Process -XD3 Modelling Code

5.1 Introduction

For a complex process such as x-ray lithography involving so many variables the only predictive capability comes from having a simulation code which includes the physics of all the important processes occurring. A number of complete modelling codes exist that predict the final resist profile given a set of exposure parameters such as XMAS⁽⁶⁰⁾, XLIMAS⁽⁴⁰⁾. A modelling code has been developed at the University of Alberta for simulating the exposure and development of the x-ray resist. The modelling code is called XD3 (for X-ray Diffraction, Deposition and Development) which incorporates source spectrum, source spot size, Fresnel diffraction, mask leakage radiation, volumetric deposition in the resist, the development of the resist and prediction of the resulting resist profile. The aim of this model is to calculate the allowable range of exposures and mask to wafer gaps which will still ensure that the final linewidth falls within an allowed tolerance of the desired value.

5.2 Structure of the XD3 modelling code

The XD3 modelling code is written in FORTRAN language and consists of three sub-programs: xdepos, xprof, and xetch. Each sub-program has its own parameter file and output file and passes the results to the next program.

The first sub-program “xdepos” takes the source spectrum from a laser produced plasma and convolves with the transmission functions of the filters and mask layers to calculate the x-ray energy deposition as a function of the depth in an x-ray resist and substrate both for the main irradiation spectrum and leakage spectrum.

The second sub-program “xprof” calculates the one dimensional Fresnel diffraction of the x-rays from the mask pattern onto the resist surface. In this calculation the frequency spectrum is divided into ten spectral bins with one-tenth of the total power in each bin and the intensity diffraction pattern for each individual frequency bin calculated. These intensity distributions are then summed up to give the total diffraction of the input spectrum. In addition, for point sources, the broadening due to source geometry is also calculated using the given distances from source to mask and from mask to wafer together with the diameter of the source.

Finally, the third sub-program “xetch” calculates the development of the resist pattern as time progresses until the development front hits the surface of the wafer or the evolved side walls overlap one another. The models⁽⁶¹⁾ used will be described in the next section.

5.3 Development Model of chemically amplified negative resists

For chemically amplified negative resists a dissolution model proposed by Ziger⁽⁶¹⁾ is employed. In that model, the fraction of resist remaining after development as a function of incident dose is related to the development rate which in turn is assumed to be dependent on the concentration of a soluble species which is photochemically consumed for negative resists. The remaining resist thickness after development is given by (normalized to the initial thickness):

$$\tau_N = 1 - \Delta\tau_{PEB} - \Delta\tau_{DEV} \quad (5.1)$$

where $\Delta\tau_{PEB}$ = thickness loss due to post-exposure bake

$\Delta\tau_{DEV}$ = thickness loss due to development

We model the resist as a mixture of a base soluble species, [S], and an insoluble species, where the initial is all soluble species with a concentration of $[S_0]$.

For post-exposure bake the shrinkage is given by:

$$\Delta\tau_{PEB} = \Delta\tau_{(E=0)} + \left(1 - \frac{[S]}{[S_0]}\right)G \quad (5.2)$$

where $\Delta\tau_{(E=0)}$ = thickness loss due to PEB at zero exposure

G = fractional volume change for complete conversion

For development:

$$\Delta\tau_{DEV} = \frac{\int_0^{t_{DEV}} r_{DEV} dt}{D} \quad (5.3)$$

where r_{DEV} = development rate at time t

D = initial resist thickness

t_{DEV} = development time

If r_{DEV} is a constant,

$$\begin{aligned} \Delta\tau_{DEV} &= \frac{r_{DEV} \times t_{DEV}}{D} \\ &= \frac{k_{DEV} t_{DEV} [S]^p}{D} \end{aligned} \quad (5.4)$$

where we assume that the development rate is proportional to the nth power of the concentration of soluble species, $r_{DEV} = k_{DEV} [S]^n$

Substituting equation (5.4) into equation (5.1) gives:

$$\tau_N = 1 - \Delta\tau_{PEB} - \frac{k_{DEV} t_{DEV} [S]^n}{D} \quad (5.5)$$

Now we have to find the concentration of the base soluble species, [S], which is the unreacted base soluble polymer prior to development. Photolysis generates H^+ that catalyzes a base insolubilization reaction. The photoacid generator decomposes upon radiation to form an acidic product which for simplicity will be denoted by a proton:



From first-order decomposition photochemistry the rate of change in the concentration of the photoacid generator as a function of absorbed radiation, E, is:

$$\begin{aligned} \frac{d[PAG]}{dE} &= -k_{photo}[PAG] \\ \Rightarrow [PAG] &= [PAG_o] e^{-k_{photo}E} \end{aligned} \quad (5.7)$$

where [PAG] = final PAG concentration
 [PAG_o] = initial PAG concentration
 k_{photo} = reaction coefficient

Acid catalysis is sensitive to residual contaminants. For a given amine concentration in the photoresist, a certain amount of acid will be consumed in the neutralization reaction.

$$\begin{aligned} [H^+] &= [PAG_o] - [PAG] - [amine] \\ &= [PAG_o] - [PAG_o] e^{-k_{photo}E} - [PAG_o] (1 - e^{-k_{photo}E_{inhib}}) \quad (\text{by (5.7)}) \end{aligned}$$

where E_{inhib} = inhibition dose to generate enough acid to neutralize the amine

$$[H^+] = [PAG_o] \left(e^{-k_{photo}E_{inhib}} \right) \left[1 - e^{-k_{photo}(E - E_{inhib})} \right] \quad (5.8)$$

For the post exposure bake (PEB) process let t_{PEB} be the post-exposure bake time, k_{PEB} be the rate constant and $[H^+]$ be the photoacid concentration (assumed to be a constant). The time rate of decrease in soluble species concentration due to the catalysis is given by:

$$\begin{aligned}
 \frac{d[S]}{dt} &= -k_{PEB}[S][H^+] \\
 \Rightarrow [S] &= [S_0] e^{-k_{PEB}[H^+]t_{PEB}} \\
 &= [S_0] e^{-[PAG_0](e^{-k_{photo}E_{inhib}}k_{PEB}t_{PEB}) \left[1 - e^{-k_{photo}(E - E_{inhib})}\right]} \quad (\text{by (5.8)}) \\
 &= [S_0] e^{-\alpha e^{-k_{photo}E_{inhib}} \left[1 - e^{-k_{photo}(E - E_{inhib})}\right]} \quad (5.9)
 \end{aligned}$$

where $\alpha = [PAG_0]k_{PEB}t_{PEB}$

Substituting (5.9) into (5.5) gives:

$$\tau_N = 1 - \Delta\tau_{PEB} - \frac{k_{DEV}t_{DEV}[S_0]^n}{D} \left\{ e^{-\alpha n e^{-k_{photo}E_{inhib}} \left[1 - e^{-k_{photo}(E - E_{inhib})}\right]} \right\} \quad (5.10)$$

Define E_{clear} to be the energy dose per unit volume such that the resist will just be removed in the processing, i.e. $\tau_N = 0$ at $E = E_{clear}$.

$$\begin{aligned}
 0 &= 1 - \Delta\tau_{PEB, E_{clear}} - \frac{k_{DEV}t_{DEV}[S_0]^n}{D} \left\{ e^{-\alpha n e^{-k_{photo}E_{inhib}} \left[1 - e^{-k_{photo}(E_{clear} - E_{inhib})}\right]} \right\} \\
 \Rightarrow \frac{k_{DEV}t_{DEV}[S_0]^n}{D} &= (1 - \Delta\tau_{PEB, E_{clear}}) \left\{ e^{\alpha n e^{-k_{photo}E_{inhib}} \left[1 - e^{-k_{photo}(E_{clear} - E_{inhib})}\right]} \right\} \quad (5.11)
 \end{aligned}$$

Substitute (5.11) into (5.10):

$$\tau_N = 1 - \Delta\tau_{PEB} - (1 - \Delta\tau_{PEB, E_{clear}}) e^{-\alpha n (e^{-k_{photo}E_{clear}} - e^{-k_{photo}E})} \quad (5.12)$$

The dissolution rate can be rewritten using equation (5.9):

Then substituting from equation (5.11):

$$r = \frac{D}{t_{DEV}} (1 - \Delta\tau_{PEB, E_{clear}}) \left\{ e^{\alpha n e^{-k_{photo} E_{inhib}}} [1 - e^{-k_{photo} (E_{clear} - E_{inhib})}] \right\} e^{-\alpha n e^{-k_{photo} E_{inhib}}} [1 - e^{-k_{photo} (E - E_{inhib})}]$$

$$= r_{clear} e^{-\alpha n (e^{-k_{photo} E_{clear}} - e^{-k_{photo} E})}$$

$$r = r_{clear} \exp \left\{ -n \left[\exp \left(-\frac{E_{clear}}{E_{th}} \right) - \exp \left(-\frac{E}{E_{th}} \right) \right] \right\} \quad (5.13)$$

where r_{clear} is the development rate at E_{clear} which is given by $r_{clear} = \frac{D}{t_{DEV}} (1 - \Delta\tau_{PEB, E_{clear}})$

and a threshold energy dose is defined to be $E_{th} = \frac{1}{k_{photo}}$

The above model does not take into account a finite dissolution rate of the fully exposed resist which can be added as an extra constant giving

$$r = r_{clear} \exp \left\{ -n \left[\exp \left(-\frac{E_{clear}}{E_{th}} \right) - \exp \left(-\frac{E}{E_{th}} \right) \right] \right\} + r_{min} \quad (5.14)$$

There are five constants (r_{clear} , E_{clear} , E_{th} , n and r_{min}) which must be determined experimentally to fit this model.

5.4 Output files of XD3 modelling code

Each subprogram xdepos, xprof and xetch will output a series of graphs and output files after running the program. A brief explanation of each subprogram and a description of the output files and graphs from each subprogram is given below.

5.4.1 Output graphs and files of x-ray deposition program (xdepos)

Xdepos uses the given x-ray source spectrum and calculates the fractional energy deposition per unit length of propagation through the mask, resist and substrate. The calculation is based on the standard x-ray absorption cross-sections for the various elements as a function of x-ray photon energy. The x-ray source spectrum and filter, mask, resist and wafer layers are specified in the input file xdepos.par. There are three spectral

plots, two deposition plots and two output files produced by the program xdepos. These give the spectrum of x-rays at the resist surface behind the clear areas of the mask (xmnspec.out), behind the opaque areas of the mask (xlkspc.out) and at some user specified probe point in the system (xprbsp.out). The main output consists of two deposition profiles in the resist/substrate due to the main spectrum and leakage spectrum. The output is illustrated below for the case of copper irradiating a 0.5 μm thick gold mask on front of a 1.5 μm thick Shipley negative resist layer coated on a 1 μm silicon wafer. The mask is covered with four layers of B10 filters (a polycarbonate filter covered with a thin layer of aluminum as described in Chapter 6) and is situated at 4 cm from the copper target. The whole assembly is in 640 torr of helium gas.

The main irradiation spectrum hitting the mask is shown in Figure 5.1. The leakage spectrum through the opaque mask metal is shown in Figure 5.2. The probe spectrum for x-rays which have propagated through the mask substrate, resist and wafer as observed at the bottom of the silicon wafer layer is shown in Figure 5.3.

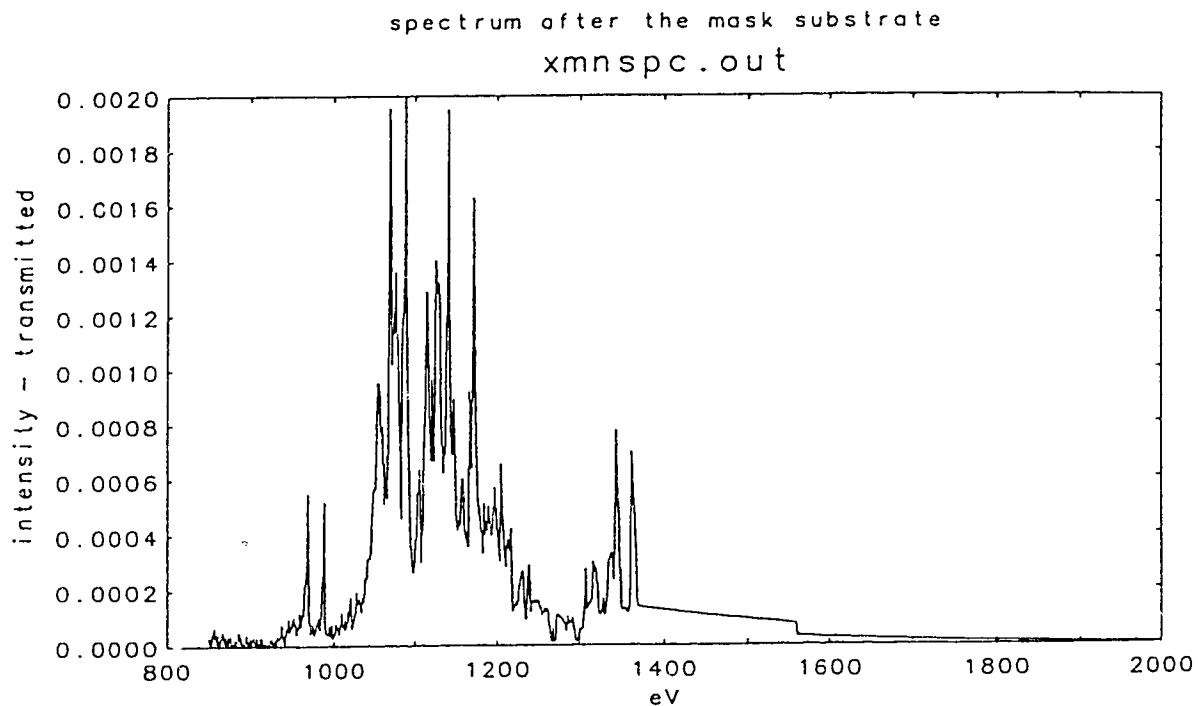


Figure 5.1. Output graph of XD3 - xmnspec.out.

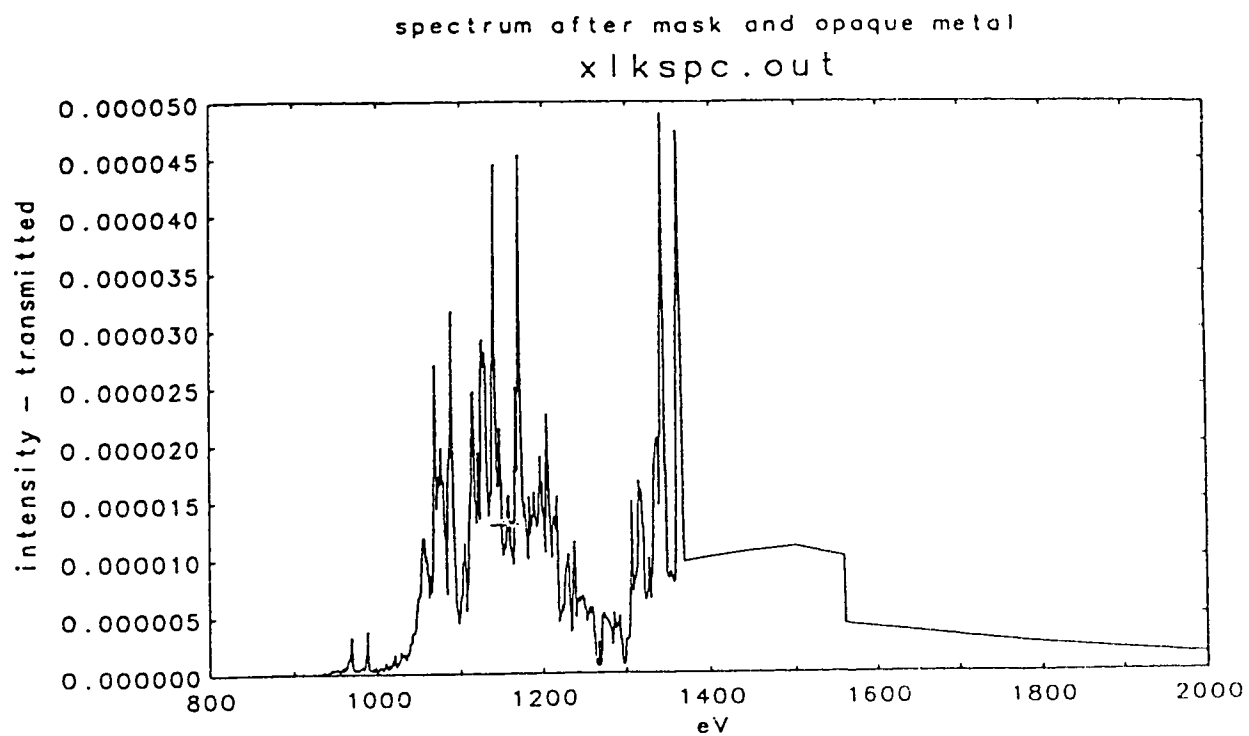


Figure 5.2. Output graph of XD3 - xlkspc.out.

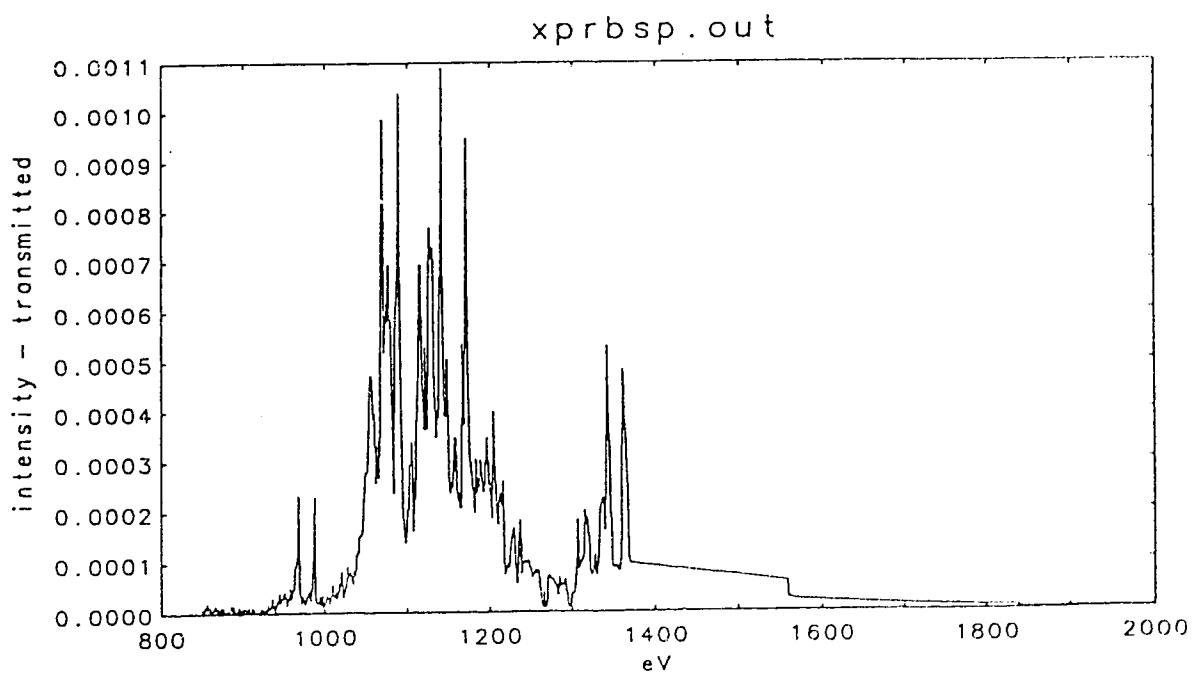


Figure 5.3. Output graph of XD3 - xprbsp.out.

The deposition profiles in the resist and substrate from the main spectrum (Xmnspc.out) and leakage spectrum (Xlkspc.out) are plotted on the same graph as shown in Figure 5.4. The first row of ESPCIN, ESPRES, ESPOUT, EDEPOS refers to the energy in the main spectrum through the transparent mask substrate whereas the second row refers to the leakage spectrum through the opaque mask metal. The definitions of these variables are:

ESPCIN : Input energy spectrum normalized to unity (i.e. unit area)

ESPRES : Energy spectrum at the surface of the resist

ESPOUT : Output energy spectrum at the back side of the system

EDEPOS : Energy deposition in resist and wafer (= ESPRES - ESPOUT), which is the area under the solid curve (for main spectrum) or dotted curve (for leakage spectrum).

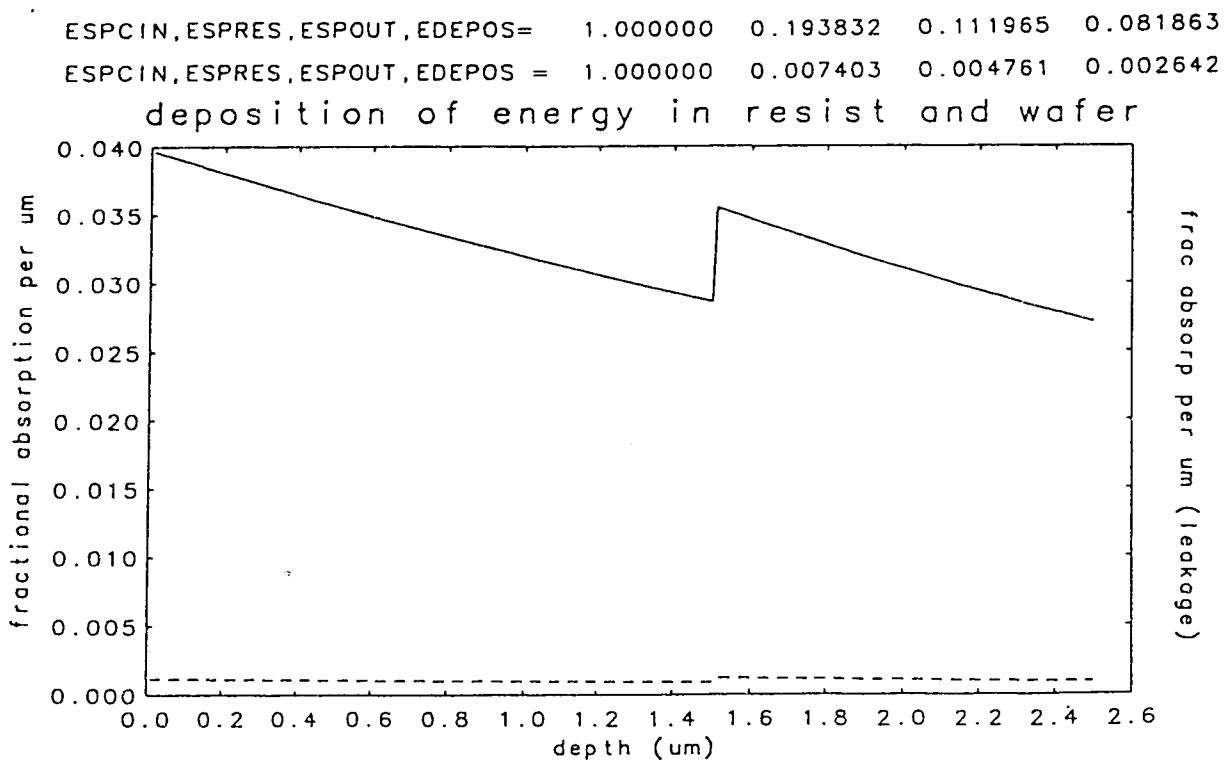


Figure 5.4. Output graph of XD3 - xmndep.out and xlkdep.out.

5.4.2 Output graphs and files of x-ray diffraction program (xprof)

Xprof uses Huygen's principle to numerically calculate the Fresnel diffraction for a one dimensional slit pattern with multiple openings. The slit pattern, distances, input spectrum name are given in the input file xprof.par. There is one diffraction plot produced by the program xprof and a corresponding output file. This gives the one dimensional Fresnel diffraction from multiple slits convolved with the geometric source spot shadow. The diffraction is calculated for ten frequency bands across the input spectrum and the resultant intensity patterns summed to give the final output. An example of the Fresnel diffraction pattern across the surface of the resist is shown in Figure 5.5. The data from the plot is output to the file xprof.out.

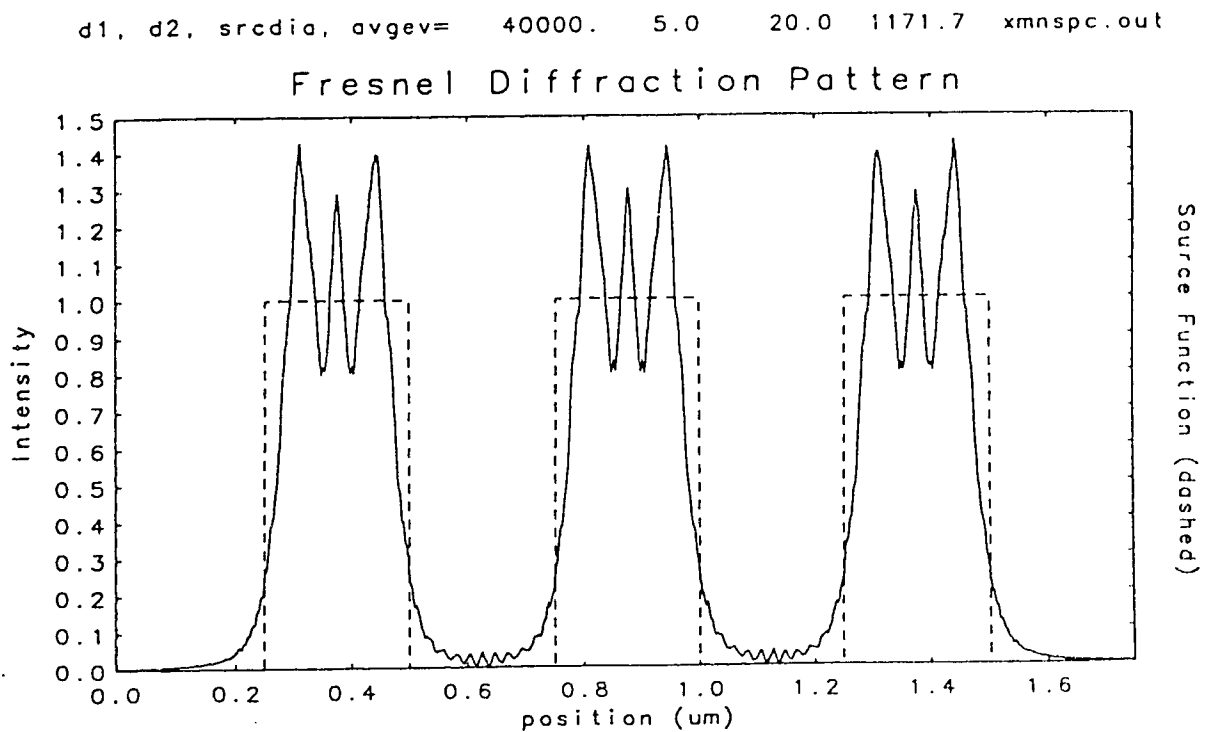


Figure 5.5. Output graph of XD3 - xprof.out.

The pattern shown is for three exposure lines $0.25 \mu\text{m}$ wide with a spacing of $0.5 \mu\text{m}$ center to center with a mask to wafer gap of $5 \mu\text{m}$ using the copper spectrum shown in Figure 5.1. The intensity is normalized to the incident intensity of the x-ray radiation.

5.4.3 Output graphs of x-ray development program (xetch)

Xetch simulates the development of the resist by advancing a development front line through the resist using a dissolution rate at each point in the resist given by the rate equation 5.14 which is dependent on the local energy density of absorbed x-ray radiation. The resist, development model and parameters in equation 5.14 are given in the input file xetch.par. There are one contour and one or more resist profile plots produced by xetch. The contour plot gives the deposited energy density contours throughout the resist and wafer volume prior to the development process which is calculated taking the product of the axial deposition profile and the Fresnel diffraction pattern. The resist profiles give the output of the etched resist cross-section at various user specified times.

The deposited energy density contours in J cm^{-3} throughout the resist and wafer volume are shown in Figure 5.6. The conditions for this calculation are 80 mJ cm^{-2} exposure flux before the filters at the surface of the mask. In Figure 5.6 the x-rays enter from the bottom, the resist layer extends from 0.0 to $1.5 \mu\text{m}$ and the silicon substrate from 1.5 to $2.4 \mu\text{m}$.

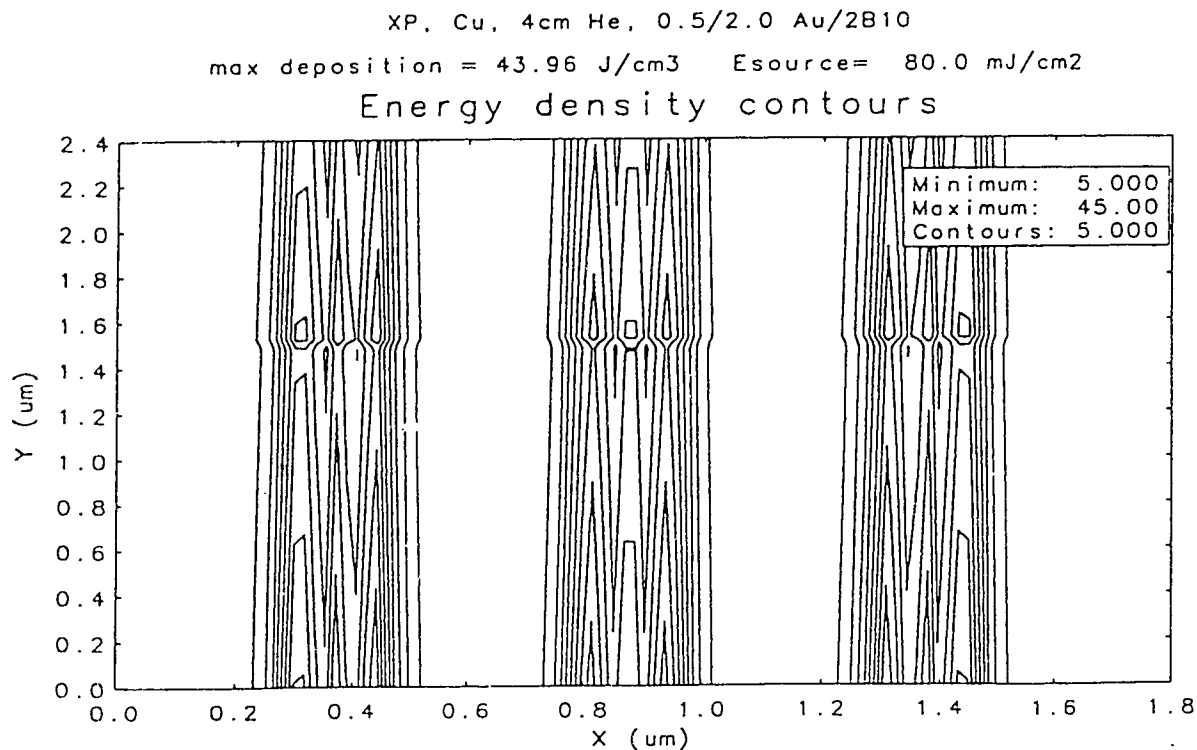
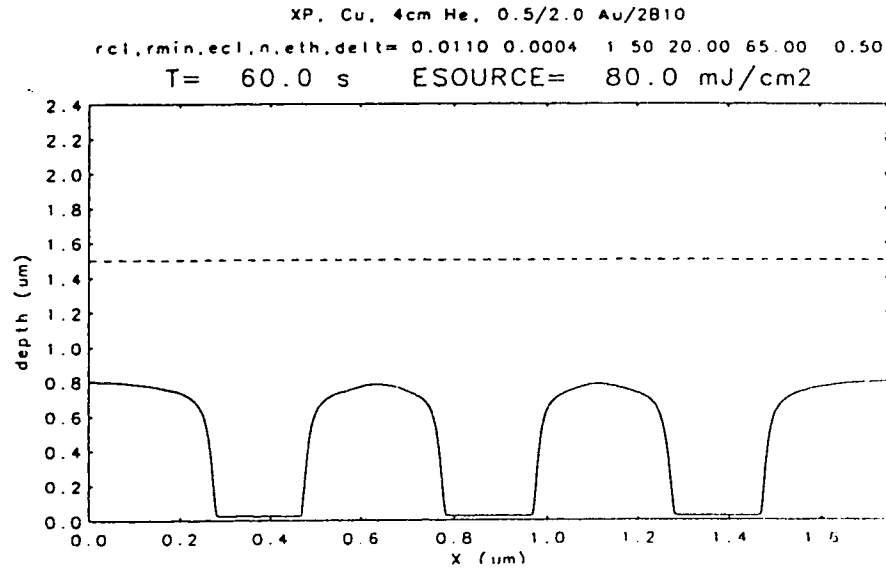
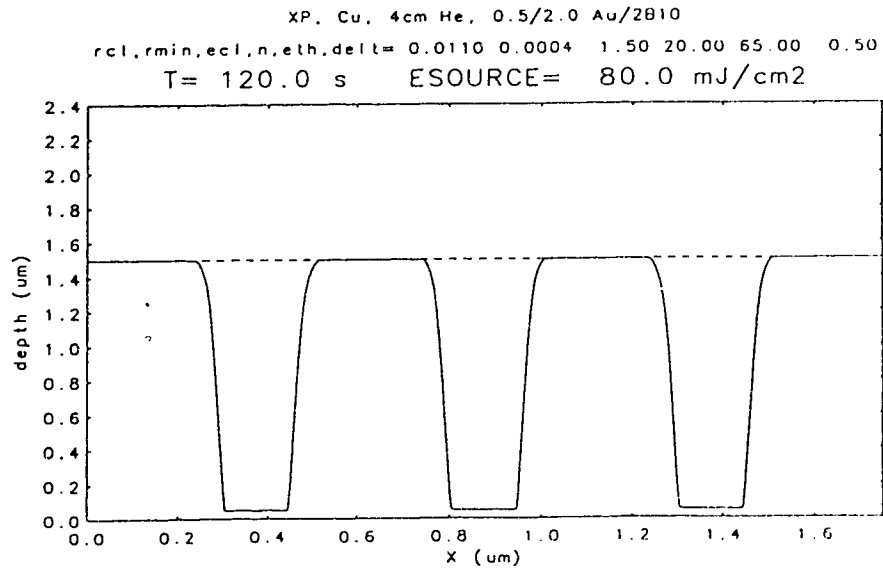


Figure 5.6. Output graph of XD3 - contour plot.

The predicted resist profiles after etching for the specified development times are shown in Figure 5.7. The values used in this case for the parameters in equation 5.20 are $r_{\text{clear}} = 0.011 \mu\text{m s}^{-1}$, $E_{\text{clear}} = 1.5 \text{ J cm}^{-3}$, $E_{\text{th}} = 65 \text{ J cm}^{-2}$, $n = 20$ and $r_{\text{min}} = 0.0004 \mu\text{m s}^{-1}$.



(a)



(b)

Figure 5.7. Output graph of XD3 - resist profile at (a) 60 s and (b) 120 s.

6. X-ray Exposure Station

The x-ray source used in the project is a keV x-ray source based on plasma production using a high repetition rate picosecond KrF laser developed in the Department of Electrical Engineering, University of Alberta⁽⁶²⁾.

6.1 Introduction

It is known that UV laser pulses are more efficient than visible or infrared laser pulses in generating x-rays from laser produced plasmas because of the higher emissivity of the high density plasma produced⁽⁶³⁾. X-rays in the keV photon-energy range are of particular interest for exposing x-ray resists using the proximity mask technique.

6.2 KrF Laser System

The schematic layout of the short pulse KrF laser system is shown in Figure 6.1.

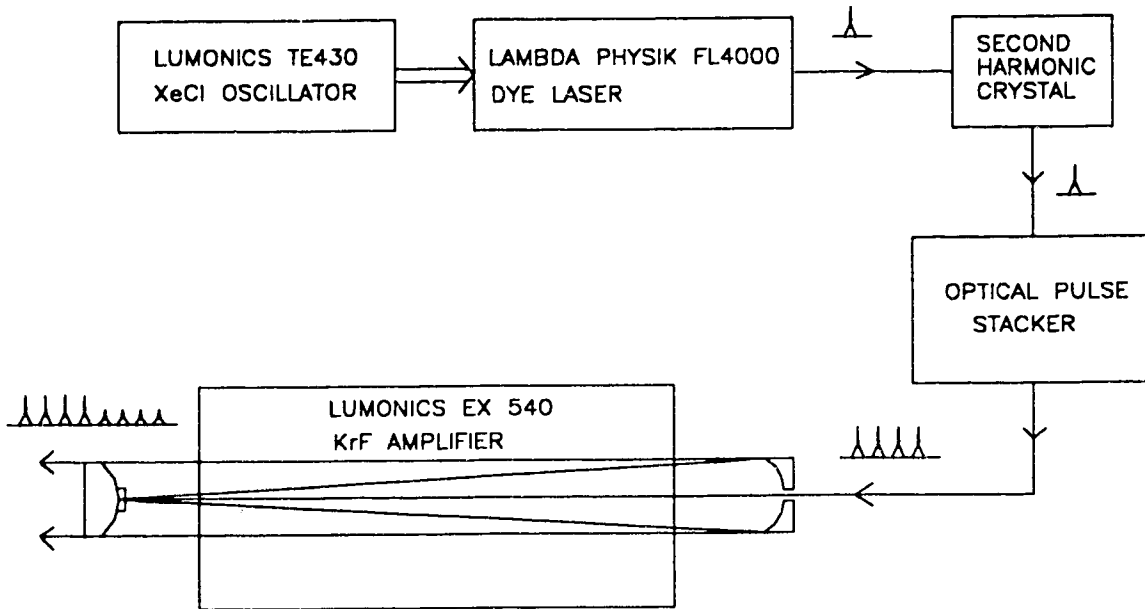


Figure 6.1. Schematic diagram of the picosecond KrF laser system.

A Lumonics TE430 XeCl laser module with a pump energy of approximately 20 mJ per pulse with a duration of 7 ns is used to pump a Lambda Physik FL-4000 dye laser system which is used to produce 50 ps pulses at 497 nm in the visible wavelength region. The 497 nm component of the output pulse is selected using a grating and then proceeds through 3 stages of dye amplification. The final output pulse has an energy of $\sim 150 \mu\text{J}$ and a duration of 50 ps. The output repetition rate is limited by the XeCl laser to a maximum of 20 Hz.

The visible pulse is frequency doubled in an 8 mm long type-I β -Barium-Borate crystal to produce a UV pulse at 248.5 nm with an energy of $\sim 10 \mu\text{J}$. In order to improve the conversion efficiency of laser energy into keV x-rays in the plasma, shorter pulses with higher peak power are required. Excimer lasers have upper state lifetimes of the order of a few ns and so it is not possible to extract the available energy in a single ps pulse. The best that can be done is to extract a train of picosecond pulses. As a result, the UV pulse is divided, delayed and recombined twice with 50 % beam splitters in order to produce a train of four pulses with an interpulse separation of 1.8 ns. Half of the input energy is lost in the pulse stacker system leading to a final energy of $\sim 1 \mu\text{J}$ per pulse.

The pulse train is sent into a Lumonics EX540 KrF discharge laser module where it is amplified in three passes. The amplifier geometry is that of confocal unstable resonator with a magnification of 10 times and a round trip time of 7.6 ns. The pulses are coupled into the amplifier through a 3 mm diameter hole in the concave resonator mirror. A second set of four pulses is obtained due to the diffraction coupling from the edge of the hole which prevents direct feedback in the unstable resonator.

A typical output train of pulses with a total energy of 186 mJ is shown in Figure 6.2. One can observe the initial four pulses and the diffracted set of four pulses for a total gain window of ~ 15 ns. In addition to the short pulses, there is a rising level of amplified spontaneous emission (ASE) throughout the pulse train. The final output energy can be controlled over the range of 100 - 300 mJ by varying the fill pressure and voltage on the KrF amplifier module. Thus, maximum output powers of up to 6 W could be obtained.

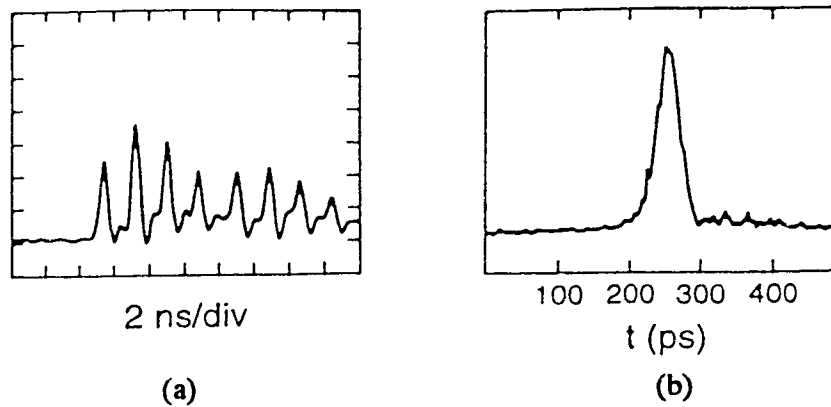


Figure 6.2. (a) Photodiode trace of the output ps pulse train (200 mV, 2 ns /division).
(b) Streak camera trace of a single pulse in the train.

6.3 X-ray Emission Characterization

The setup for the target experiments is shown in Figure 6.3. The laser pulse train is sent into a vacuum target chamber and focused by means of a 125 mm focal length, aberration corrected, triplet lens to an 8 μm diameter spot onto solid and tape targets. The laser is incident at angle of 45° to the target normal. The quantitative x-ray yield is measured using filtered silicon p-i-n diodes⁽⁶⁴⁾ and the fast temporal shape of emission is determined with filtered vacuum x-ray diodes⁽⁶⁵⁾.

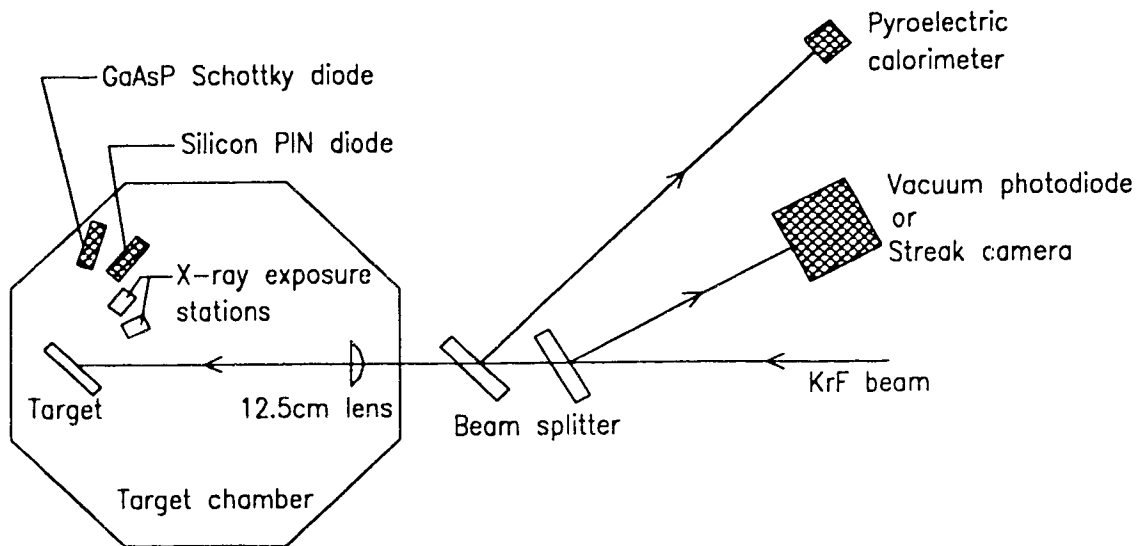


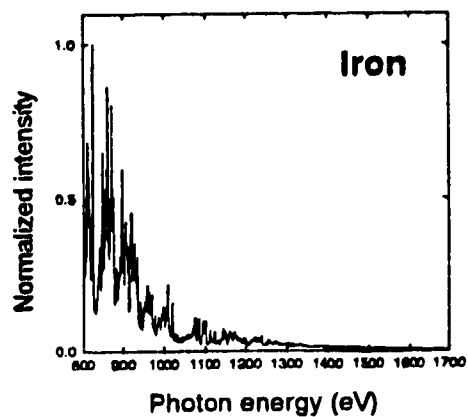
Figure 6.3. Schematic diagram of target chamber and diagnostics.⁽⁶⁶⁾

The emission characteristics of the plasma source have been previously characterized. Spectral measurements were made using a TAP (thallium hydrogen phthalate) crystal spectrograph and Kodak DEF film. The plasma size was measured using a pinhole camera together with DEF film which was covered by two layers of B10 filter material.⁽⁶⁷⁾ B10 filter material consists of a 2 μm polycarbonate substrate coated with 0.165 μm of aluminum. This filter blocks radiation with photon energies below ~ 800 eV and transmits keV radiation. A typical pinhole camera image of the plasma created by the picosecond laser train at normal incidence on a copper target, taken from the side of the plasma is shown in Figure 6.4 (the laser is incident from the right as shown on the sketch). The image as viewed from the side of the target has a size of 17 μm across by 28 μm long. The overall source size of 30 μm is much smaller than required for a keV proximity lithography source and will lead to negligible source size degradation of lithography resolution.

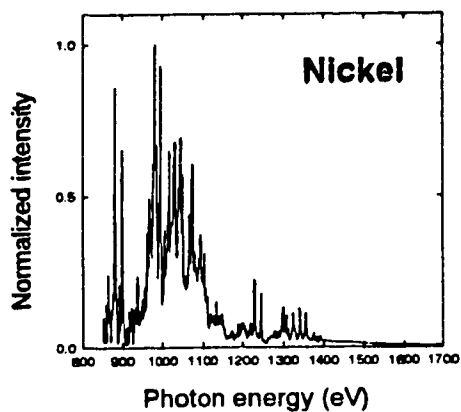


Figure 6.4. X-ray pinhole picture of the plasma produced by the laser at normal incidence from reference 62.

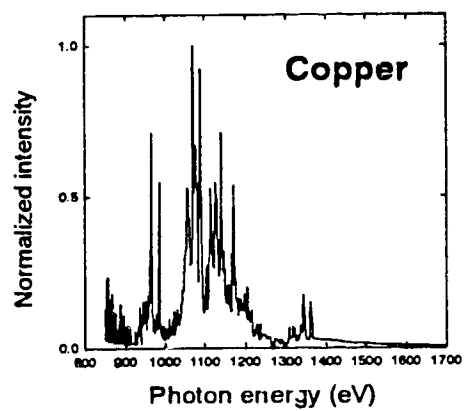
Using different target species the output spectrum can be tuned to different center frequencies. Typical spectra obtained from iron, nickel and copper targets are shown in Figure 6.5 (a) - (c), respectively. The x-ray conversion efficiency (defined as x-ray energy emitted into 2π steradians divided by incident laser energy) into the keV region was on average 2.3 % for iron, 1.9 % for nickel and 1.5 % for copper⁽⁶²⁾ .



(a)



(b)



(c)

Figure 6.5. Spectra of keV x-rays from (a) Iron, (b) nickel and (c) copper.

6.4 X-ray Lithography Exposures at high repetition rate in a Helium flow target chamber

The lithography experiments reported in this thesis were carried out in the vacuum target chamber shown in Figure 6.3. The samples were mounted on a conical ring holder so that they were located at an angle of 60° relative to the target surface normal. In order to remove debris and to prevent target debris from hitting the mask in x-ray lithography systems it is desirable to work in a partial pressure of background gas. Also, in order to simplify the target system it would be desirable to work at atmospheric pressure. These goals can be achieved by working at one atmosphere of helium background pressure which has a transmission of 90 % for 1 keV photons over a 10 cm path length. The short wavelength of our laser source allows operation at one atmosphere helium pressure with only minor perturbation on the x-ray yield from the solid target surface. A plot of the transmission of 10 cm of Helium versus photon energy is shown in Figure 6.6.

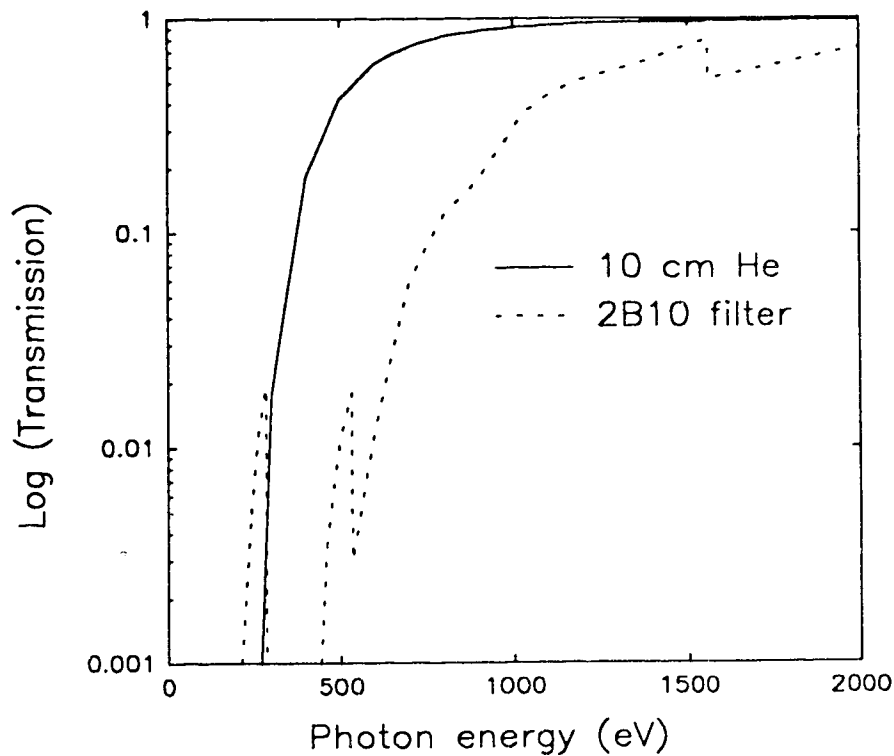


Figure 6.6. Transmission of 10 cm Helium and 2B10 filter versus photon energy.

In addition to the helium gas, a filter consisting of four layers of B10 filter material was used in front of the resist samples to eliminate the soft x-rays. The transmission of two layers of B10 material (2B10) versus photon energy is given in Figure 6.6. The values of transmission of B10, 2B10 and 4B10 filters for copper and iron spectrum is given in Table 6.1.

| | Transmission T_2 | | |
|--------|--------------------|------|-------|
| Target | B10 | 2B10 | 4B10 |
| Copper | 0.67 | 0.46 | 0.21 |
| Iron | 0.56 | 0.31 | 0.096 |

Table 6.1 : Transmission of B10 filters for copper and iron spectra

To calculate the energy flux at the surface of the resist sample, the transmission functions of both helium and 4B10 filters must be taken into consideration.

Let E (mJ) be the total energy produced at the target, L (cm) be the distance from target to the resist sample, T_1 be the transmission of helium and T_2 be the transmission of 4B10 filters. Then the x-ray flux \mathcal{F} (mJ cm⁻²) at the surface of the resist sample is given by equation 6.1.

$$\mathcal{F} = E \times \frac{1}{2\pi L^2} \times T_1 \times T_2 \quad (6.1)$$

The target chamber used for the exposure experiments has a diameter of 80 cm and contained a motorized tape target drive system, motorized lens focusing control, reference x-ray diode monitor stations, an x-ray exposure station array for sample exposure at various distances and a vacuum / gas handling system for evacuating and flushing with partial pressures of helium for debris control.

The firing of the laser can be triggered externally by computer, manually by a hand triggering pulse box or internally at a fixed repetition rate. A block diagram of the firing control and diagnostic system is shown in Figure 6.7. The x-ray flux measured by the monitor diodes is fed to an analog to digital converter (ADC) board in a desktop personal computer (PC). This computer controller system automatically advances the target and fires the laser to achieve the specified x-ray exposure for the given resist sample. The focusing of the lens in the target chamber to produce the maximum x-ray

signal is achieved by using a motorized positioning stage to scan the lens forward and backward in predefined steps of a few microns.

The detailed step-by-step operation of the laser system is outlined in Appendix 1.

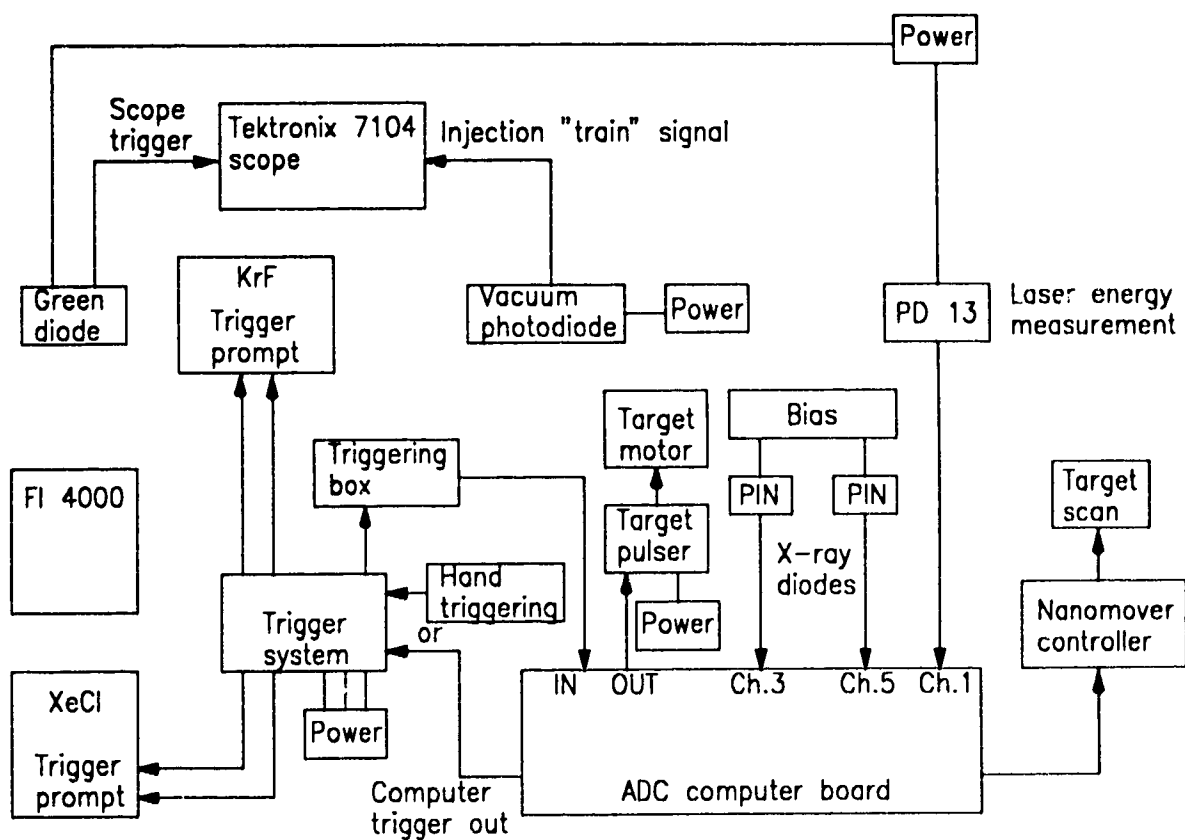


Figure 6.7. Block diagram of the component in x-ray lithography laboratory.

Chapter 7 : Experimental Measurements of a Negative X-ray Resist

7.1 Introduction

The initial studies of the Shipley XP90104C⁽⁶⁸⁾ negative x-ray resist indicated that it was fairly robust and stable leading to reproducible results on repeated runs. In contrast, a high sensitivity positive resist, PBS, which was also tried was very sensitive to the processing environment, humidity in particular, as shown in Figure 7.1. It was harder to study in a reproducible manner and thus after initial tests PBS was not studied in detail. It was, therefore, determined to study and characterize the negative resist in detail.

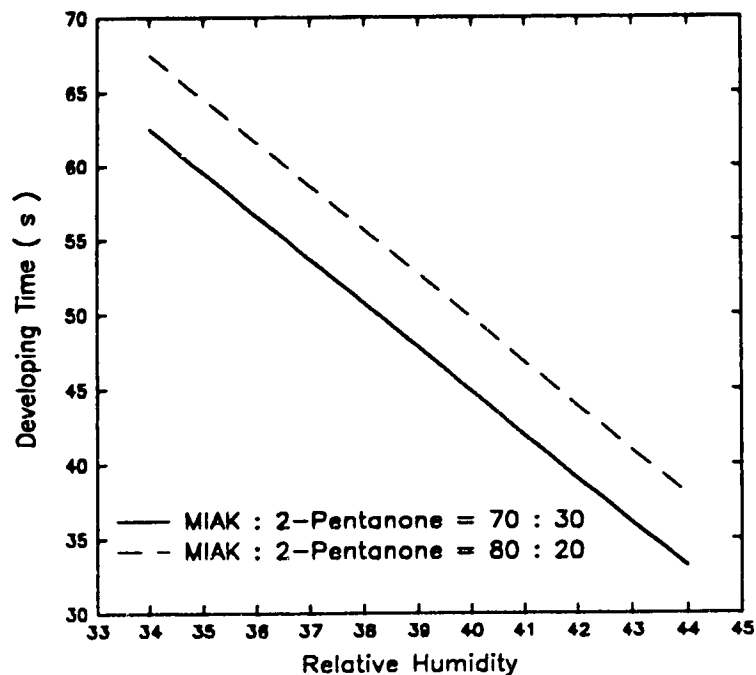


Figure 7.1. Typical PBS developing time versus relative humidity.⁽⁶⁹⁾

Studies were carried out to characterize the XP90104C negative resist in terms of the following properties:

1. etch rate as a function of exposure,
2. resistance to plasma etching,
3. contrast and sensitivity,
4. optimum exposure dosage for given line widths,
5. line profiles as a function of the gap.

7.2 Spincoat of the resist on the wafer

The first step in the lithography tests involved spin coating a thin layer of resist on the wafer. The following spin coating procedure was used. A predetermined amount of the resist solution is poured through a nozzle onto a wafer held on a vacuum chuck. The wafer is accelerated rotationally to a final spin speed of 1500 - 10,000 revolutions per minute (rpm) depending on the thickness of the resist required. Much of the original liquid is spun off the wafer edge. A small fraction remains and dries through solvent evaporation. The resist coated wafer is prebaked at 110 °C for 60 seconds to remove residual solvent, relax stresses induced by the flow, harden the film and increase adhesion of the film to the substrate. The hardened resist forms a thin film over the wafer. The resist film thickness is measured by the mechanical stylus, which is used to sense, versus a reference plane, the step height of a scratch or pattern in a resist. For accurate measurements, careful selection of stylus size, a clean scratch mark, flat wafers, and a vibration-free table are necessary.

The final film thickness and film thickness uniformity are a strong function of fluid viscosity, final spin speed, and final spin time. The dispense volume, dispense speed, and spin acceleration do not affect the average final film thickness much⁽⁷⁰⁾. The average final film thickness as a function of final spin speed for the Shipley 90104C resist is shown in Figure 7.2.

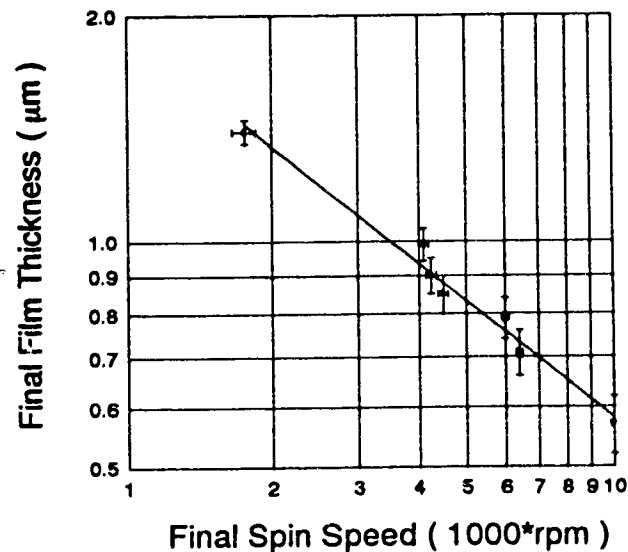


Figure 7.2. Dependence of resist thickness on the spin speed for XP90104C.

7.3 Etch rate of XP90104C resist

7.3.1 Experimental details

The XP90104C was first characterized in terms of the dependence of etch rate on the x-ray flux. The XP90104C resist was spun at 1750 rpm for 60 seconds to a thickness of $1.45\text{ }\mu\text{m}$ on a silicon wafer and prebaked at a temperature of $110\text{ }^{\circ}\text{C}$ for 60 seconds. Exposures were carried out in 640 torr of flowing helium at distance of 4 cm from a copper source plasma at an angle of 60° relative to target normal. The laser was incident at 45° relative to target normal. Exposures are in the range of 0.5 to 10 mJ cm^{-2} , corresponding to 200 to 3000 laser shots at 20 Hz. A filter consisting of four layers of B10 filter material (each consisting of $0.165\text{ }\mu\text{m}$ of Aluminum on $2\text{ }\mu\text{m}$ polycarbonate substrate) was used in front of the resist samples to ensure that no soft x-rays or UV radiation were incident on the resist. An $80\text{ }\mu\text{m}$ thick nickel mask with 0.5 mm diameter holes was used to give exposed and non-exposed regions.

Each run consists of four resist samples exposed to the same x-ray flux desired and post-exposure baked at $110\text{ }^{\circ}\text{C}$ for one minute in a vacuum hot plate to allow the desired reactions to continue to completion. Samples are then developed for 25 seconds, 50 seconds, 75 seconds and 100 seconds respectively in MF-312 developer. The resultant step heights in the resist samples were measured using a mechanical stylus profile monitor as shown in Figure 7.3.

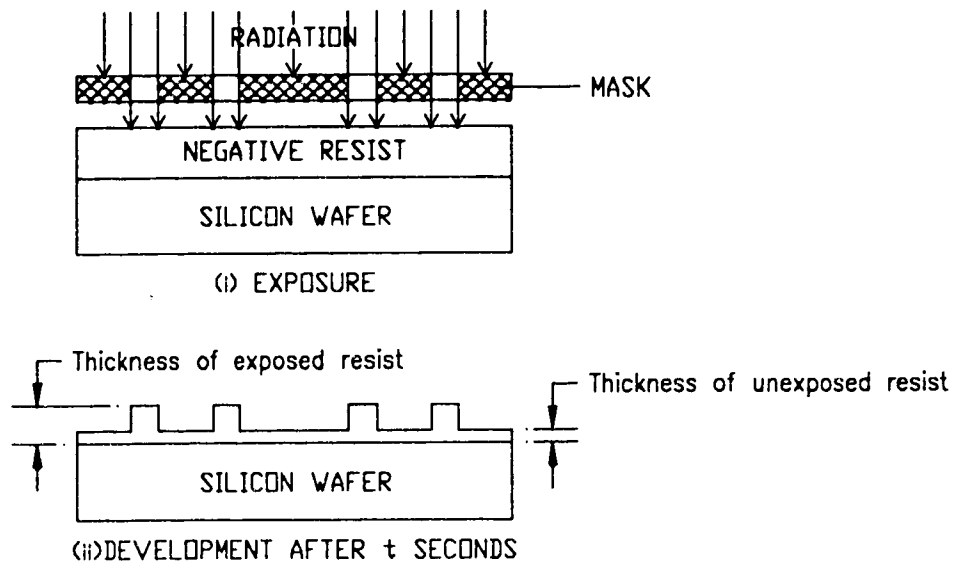
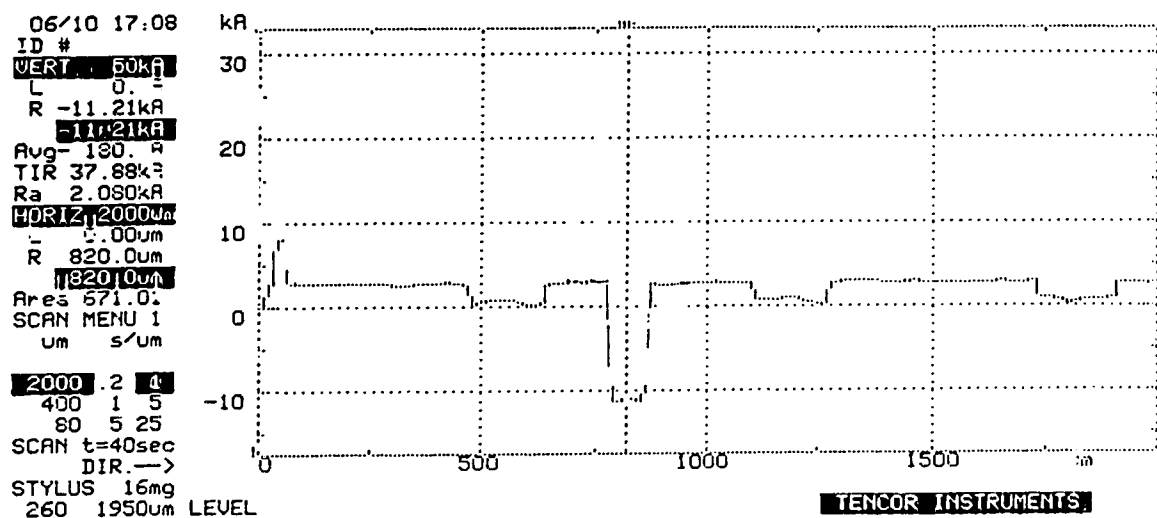
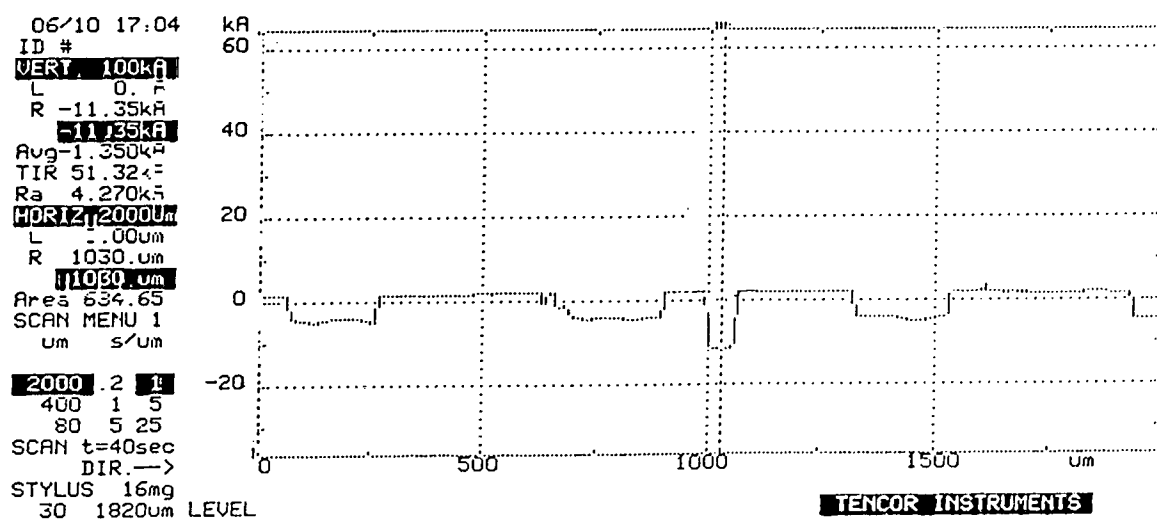


Figure 7.3. Measurement of the resist thickness as a function of time.

A typical stylus profile monitor trace is shown in Figure 7.4 in which a scratch is made on the surface of the wafer acts as a reference.



(a)



(b)

Figure 7.4. Stylus profile monitor trace using 6 mJ cm^{-2} at (a) 25s and (b) 50s.

7.3.2 Results

A graph of the thickness of resist remaining for the exposed and unexposed regions versus development time is constructed. A graph showing the result for an exposure of 2 mJ cm^{-2} is shown in Figure 7.5.

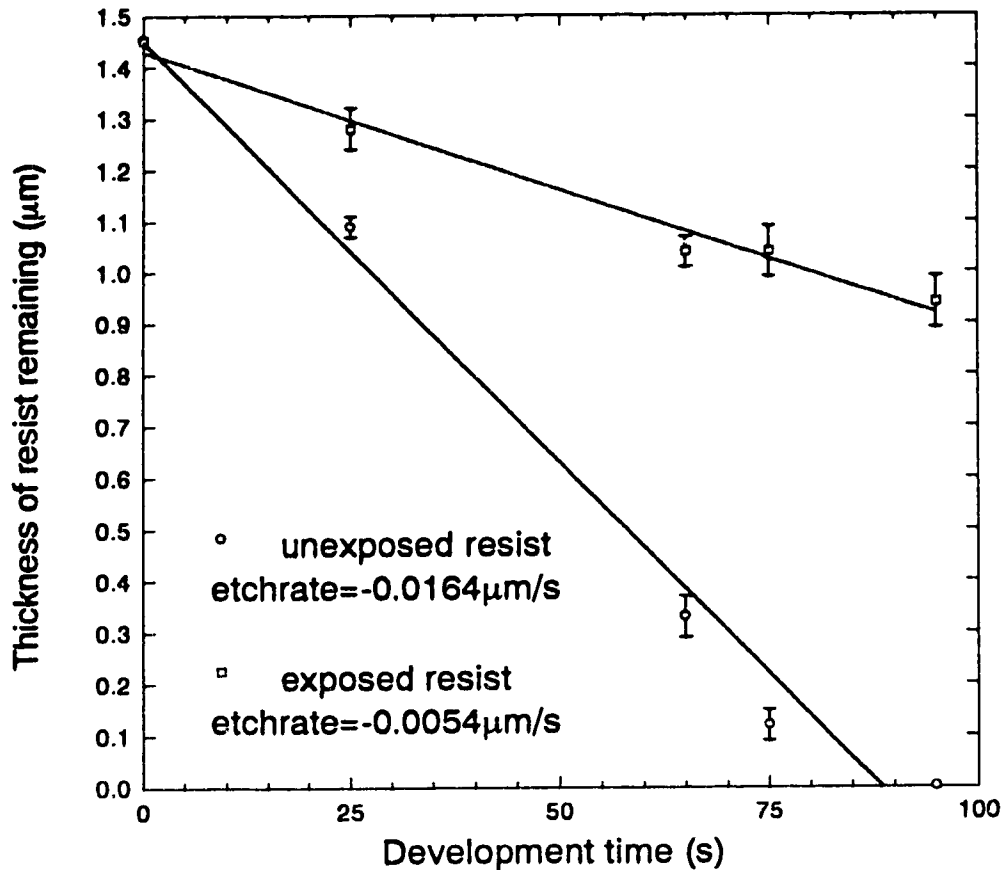


Figure 7.5. Dissolving of exposed (2 mJ cm^{-2}) and unexposed resist with time.

The dissolution rate can be calculated by finding how much the resist was etched away in the exposed region divided by the development time, that is, given by the slope of the etch rate curve.

The same procedure is repeated for exposure of 0.5, 1, 2, 3, 4, 5, 6, 7, 8, 9 and 10 mJ cm^{-2} . Each exposure level was repeated twice to ensure more accurate measurements. The result showing the effect of x-ray flux on the dissolution rate is shown in Figure 7.6.

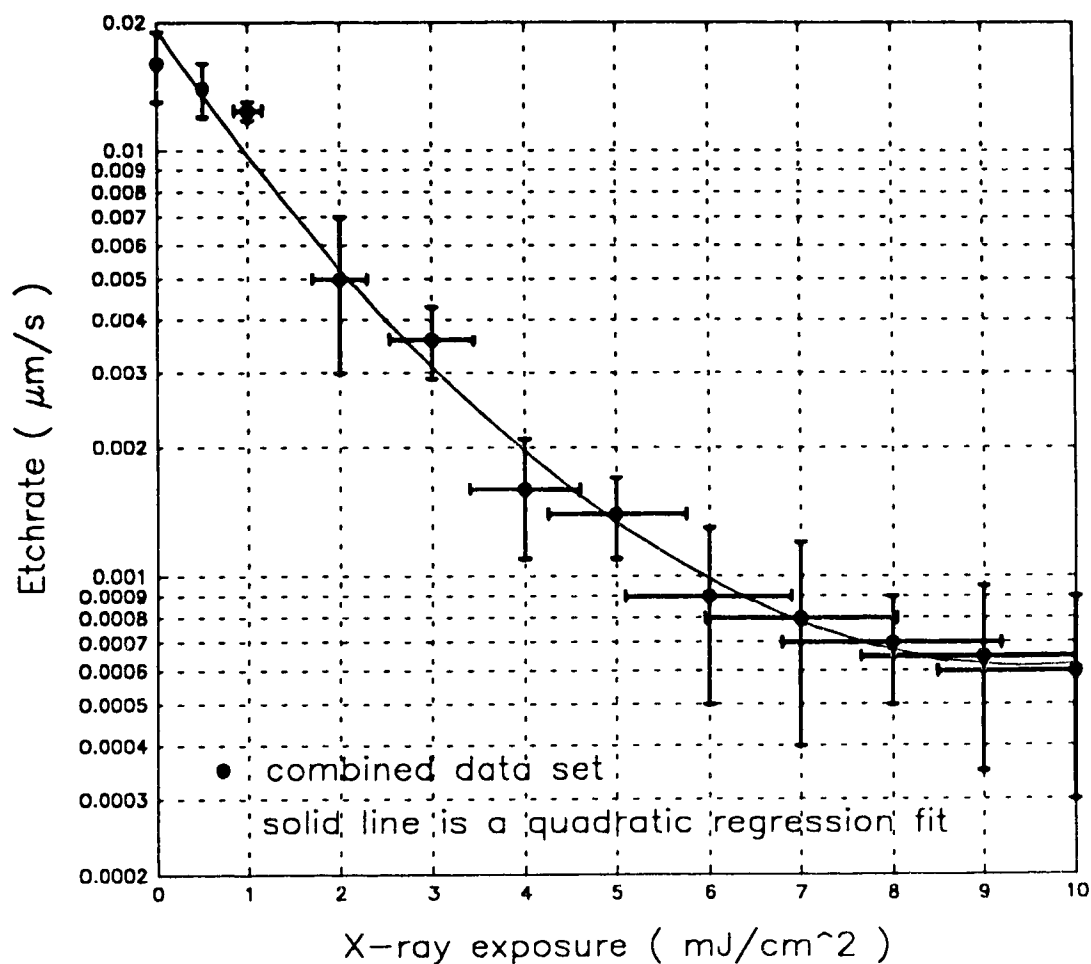


Figure 7.6. Dissolution rate as a function of surface x-ray flux for XP90104C resist.

7.4 Plasma etch resistance of XP90104C

Two samples of Shipley XP90104C negative resist were exposed to 6 and 10 mJ cm⁻² and etched in an isotropic plasma etch using SF₆ (300 watts and 200 mtorr) for 6 minutes to study the plasma etch rate of the exposed resist and silicon wafer. It was found that the etch rate is 0.045 ± 0.002 µm/min for the exposed resist and 1.73 ± 0.06 µm/min for the silicon wafer. Thus the XP90104C resist is quite resistant to plasma etching. Figure 7.7 shows the resist and silicon wafer after plasma etching. The top layer is the Shipley resist exposed to 6 mJ cm⁻² after development. It can be seen that the silicon wafer was undercut due to extreme over etching.

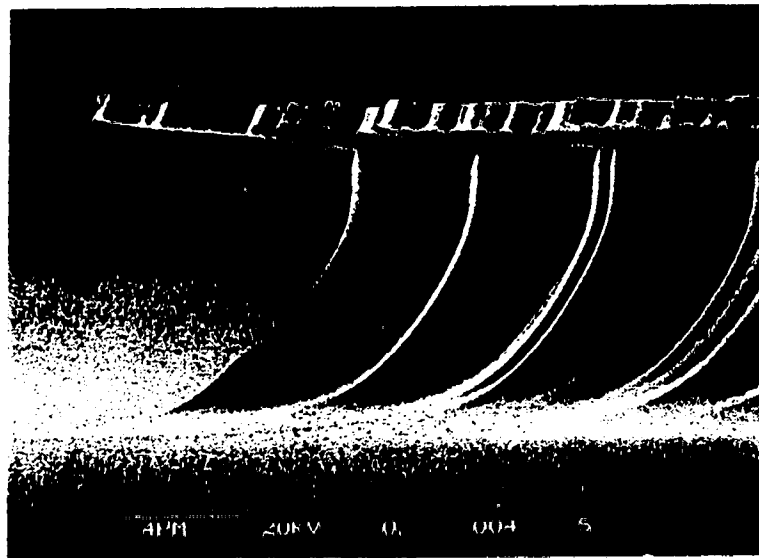


Figure 7.7. Plasma etch of XP90104C resist and silicon wafer.

7.5 Contrast and Sensitivity of XP90104C

From the etch rate curve, a graph of the resist height versus x-ray exposure can be constructed using the relation:

$$\begin{aligned}\text{Resist height} &= \text{Original resist thickness} - \text{Etch rate} \times \text{Development time} \\ &= 1.45 \mu\text{m} - \text{Etch rate } \mu\text{m/s} \times 120 \text{ s}\end{aligned}$$

The resultant plot of resist height versus exposure is shown in Figure 7.8. From the graph, the contrast and sensitivity of the XP90104C resist can be obtained.

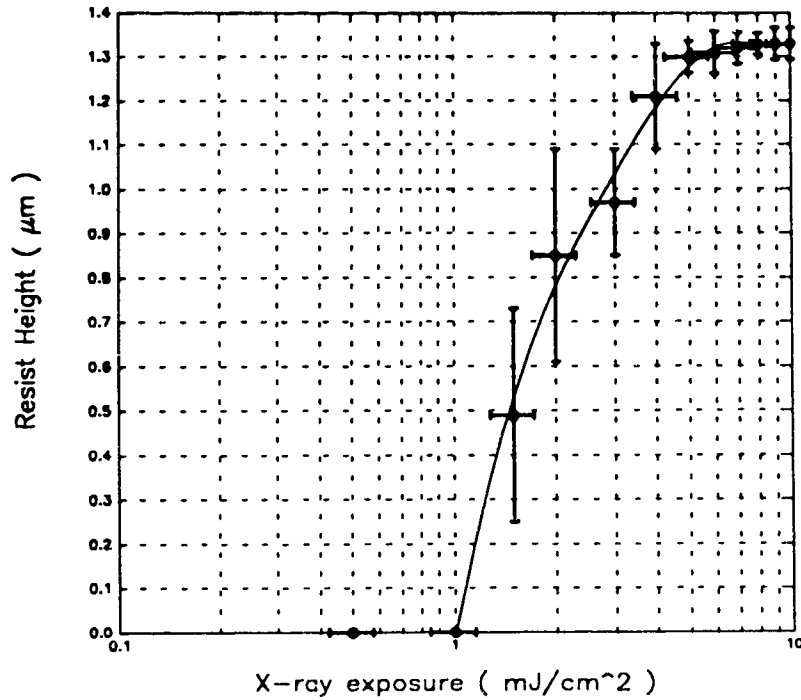


Figure 7.8. Resist height versus x-ray exposure.

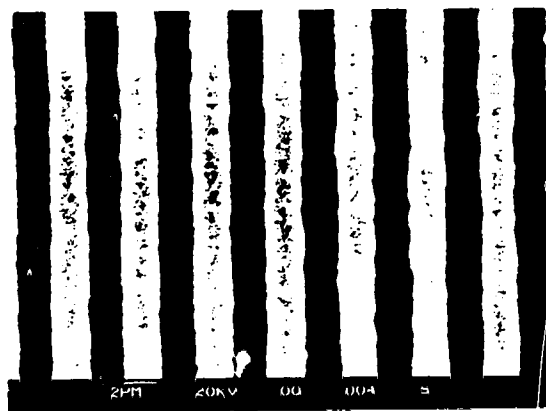
The contrast (γ) defined as the sharpness of transition from unexposed to fully exposed regions can be given by the slope of the tangent at the mid-point of the resist height in Figure 7.8, i.e. at resist height of $0.67 \mu\text{m}$. The contrast is found to be $\gamma = 3.3$ which is comparable to the value 3.81 obtained by C.P. Babcock⁽⁷¹⁾ for the same resist using a synchrotron source.

The sensitivity for the negative resist can be defined in a number of ways. For example, it can be defined by the dose where 50 - 80 % of the original resist thickness is maintained⁽⁵³⁾. For this project, the sensitivity is defined by the exposure at which 90 % of the original resist thickness is maintained⁽⁷²⁾. The sensitivity of XP90104C is 6 mJ cm^{-2} which is four times smaller than that of Babcock using higher photon energy synchrotron radiation. This discrepancy may due to different processing conditions (we use 2 minutes development but Babcock uses 3 minutes). In addition, our laser plasma spectrum is centered at 1150 eV but Babcock's synchrotron spectrum is centered at about 1700 eV. Because of the strong dependence of absorption which scales empirically as $(h\nu)^{-2.7}$ with x-ray energy for typical resist material over the range 1-2 keV, this enhanced sensitivity for laser-plasma radiation is expected.

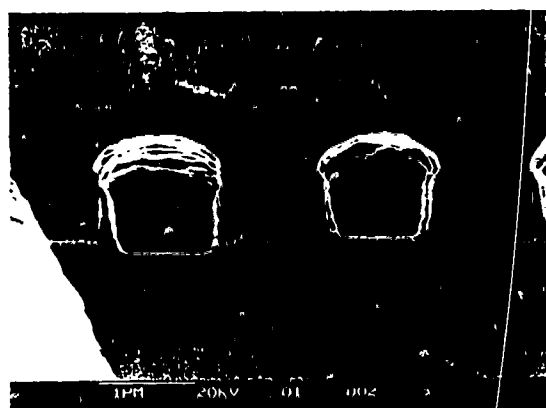
7.6 Exposure measurement on XP90104C resist for contact printing

7.6.1 Masks

The first set of exposure experiments were carried out in a contact printing geometry. The masks used to produce the patterns are 500 μm and 1000 μm free standing gold bar grating patterns. The 500 μm transmission grating provides 1 μm lines and spaces as shown in Figure 7.9. The 1000 μm grating gives approximately 0.3 μm spaces and 0.7 μm lines where the grating bars contact the larger support structure as shown in Figure 7.10. As can be seen, the grating spacing is non-uniform in the region where the grating bars are free standing between the larger support bars. The grating bars themselves are almost square in cross-section with a slightly rounded profile with a thickness of about 0.9 μm for the 500 μm grating and 0.6 μm for the 1000 μm grating. The overall grating support structure is only on the order of 1 μm thick leading to very fragile structures.

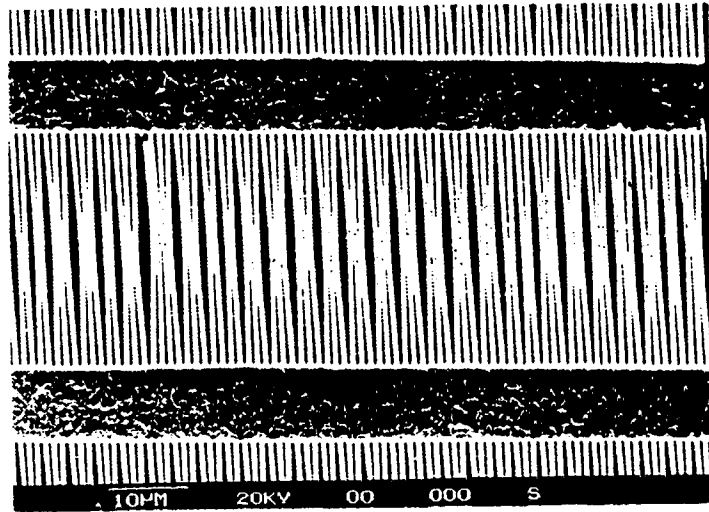


(a)

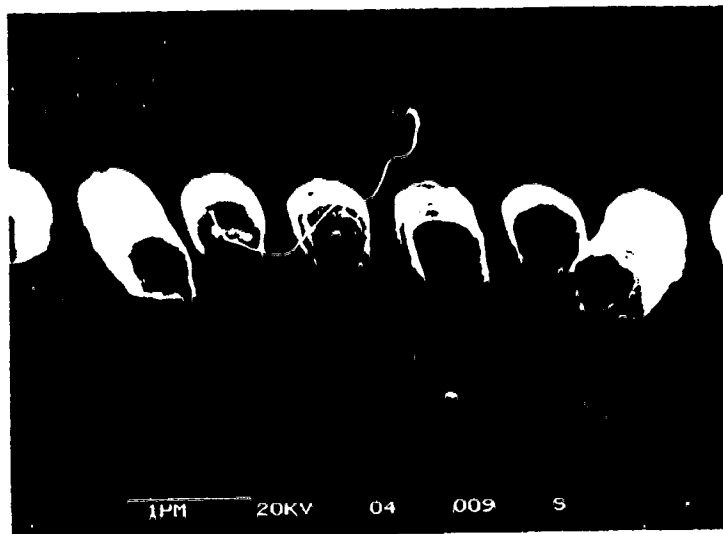


(b)

Figure 7.9. 500 μm free standing gold bar grating (a) top view and (b) cross-section.



(a)



(b)

Figure 7.10. 1000 μ /mm free standing gold bar grating (a) top view and (b) cross-section.

7.6.2 Experimental details

The XP90104C resist was spun at 1750 rpm (for thick resist) or 6400 rpm (for thin resist) for 60 seconds to achieve a film thickness of 1.4 or 0.7 μm , then prebaked 60 seconds at 110 $^{\circ}\text{C}$. Exposures were carried out in 640 torr of flowing helium at distances of 3 cm to 8 cm from a copper source plasma at an angle of 60 $^{\circ}$ relative to target normal. A filter consisting of four layers of B10 filter material was used in front of the resist samples to eliminate the UV light and softer x-rays. The mask is in direct contact with the resist coated wafer and there is a 75 μm thick nickel mesh with 0.5 mm holes, on top of the mask to keep the grating mask flat. Even so, it is expected that the mask pattern was not in intimate contact everywhere on the surface with estimated mask to wafer gaps ranging from 0 μm to $\sim 10 \mu\text{m}$. The mounting of the resist and mask is shown in Figure 7.11.

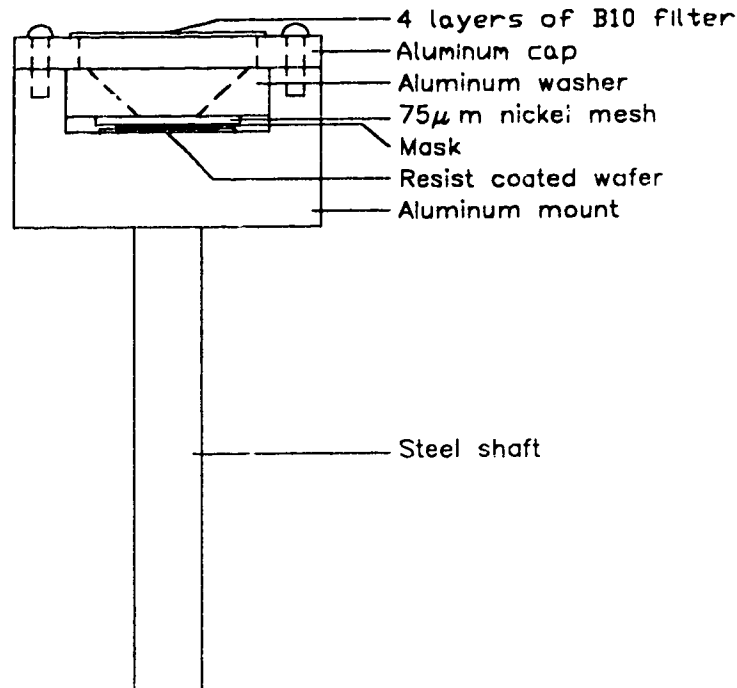


Figure 7.11. Mounting of the resist sample and mask.

The laser was fired at high repetition rate (20 Hz) and each exposure consisted of 200 to 5000 laser shots depending on the exposure level desired. After exposure, the samples were post baked on a vacuum hot plate at a temperature of 110 $^{\circ}\text{C}$ for 60 seconds. They were developed in Microposit MF-312 CD-27 developer for 2 minutes, rinsed in water for 40 seconds and then dried by nitrogen gas.

7.6.3 Results for thick resists

The wafers are coated with $1.4\text{ }\mu\text{m}$ thick resist and exposed to a range of incident fluxes from 2 mJ cm^{-2} to 12 mJ cm^{-2} at the surface of the resist in order to find optimum exposure conditions. Typical results using $500\text{ }\mu\text{m}$ mask are shown in Figure 7.12 to 7.16. For the fine grating only an exposure at 7.0 mJ cm^{-2} is shown in Figure 7.17.

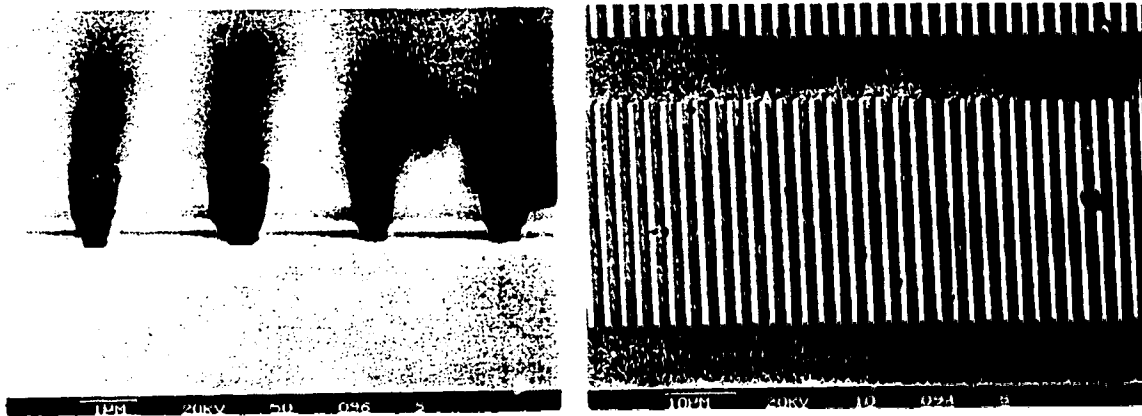


Figure 7.12. Thick resist profile using $500\text{ }\mu\text{m}$ mask and 2.5 mJ cm^{-2} exposure flux.

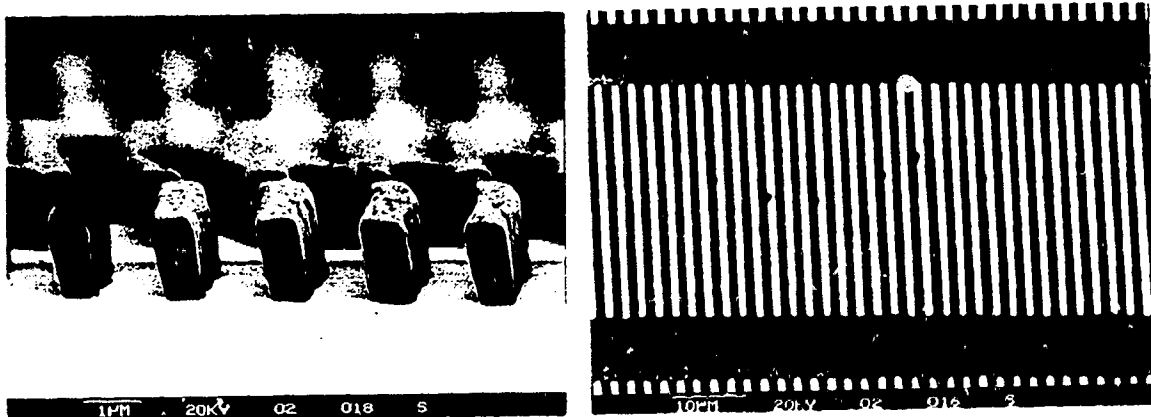


Figure 7.13. Thick resist profile using $500\text{ }\mu\text{m}$ mask and 3.8 mJ cm^{-2} exposure flux.

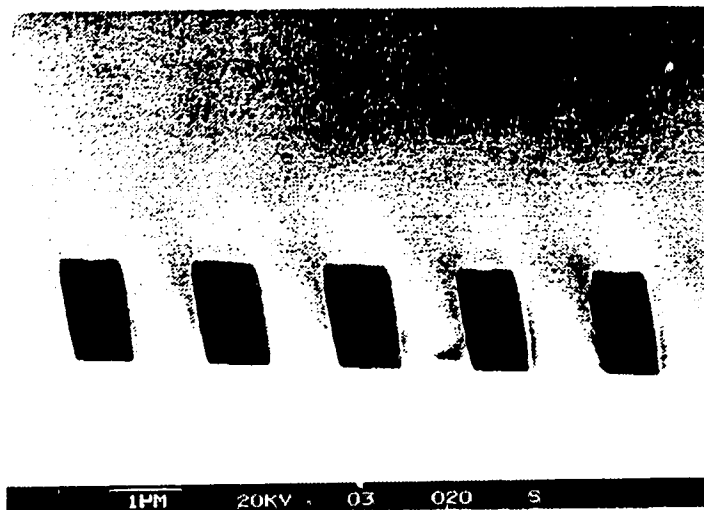


Figure 7.14. Thick resist profile using 500 μ m mask and 5.0 mJ cm⁻² exposure flux.

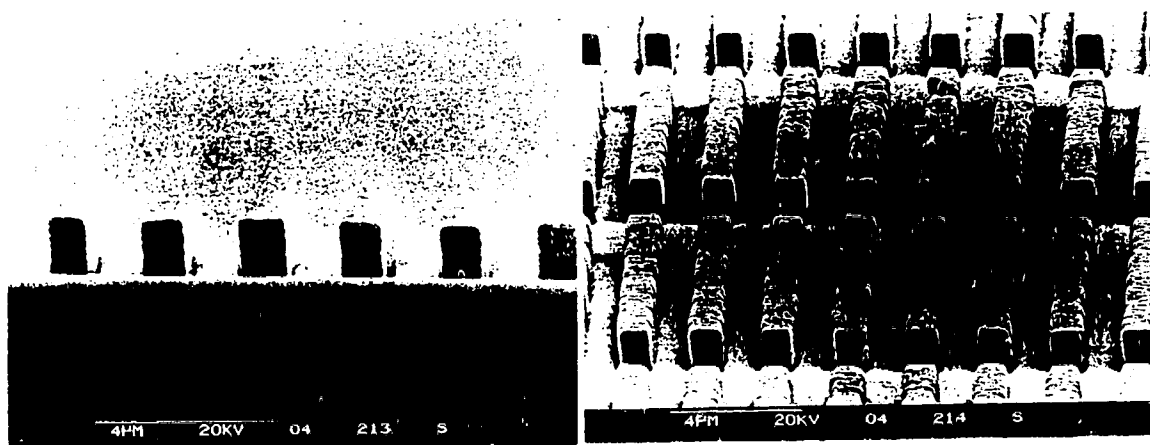


Figure 7.15. Thick resist profile using 500 μ m mask and 7.0 mJ cm⁻² exposure flux.

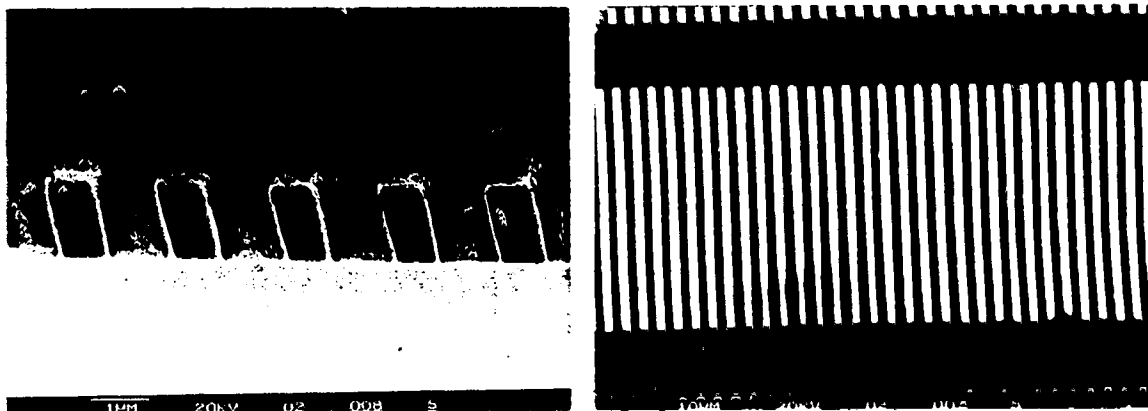


Figure 7.16. Thick resist profile using 500 μ m mask and 9.0 mJ cm^{-2} exposure flux.

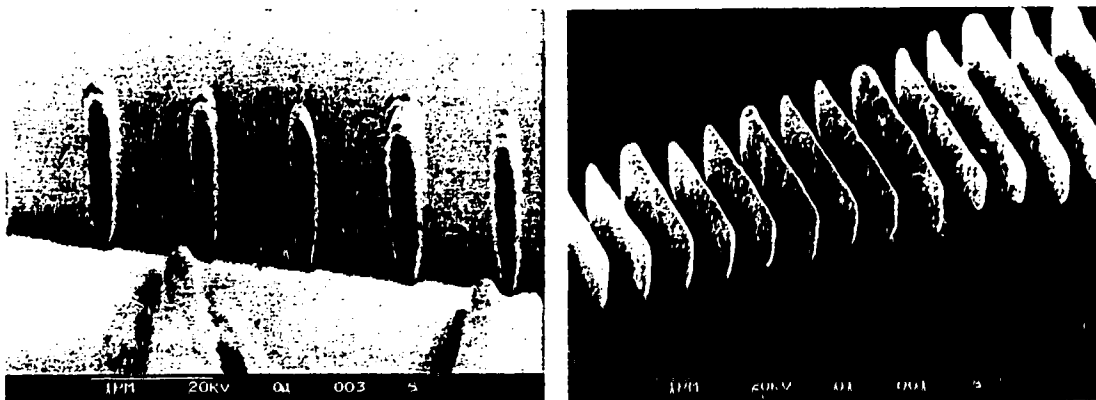


Figure 7.17. Thick resist profile using 1000 μ m mask and 7.0 mJ cm^{-2} exposure flux.

Among various exposure levels, 7 mJ cm^{-2} seems to be the optimum x-ray flux for the best replication of patterns in XP90104C resist.

7.6.4 Results for thin resists

The wafers are coated with $0.7\text{ }\mu\text{m}$ thick resist and exposed to a wide range of exposure from 7 mJ cm^{-2} to 30 mJ cm^{-2} at the surface of the resist in order to find optimum exposure conditions. The results of using $1000\text{ }\mu\text{mm}$ grating as the mask are shown in Figures 7.18 - 7.24.

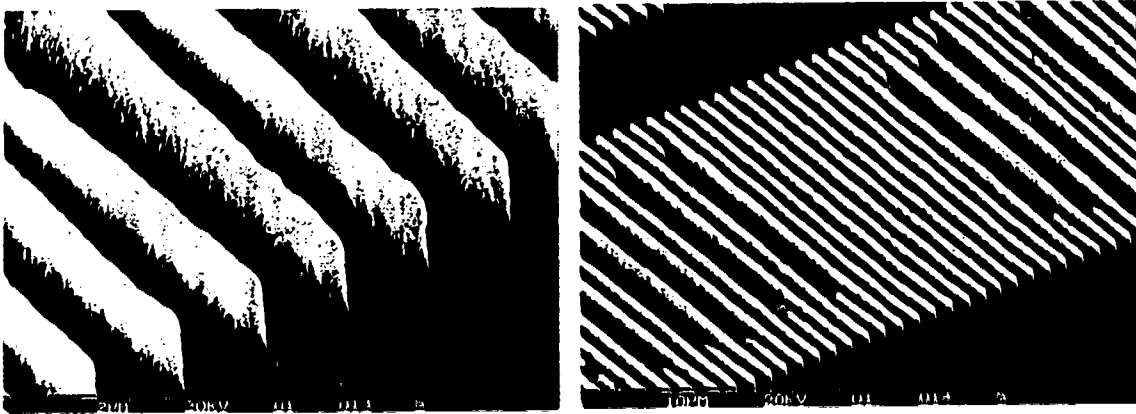


Figure 7.18. Thin resist profile using $1000\text{ }\mu\text{mm}$ mask and 7.0 mJ cm^{-2} exposure flux.

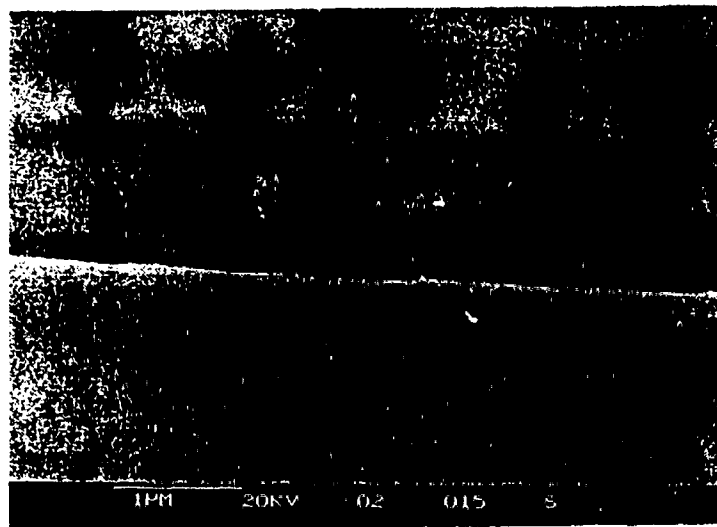


Figure 7.19. Thin resist profile using $1000\text{ }\mu\text{mm}$ mask and 9.0 mJ cm^{-2} exposure flux.

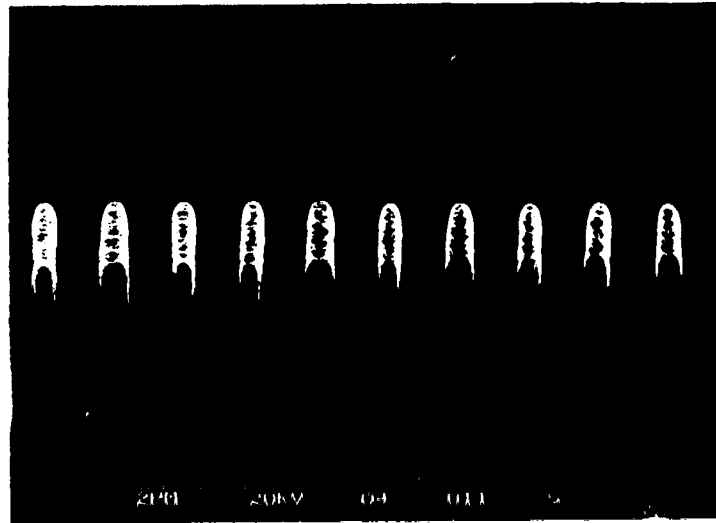


Figure 7.20. Thin resist profile using 1000 μm mask and 13.0 mJ cm^{-2} exposure flux.

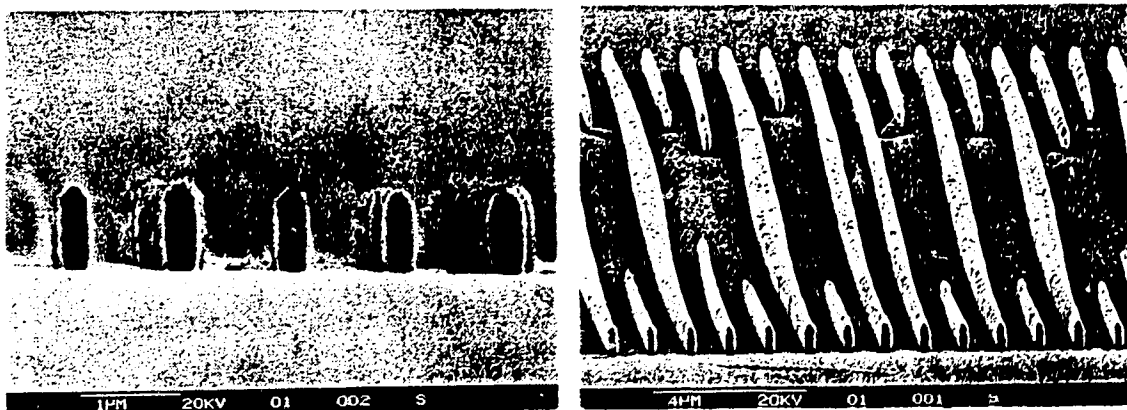


Figure 7.21. Thin resist profile using 1000 μm mask and 15.0 mJ cm^{-2} exposure flux.

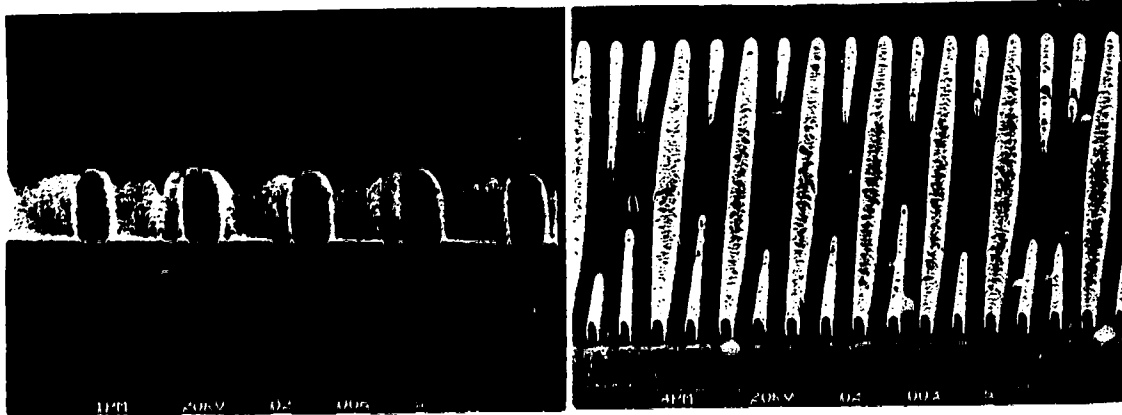


Figure 7.22. Thin resist profile using 1000 μm mask and 20.0 mJ cm^{-2} exposure flux.

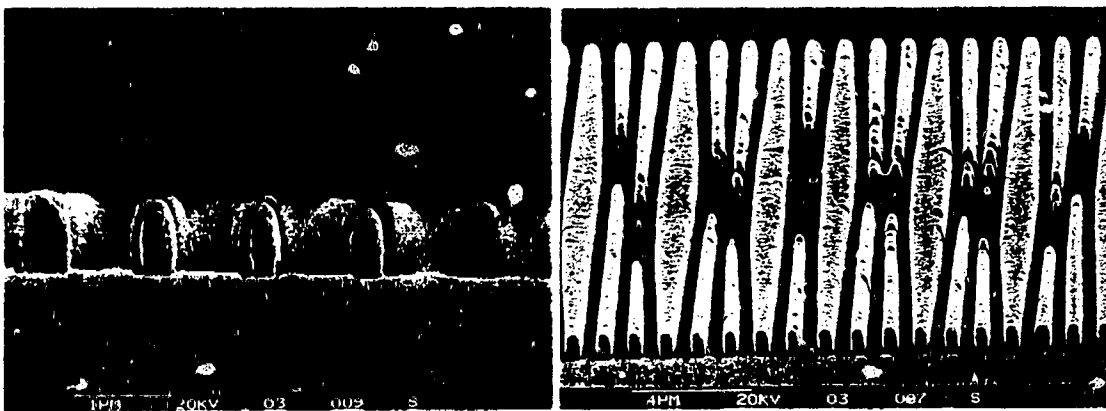


Figure 7.23. Thin resist profile using 1000 μm mask and 25.0 mJ cm^{-2} exposure flux.

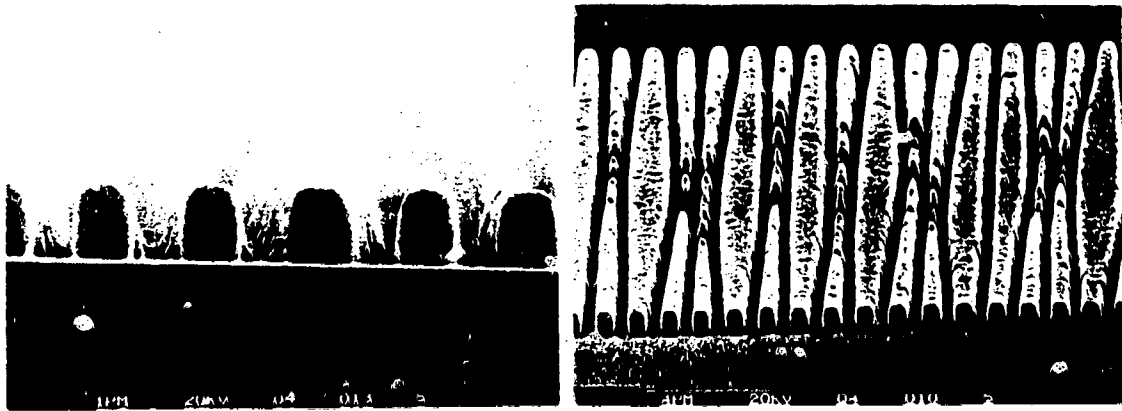


Figure 7.24. Thin resist profile using 1000 μm mask and 30.0 mJ cm^{-2} exposure flux.

It can be seen from Figure 7.12 to 7.24 that the lines become narrower than the original mask pattern for low incident fluxes. If the exposure is too low, only the center part of the line profile which receives the peak exposure remains after processing. The underexposed resist samples also show undercutting which may be due to the surface contamination. On the other hand, if the incident flux is too high, the lines become fat and merge together due to the leakage of the incident flux in the opaque mask region.

The best operating exposure window to obtain $\sim 0.2 \mu\text{m}$ linewidth is in the range of $7 - 9 \text{ mJ cm}^{-2}$.

7.7 Effect of Fresnel diffraction on the resist profile

This set of experiments studies the effect of diffraction of the x-ray on the resist profile. The Fresnel diffraction⁽⁷³⁾ depends on the linewidth (w) of the opening of the mask , the separation between mask and resist (gap, g) and the wavelength (λ) of the exposing radiation. A key parameter for determining the diffraction effect is the Fresnel Number, N , which is defined as the number of Fresnel zones within the aperture. The Fresnel number is given by equation (2.6) and rewritten:

$$N = \frac{a^2}{g\lambda} \quad (7.1)$$

where $a = w/2$ is the half linewidth.

For high resolution tests, we used 1000 μm mask which consisted of 0.3 μm spaces and 0.7 μm bars at the edge of the pattern so the half linewidth equals 0.15 μm . For laser produced plasma, the wavelength λ of the x-ray radiated will be about 1 nm. The only parameter left determining the Fresnel diffraction will be the gap between the mask and the resist.

Resist samples were prepared with different mask to wafer gaps and exposed to the same x-ray flux of 9 mJ cm^{-2} . The spacer was made of either mylar plastic or aluminum foil. They were both rectangular in shape with a hole of diameter 2 mm in the middle for x-rays to pass through. The gap was set with a single mylar spacer or by combining the mylar and aluminum foil to achieve the desired spacing.

As the Fresnel number increases at certain values multiple peaked diffraction patterns are expected. An attempt was made to observe this behaviour. In particular a gap spacing was sought to give a doubling of the grating period. From the Fresnel diffraction calculation exposure profiles were calculated for different gap spacings as shown in Figure 7.25.

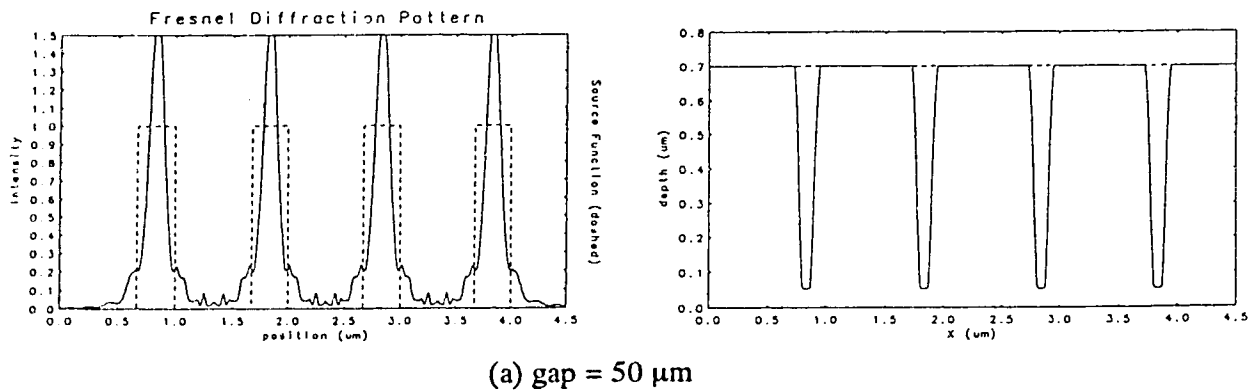
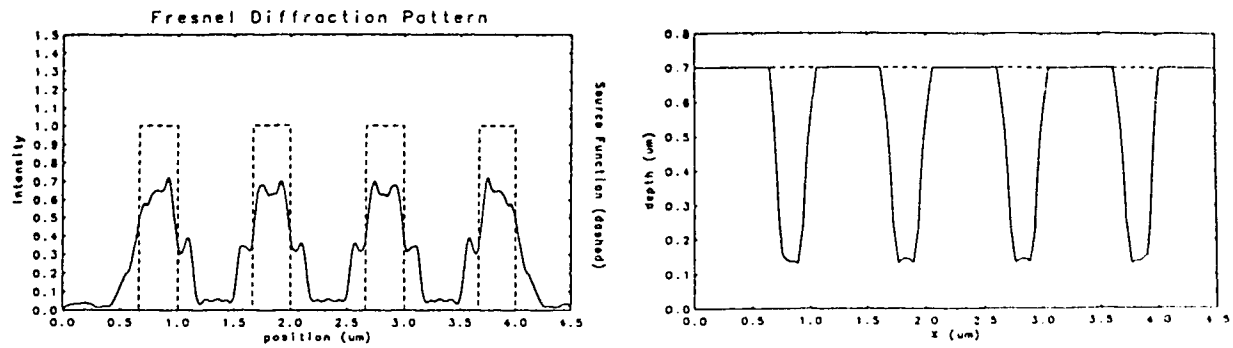
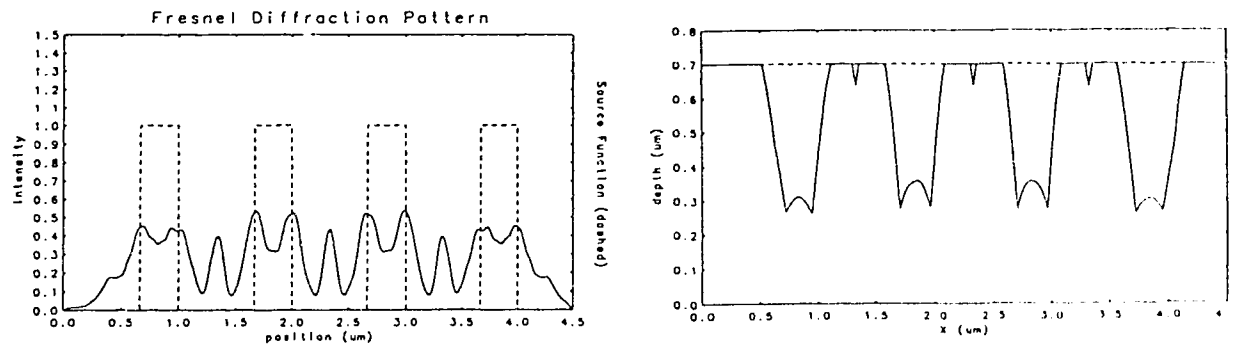


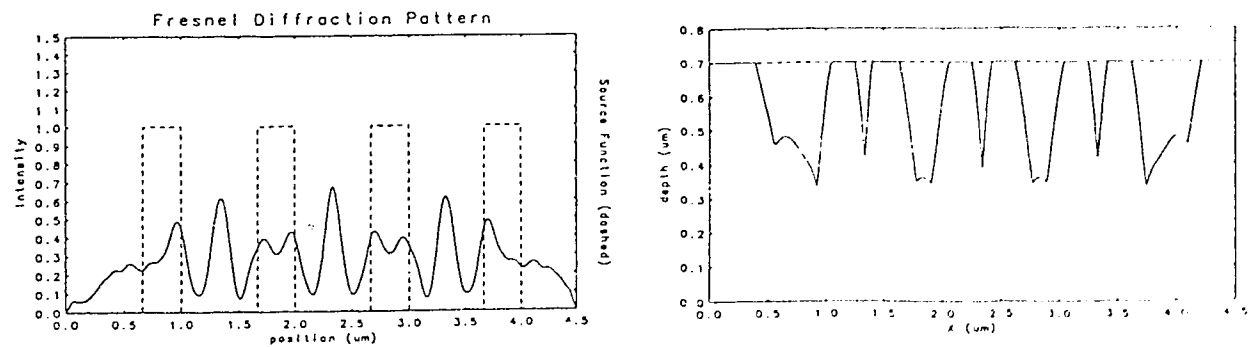
Figure 7.25. Calculated diffraction (left) and resultant resist profile (right) patterns. versus mask to wafer gap.



(b) gap = 150 μm



(c) gap = 250 μm



(d) gap = 350 μm

Figure 7.25. Calculated diffraction (left) and resultant resist profile (right) patterns.
versus mask to wafer gap.

From these calculations frequency doubling is expected to occur at a gap spacing of $350\text{ }\mu\text{m}$ which corresponds to $N = 0.054$. In general it was found to be difficult to produce multiple line features in the resist because of the lack of accurate control of the mask to wafer gap spacing and also the penumbra blur due to the finite plasma size. The penumbra blur, δ , is given by $(gS)/L$ in equation 2.3, where g is the mask to wafer gap, S is the diameter of the plasma source and L is the separation between plasma and the mask. For a sample with $400\text{ }\mu\text{m}$ mask to wafer gap situated at 4 cm from the plasma of diameter $20\text{ }\mu\text{m}$, the penumbra burr is calculated to be $0.2\text{ }\mu\text{m}$. In addition, the blurring of the image due to diffusion of the acid catalyst species during post exposure bake is estimated to be $0.1\text{ }\mu\text{m}$. Taking the r.m.s. of penumbra blurring and diffusion blurring, the combined blurring is $0.22\text{ }\mu\text{m}$ which will obscure the observation of clear single lines. The penumbra blur can be minimized by increasing the separation between the plasma point and the resist samples. The best result obtained at an exposure of 9 mJ cm^{-2} for a sample sitting at 10 cm from the plasma and at a gap spacing of $350\text{ }\mu\text{m}$ is shown in Figure 7.26. In this exposure a modulation of the resist profile is observed with a period of $0.5\text{ }\mu\text{m}$, double the original period. However, clear single lines as predicted by the simulation calculation were not observed. This may be due to a number of factors. Firstly, the rounded profile of the grating gives a gradient transmission of the x-rays. Thus the mask gives a variable intensity source function instead of a slit function as assumed in the simulation code. Knowledge of the exact transmission function of the grating is needed to correct this. Secondly, the diffusion of the catalyst species, which is not taken into consideration in the code, may widen out the thin structures. Thirdly, the etchant solution may have difficulty in getting through the narrow channel between the thin structures to dissolve the resist.

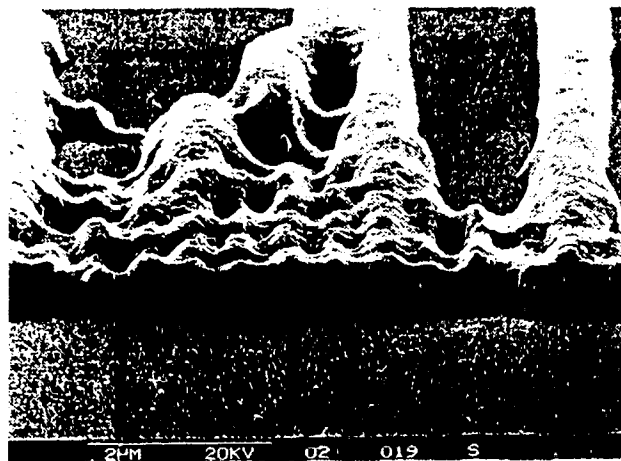
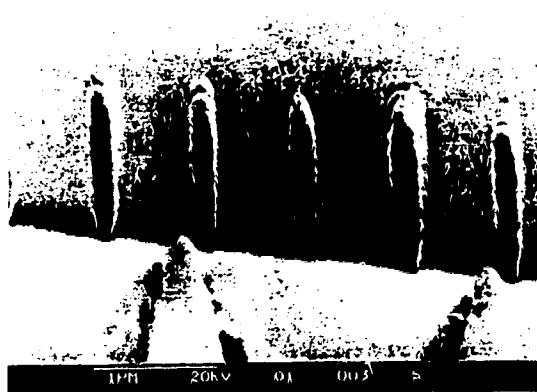


Figure 7.26. Diffraction effect for $350\text{ }\mu\text{m}$ spacing at 9 mJ cm^{-2}

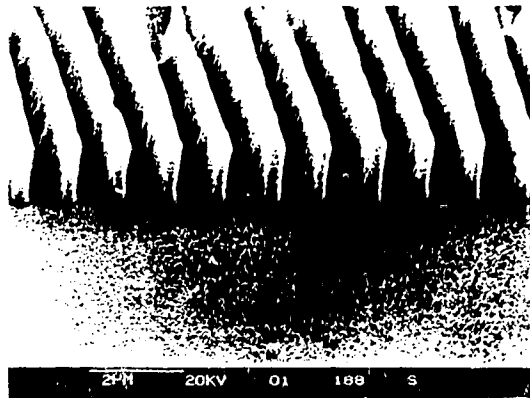
7.8 Effect of vapor prime of the wafer on the resist profile

In many of the initial exposure tests no vapor prime was used to clean the wafer before exposure. However the resultant resist patterns always showed signs of undercutting indicating contamination of the contact surface between the resist and the wafer. Thus it was determined that the wafer should be cleaned and vapor primed prior to coating of the resist to enhance the adhesion. This is done in a vacuum bake/vapor prime system using the HMDS as the adhesion promotor. The detailed steps are described in appendix 2

The resist profiles with and without vapor prime process are shown in Figure 7.27. The lineshape without vapor prime shows undercutting at the surface of the wafer presumably due to the contamination of the interface by organic impurities whereas the better cleaning procedure shows less undercutting.



(a)



(b)

Figure 7.27. 0.2 μ m lineshape (a) without vapor prime and (b) with vapor prime process.

7.9 Resolution of the XP90104C

The Shipley 90104C has been fully characterized in terms of the spincoat, etch rate, development time, exposure dose and various processing parameters. By using the best processing condition as given in appendix 2 and the optimum exposure flux of 7 mJ cm^{-2} , various linewidths can be replicated using the 500 μm and 1000 μm grating as indicated in Figure 7.28 - Figure 7.33 . The 500 μm grating is used to produce $1 \mu\text{m}$ linewidths for the initial test. For fine linewidths, the 1000 μm grating is used. Because the gold bars in the 1000 μm grating are slightly curved, the spaces between bars vary in width (refer to Figure 7.10). Different areas of the mask have different widths for transmission of the x-rays. Therefore different linewidths can be obtained by choosing different portions of the grating mask. The finest linewidth achieved by mounting two masks on top of each other to give a distribution of linewidths below $0.3 \mu\text{m}$ was 100 nm.

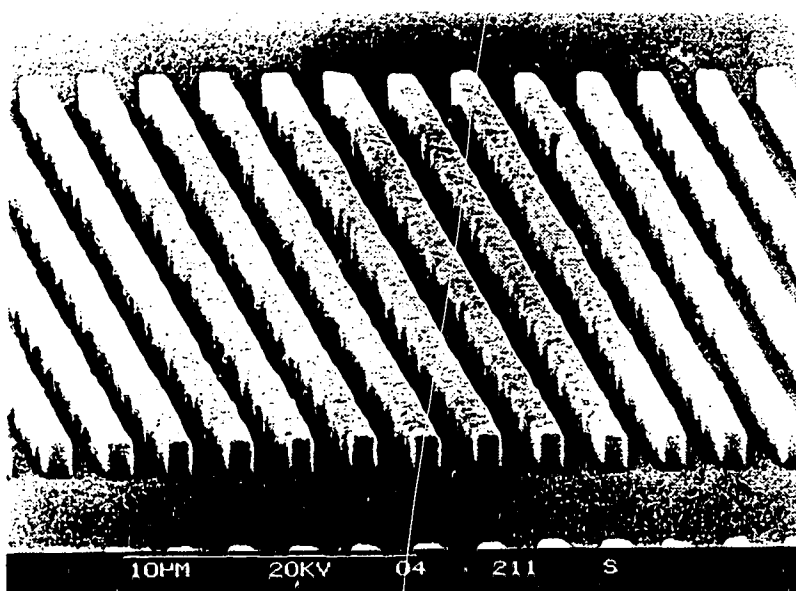


Figure 7.28. $1 \mu\text{m}$ linewidth imprinted in Shipley XP90104C resist.

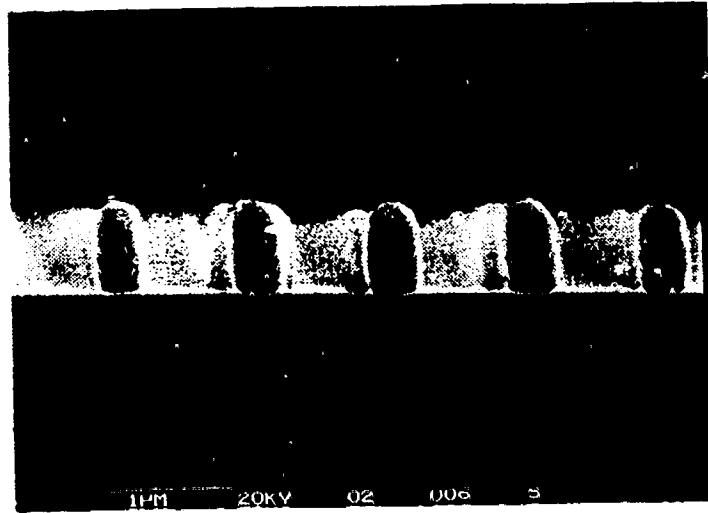


Figure 7.29. 0.3 μm linewidth imprinted in Shipley XP90104C resist.

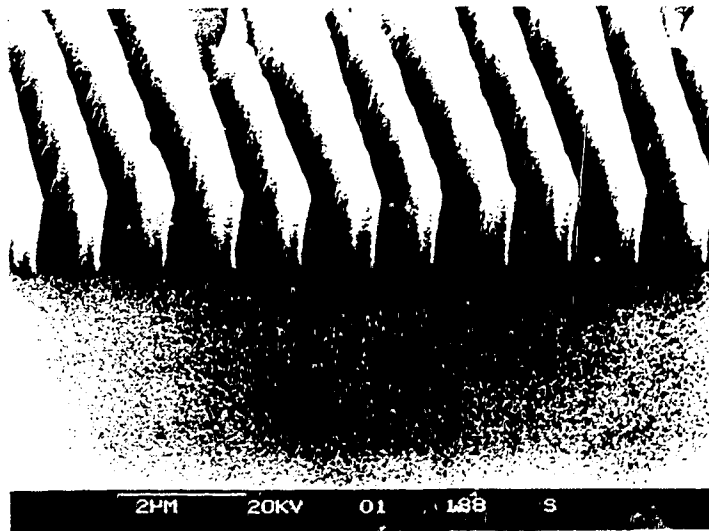


Figure 7.30. 0.2 μm linewidth imprinted in Shipley XP90104C resist.

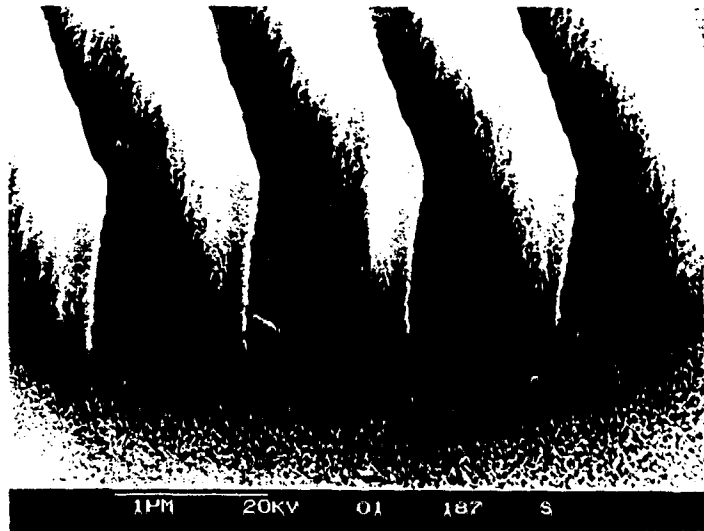


Figure 7.31. 0.15 μm linewidth imprinted in Shipley XP90104C resist.

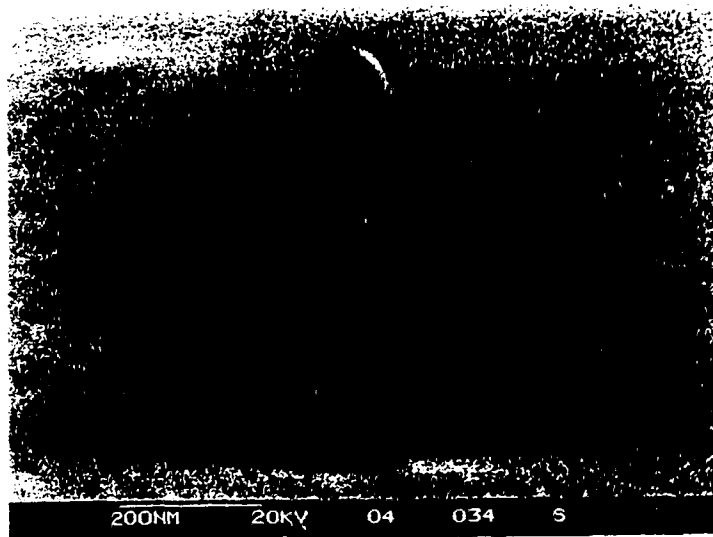


Figure 7.32. 0.1 μm linewidth imprinted in Shipley XP90104C resist using a 0.7 μm thick starting thickness of resist.

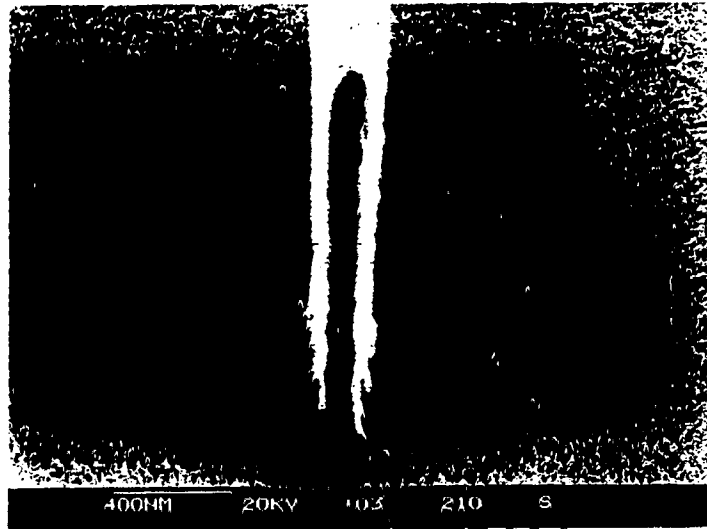


Figure 7.33. 0.1 μm linewidth imprinted in Shipley XP90104C resist using a 1.4 μm thick starting thickness of resist.

From Figure 7.32 and 7.33, the Shipley XP90104C has a resolution down to 0.1 μm with a height of 0.63 μm for thin-coated resist and 1.4 μm for the thick-coated resist. The line shape is quite straight for both thin and thick resist patterns. The aspect ratio is 14 for the later case. This high aspect ratio (14), fine linewidth (0.1 μm) and the low exposure (7 mJ cm^{-2}) demonstrate the potential feasibility of high throughput sub-nanometer pattern replication in x-ray lithography using high sensitivity x-ray resist.

Smith⁽⁹⁾ also demonstrated 0.1 μm linewidth using Hoechst PF514 resist. However, the required exposure dose is much higher ($\sim 50 \text{ mJ cm}^{-2}$) than the present characterized Shipley XP90104C resist. Typical resist sensitivity and contrast responses from some commercially amplified negative-tone resists are shown in Table 7.1.

| Resist system | Sensitivity (mJ cm^{-2}) | Contrast | X-ray source |
|--------------------------------|-------------------------------------|----------|--------------|
| Hoechst AG: AZ-PF | 50 | 7.5 | Synchrotron |
| Shipley: XP8933B | 36 | 5.4 | Synchrotron |
| Rohm and Haas/Shipley: ECX1029 | 30 | 8.9 | Synchrotron |
| Shipley: XP90104C | 6 | 3.3 | Laser-plasma |

Table 7.1. Characteristics of Commercial resists^(71, 73).

Chapter 8 : Simulation of the experimental results and prediction of process latitude

One of the aims of this thesis project was to establish the operating characteristics of a high sensitivity x-ray resist and then predict its potential operating performance in an industrial process setting. In particular, using the simulation program the allowed range of exposures and mask to wafer gap, i.e. process latitude can be calculated.

8.1 Extraction of parameters from experiment

The parameters in the simulation program XD3 can be determined by matching the experimental curve of the dissolution rate versus x-ray flux shown in Figure 7.6 for the Shipley XP90104C negative resist. Simulations are carried out using various resist parameter sets until a good fit is obtained between the measured and predicted etch rates. The parameter r_{clear} given by the resist thickness divided by the development time, is predetermined. In Figure 8.1, a comparison is shown between the calculated and measured etch rates for this resist.

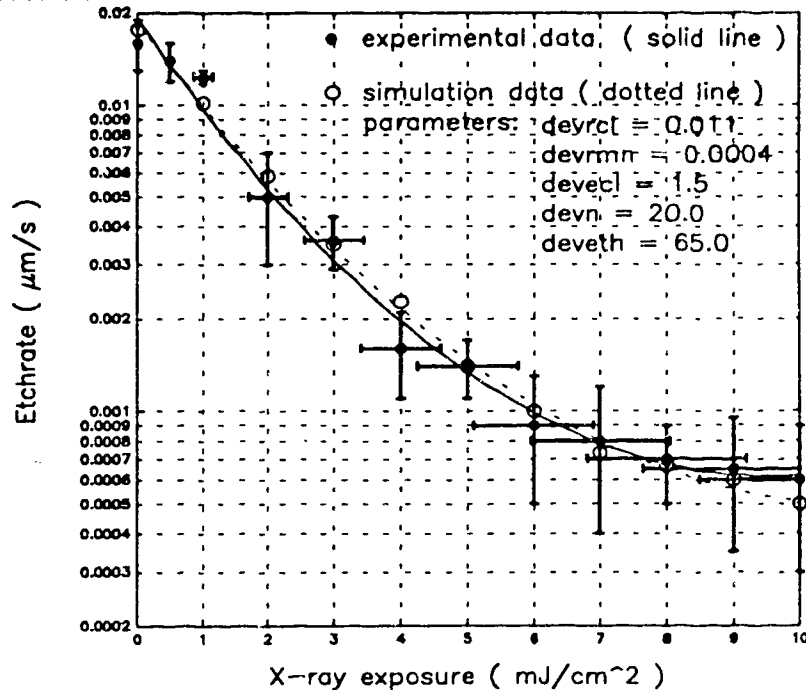


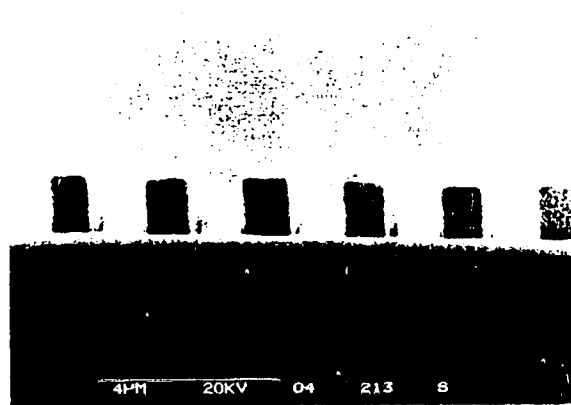
Figure 8.1. Dissolution rate as a function of surface x-ray flux, both measured (solid circles) and calculated (hollow circles).

From Figure 8.1, it can be seen that with the set of parameters shown ($r_{\text{clear}} = 0.011 \mu\text{m s}^{-1}$, $r_{\text{min}} = 0.0004 \mu\text{m s}^{-1}$, $E_{\text{clear}} = 1.5 \text{ J cm}^{-3}$, $n = 20$ and $E_{\text{th}} = 65.0 \text{ J cm}^{-3}$) the simulated etch rate calculation agrees fairly well with that measured experimentally. Once the etch rate parameters have been determined then the simulation code can be used to calculate the resist profiles for various operating conditions. These parameters were used in all the calculations which follow in this section.

8.2 Comparison of the experimental and simulated lineshape

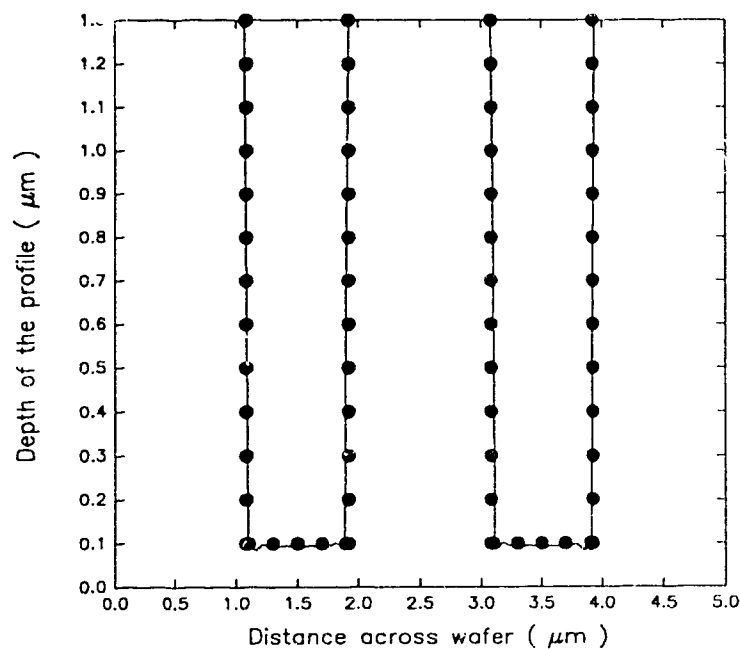
As an initial test the simulation was run to model the lineshapes measured experimentally. The following figures show the experimental and simulated results for XP90104C negative resist. In these cases an exposure gap of $5 \mu\text{m}$ was used in the simulations to account for the average estimated distance from mask to wafer.

Figure 8.2 shows a comparison with an exposure carried out with the 500 \AA/mm grating. The incident flux used in the experiment was 7 mJ cm^{-2} . The experimental lineshapes are $0.84 \mu\text{m}$ thick with a height of $1.2 \mu\text{m}$. The simulated lineshapes are $0.83 \mu\text{m}$ thick with a height of $1.2 \mu\text{m}$. It can be seen that both the simulated and experimental lineshapes agree with each other.



(a)

Experiment versus Simulation on resist profile for 1 μm linewidth



(b)

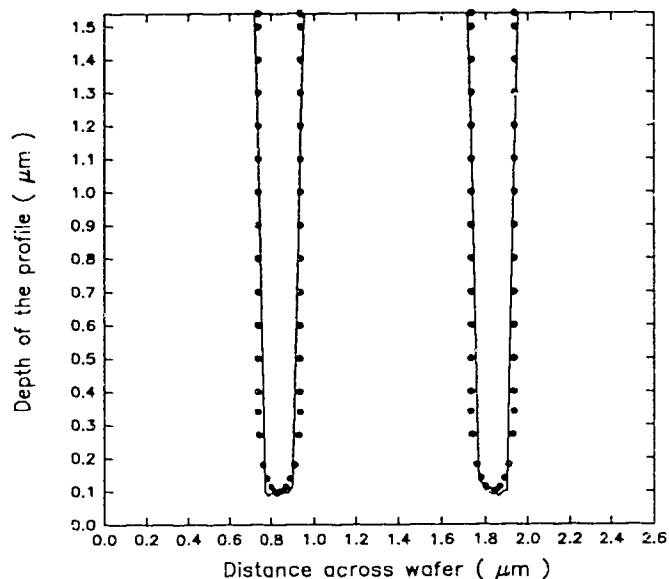
Figure 8.2. (a) Experimentally measured 1 μm lineshape at an exposure flux of 7 mJ cm^{-2} .
 (b) Comparison of the digitized experimental 1 μm line profile in XP90104C resist (solid dots) with that calculated with the XD3 simulation code (solid line).

Figure 8.3 shows a comparison with an exposure carried out with the 1000 $\text{\AA}/\text{mm}$ grating leading to a linewidth of $0.2\text{ }\mu\text{m}$. It can be seen that the simulated lineshape agrees reasonably well with the experimental lineshape. The exposure used is 7 mJ cm^{-2} and the opening of the mask is assumed to be $0.33\text{ }\mu\text{m}$ in this case.



(a)

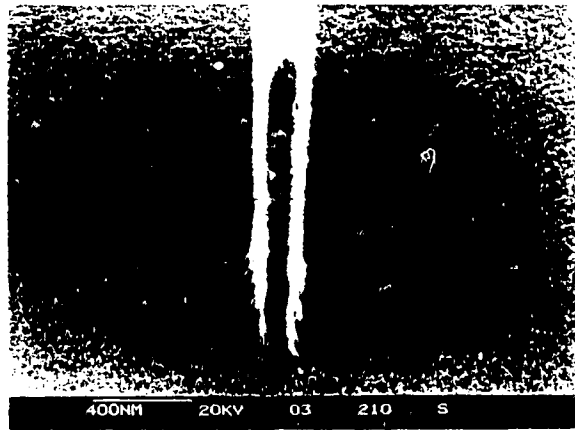
Experiment versus Simulation on resist profile for $0.2\text{ }\mu\text{m}$ linewidth



(b)

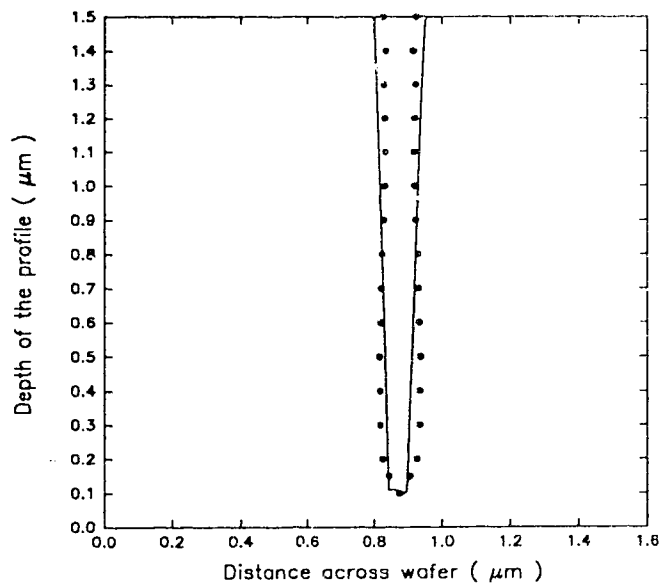
Figure 8.3. (a) Experimentally measured $0.2\text{ }\mu\text{m}$ lineshape at an exposure flux of 7 mJ cm^{-2}
 (b) Comparison of the digitized experimental $0.2\text{ }\mu\text{m}$ line profile in XP90104C resist (solid dots) with that calculated with the XD3 simulation code (solid line).

Figure 8.4 shows a comparison with an exposure carried out with the 1000 λ /mm grating leading to a linewidth of 0.1 μm .



(a)

Experiment versus Simulation on resist profile for 0.1 μm linewidth



(b)

Figure 8.4. (a) Experimentally measured 0.1 μm lineshape at an exposure flux of 7 mJ cm^{-2}
 (b) Comparison of a digitized experimental 0.1 μm line profile in XP90104C resist (solid dots) with that calculated with the XD3 simulation code (solid line).

The exposure used is 7 mJ cm^{-2} and the opening of the mask is assumed to be $0.25 \text{ }\mu\text{m}$. It can be seen that the simulated lineshape agrees qualitatively with the experimental lineshape. However the experimentally measured lineshape is thicker at the top and shows signs of some undercutting at the bottom.

From Figures 8.2 to 8.3, the simulated lineshapes predict closely the experimental profile down to $0.2 \text{ }\mu\text{m}$ and give approximate agreement at $0.1 \text{ }\mu\text{m}$. Therefore, there is reasonable confidence that the set of parameters extracted from the etch rate versus exposure curve accurately characterizes the performance of the Shipley XP90104C resist.

8.3 Process Latitude for Sub-micron Pattern Replication

In X-ray lithography the pattern is obtained by shadowgraphic replication of the mask absorber pattern onto the resist coated wafer. It is convenient to express the practical tolerances of the lithographic techniques in device fabrication in terms of a "process latitude". This figure of merit states the acceptable variation of process relevant parameters (e.g. exposure dose, proximity gap, development time, post exposure bake time, etc.) to print simultaneously a set of mask patterns varying in shape and size into the resist layer within a defined linewidth control range⁽⁷⁴⁾. For a given mask to wafer gap, features with different sizes will produce different Fresnel diffraction patterns. For all of these patterns the peak exposure region falls inside the original line boundaries. To compensate for this, in general, the linewidths on the mask pattern are made slightly larger than the desired finished linewidth. This correction factor in the design of the mask linewidths is called biasing of the linewidth.

Once the correct parameters have been determined to model a given resist then an extensive calculation of the process window for a given linewidth can be carried out. Using our parameters for the XP90104C resist we have calculated the process window for obtaining a $0.25 \text{ }\mu\text{m}$ and $0.1 \text{ }\mu\text{m}$ linewidth with a tolerance of $\pm 10\%$ in the final linewidth. The linewidth for these calculations has been defined as the width of the resist pattern at a height of $0.3 \text{ }\mu\text{m}$ from the wafer surface. These calculations have been carried out for the laser produced plasma x-ray source and a synchrotron x-ray source respectively. This can be done assuming different biases, that is starting linewidths in the mask which are slightly bigger than the desired final linewidth. In the following subsections Figures 8.5 - 8.10 and Figures 8.12 - 8.17 show predicted lineshapes at specified mask to wafer gaps and the boundaries of the exposure range which will result in the desired linewidth for different biases. Acceptable exposures are those which fall inside the two bounds shown on the exposure plots.

8.3.1 Process latitude for a laser-plasma x-ray source

(i) 0.25 μm linewidth

The exposure-gap plots with 0.0, 0.05 and 0.1 μm bias to achieve $0.25 \pm 10\%$ linewidth using the laser-plasma source are shown in Figures 8.5 - 8.7.

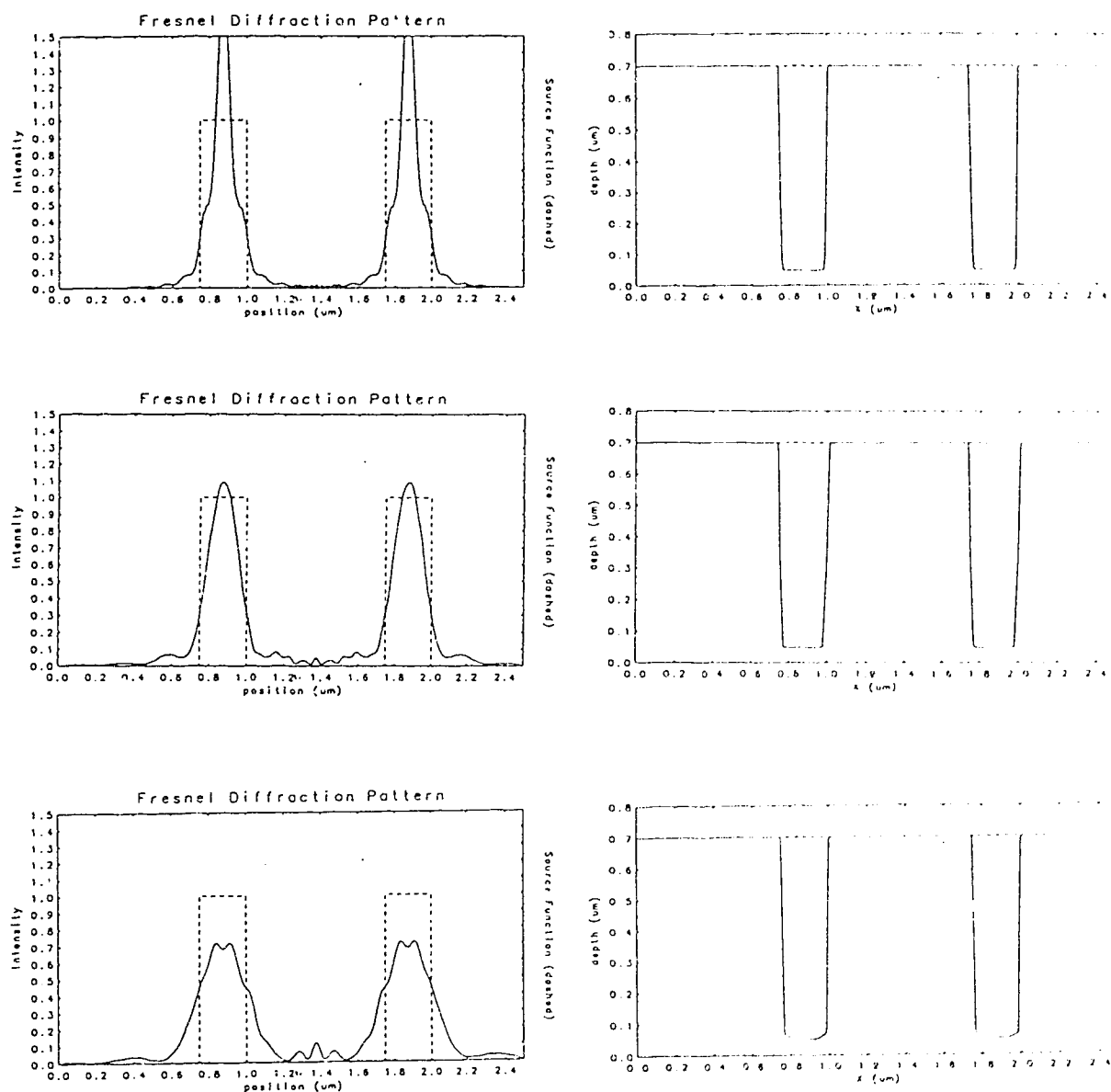


Figure 8.5. (a) Fresnel diffraction pattern and resultant resist lineshape at gaps = 20, 50, and 80 μm and corresponding exposures of 40, 30 and 20 mJ cm^{-2} .

Process latitude for 0.0 μm bias to achieve $0.25 \pm 10\%$ μm

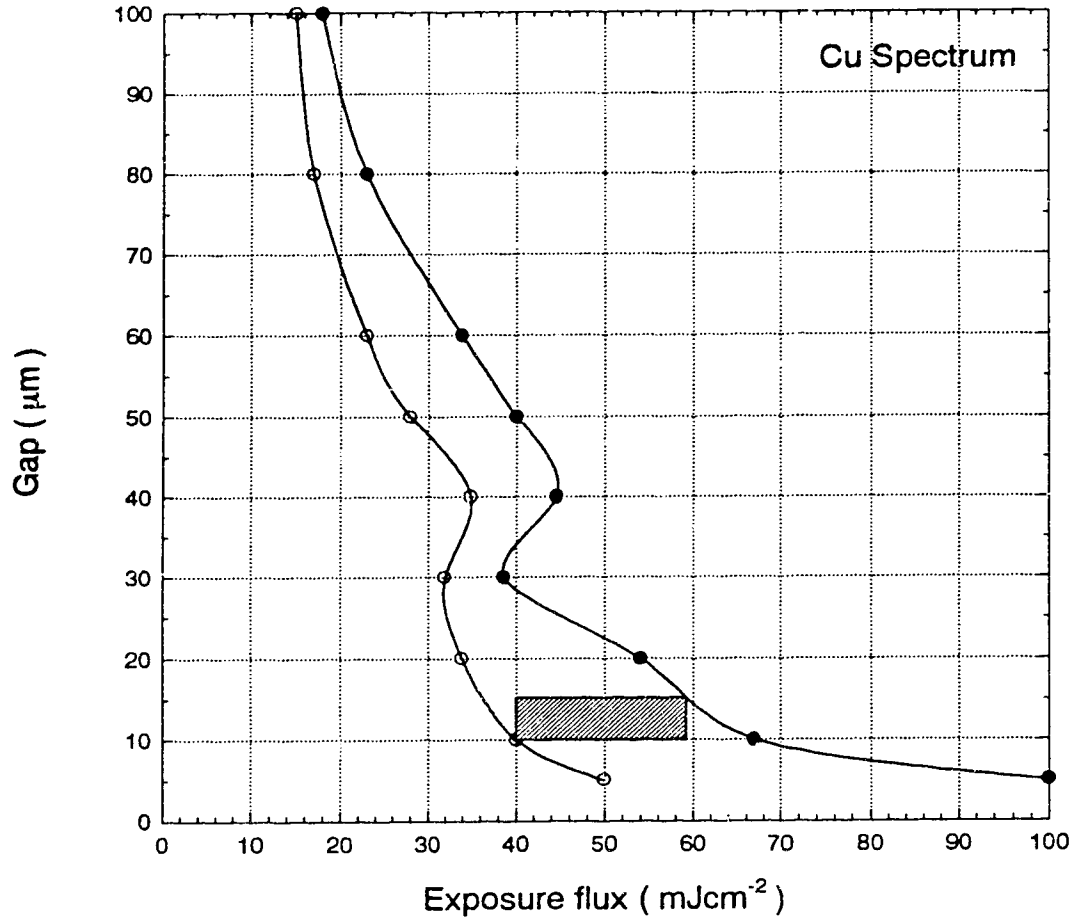


Figure 8.5. (b) Exposure-gap plots of $\pm 10\%$ linewidth contours to indicate allowed operating regimes and process latitude for the printing of $0.25\ \mu\text{m}$ wide lines in XP90104C resist with $0.0\ \mu\text{m}$ bias. Also shown is a potential operating window with an allowed exposure range of $40 - 59\ \text{mJ cm}^{-2}$ and a gap of $10 - 15\ \mu\text{m}$.

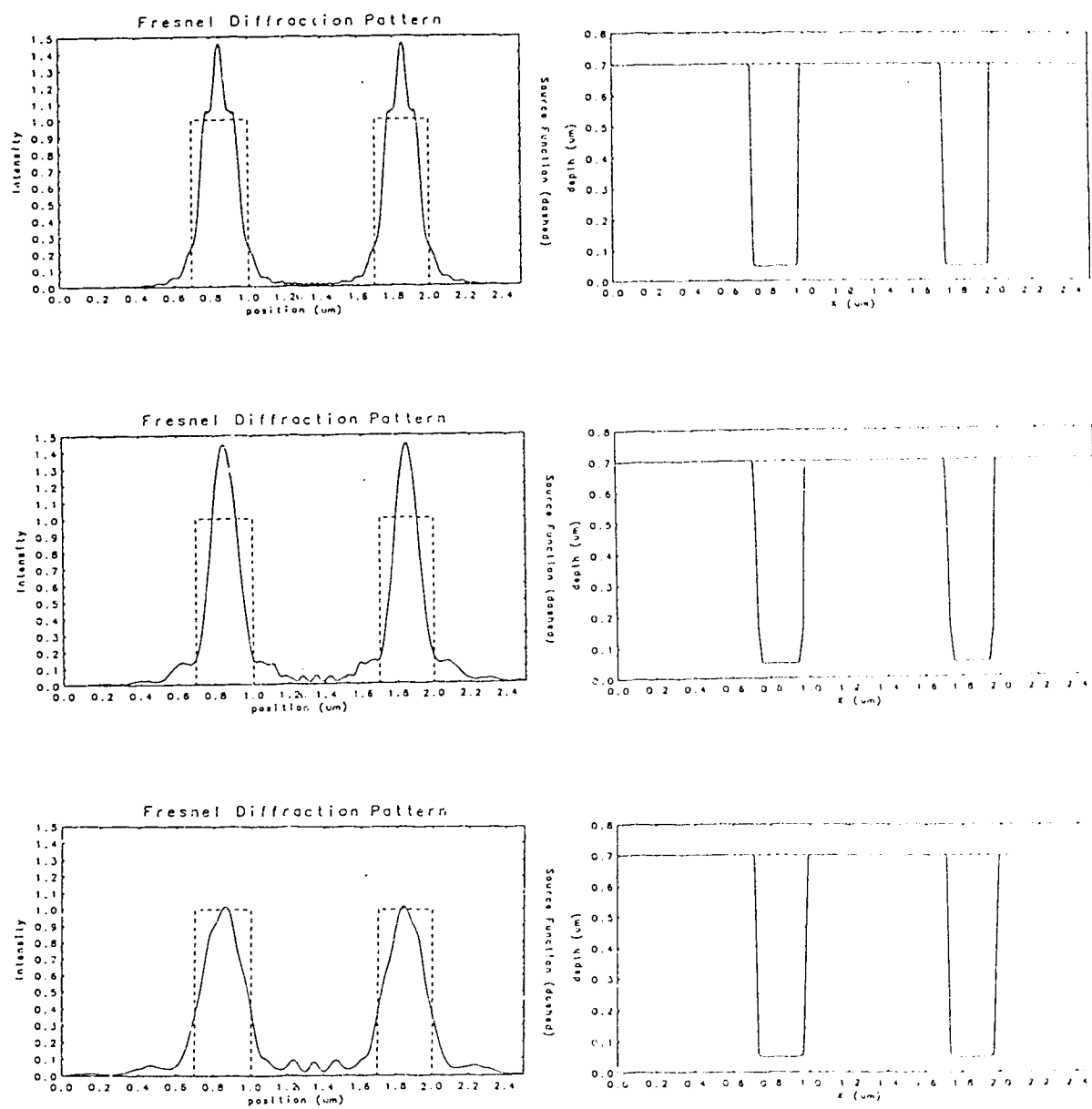


Figure 8.6. (a) Fresnel diffraction pattern and resultant resist lineshape at gaps = 20, 50, and 80 μm and corresponding exposures of 28, 27 and 20 mJ cm^{-2} .

Process latitude for 0.05 μm bias to achieve $0.25 \pm 10\%$ μm

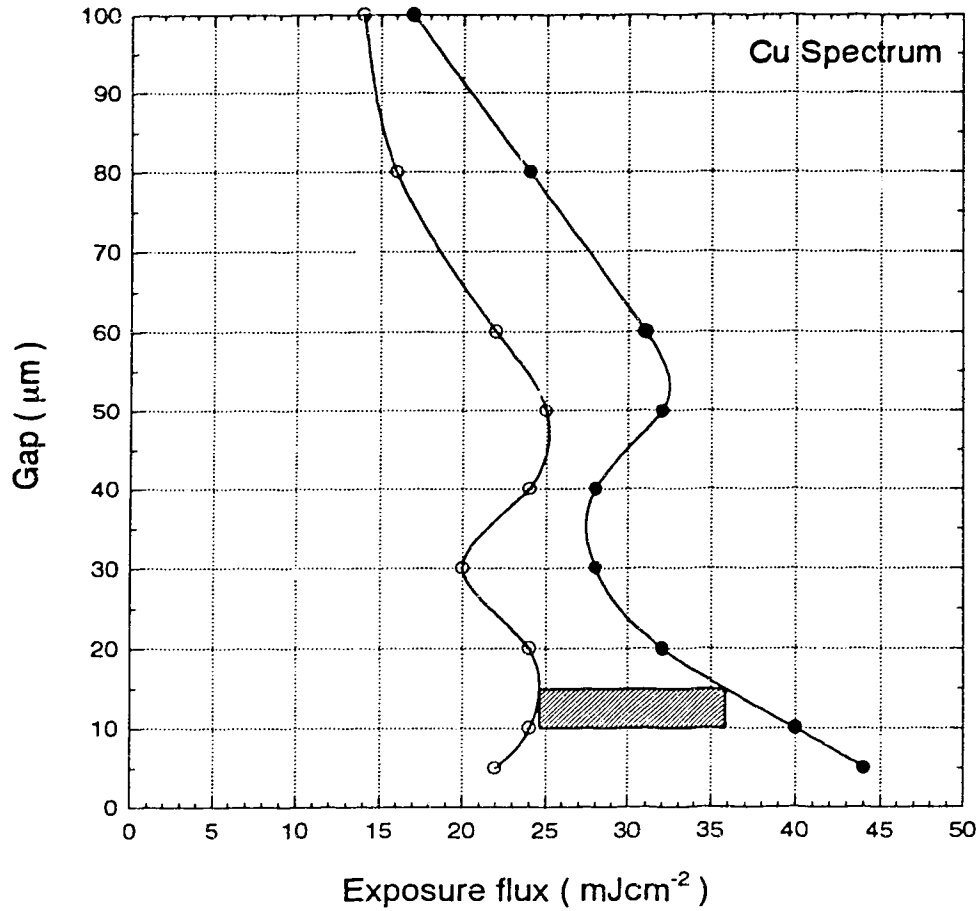


Figure 8.6. (b) Exposure-gap plots of $\pm 10\%$ linewidth contours to indicate allowed operating regimes and process latitude for the printing of $0.25\ \mu\text{m}$ wide lines in XP90104C resist with $0.05\ \mu\text{m}$ bias. Also shown is a potential operating window with an allowed exposure range of $24.5 - 36\ \text{mJ cm}^{-2}$ and a gap of $10 - 15\ \mu\text{m}$.

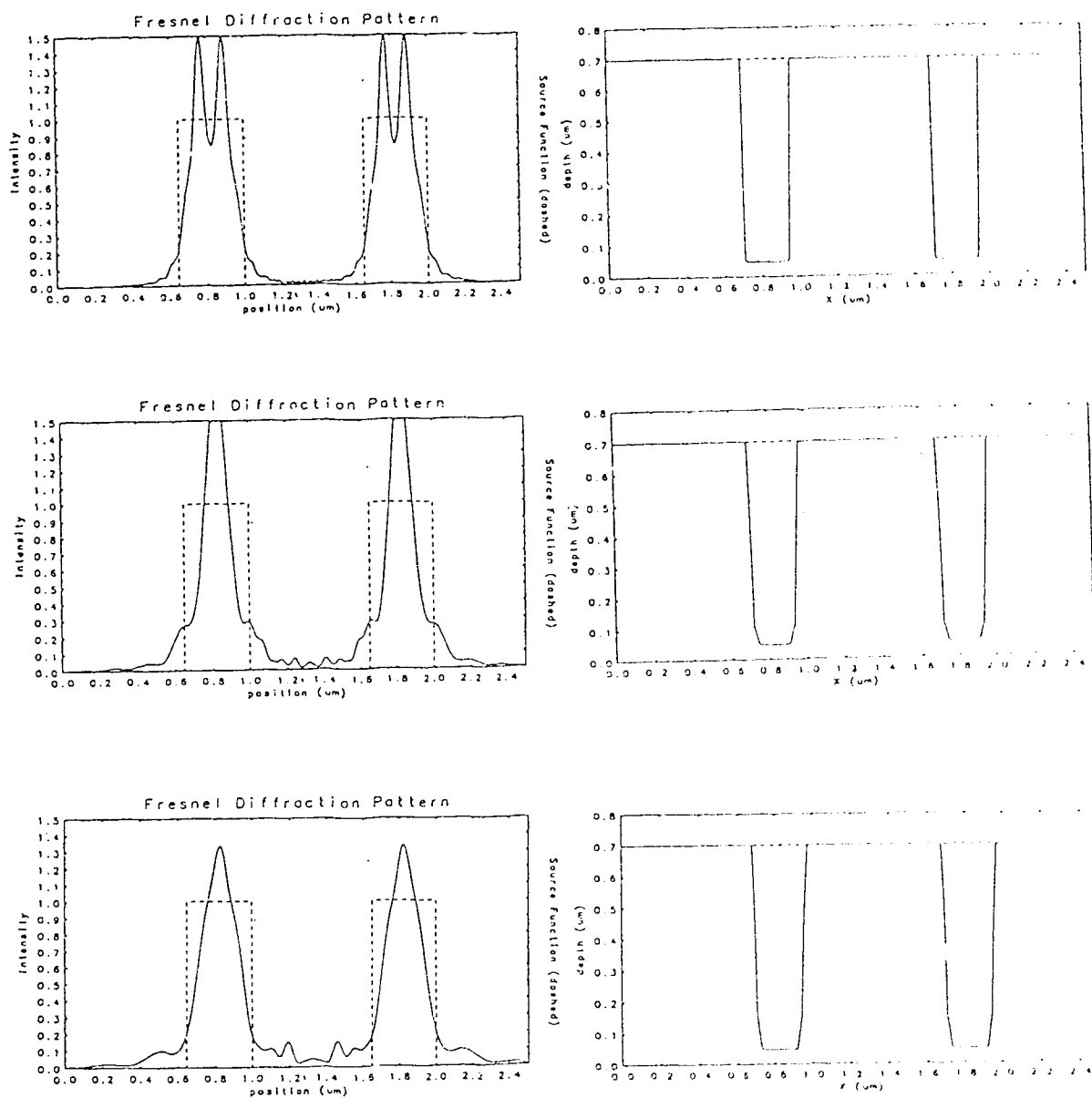


Figure 8.7. (a) Fresnel diffraction pattern and resultant resist lineshape at gaps = 20, 50, and 80 μm and corresponding exposures of 17, 20 and 20 mJ cm⁻².

Process latitude for 0.1 μm bias to achieve $0.25 \pm 10\% \mu\text{m}$

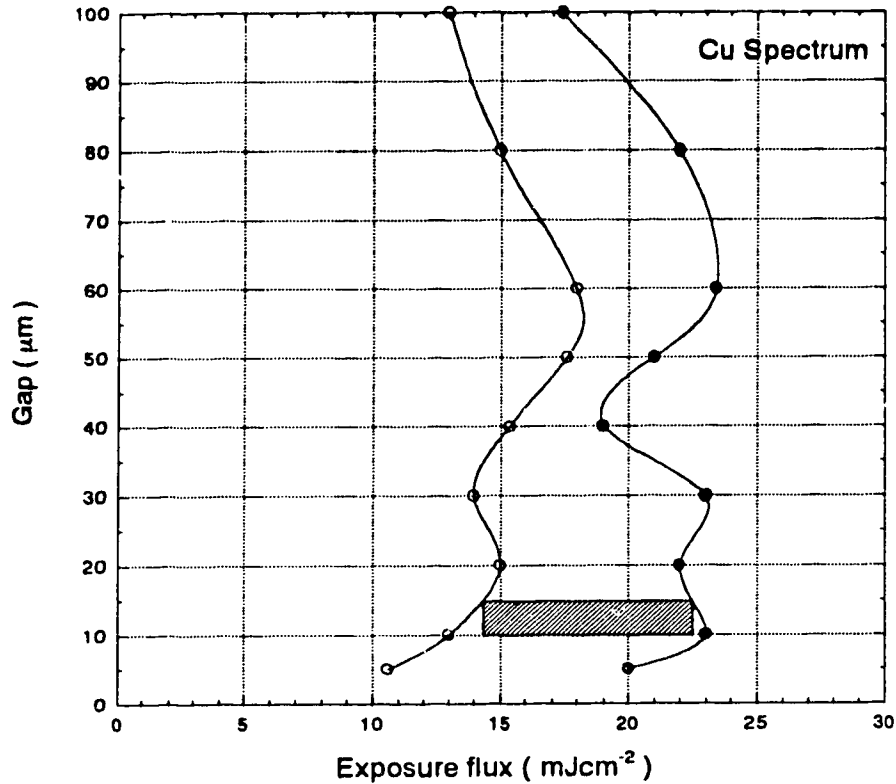


Figure 8.7. (b) Exposure-gap plots of $\pm 10\%$ linewidth contours to indicate allowed operating regimes and process latitude for the printing of $0.25 \mu\text{m}$ wide lines in XP90104C resist with $0.1 \mu\text{m}$ bias. Also shown is a potential operating window with an allowed exposure range of $14 - 22.5 \text{ mJ cm}^{-2}$ and a gap of $10 - 15 \mu\text{m}$.

From Figures 8.5 - 8.7, various operating regions with over $\pm 10\%$ latitude in both exposure and mask to wafer gap can be chosen in order to achieve the desired $0.25 \mu\text{m}$ linewidth. A typical operating region is shown in Figure 8.6 with allowed exposures in the range of 24 to 36 mJ cm^{-2} , an allowed exposure gap of 10 to $15 \mu\text{m}$ and a bias of $0.05 \mu\text{m}$. As the bias is increased the required exposure dose decreases because the contour of the diffraction pattern leading to the exposure is at a higher intensity point on the diffraction pattern.

(ii) 0.1 μm linewidth

The exposure-gap plots with 0.0, 0.01 and 0.02 μm bias to achieve $0.10 \pm 10\%$ linewidth using the laser-plasma source are shown in Figures 8.8 - 8.11.

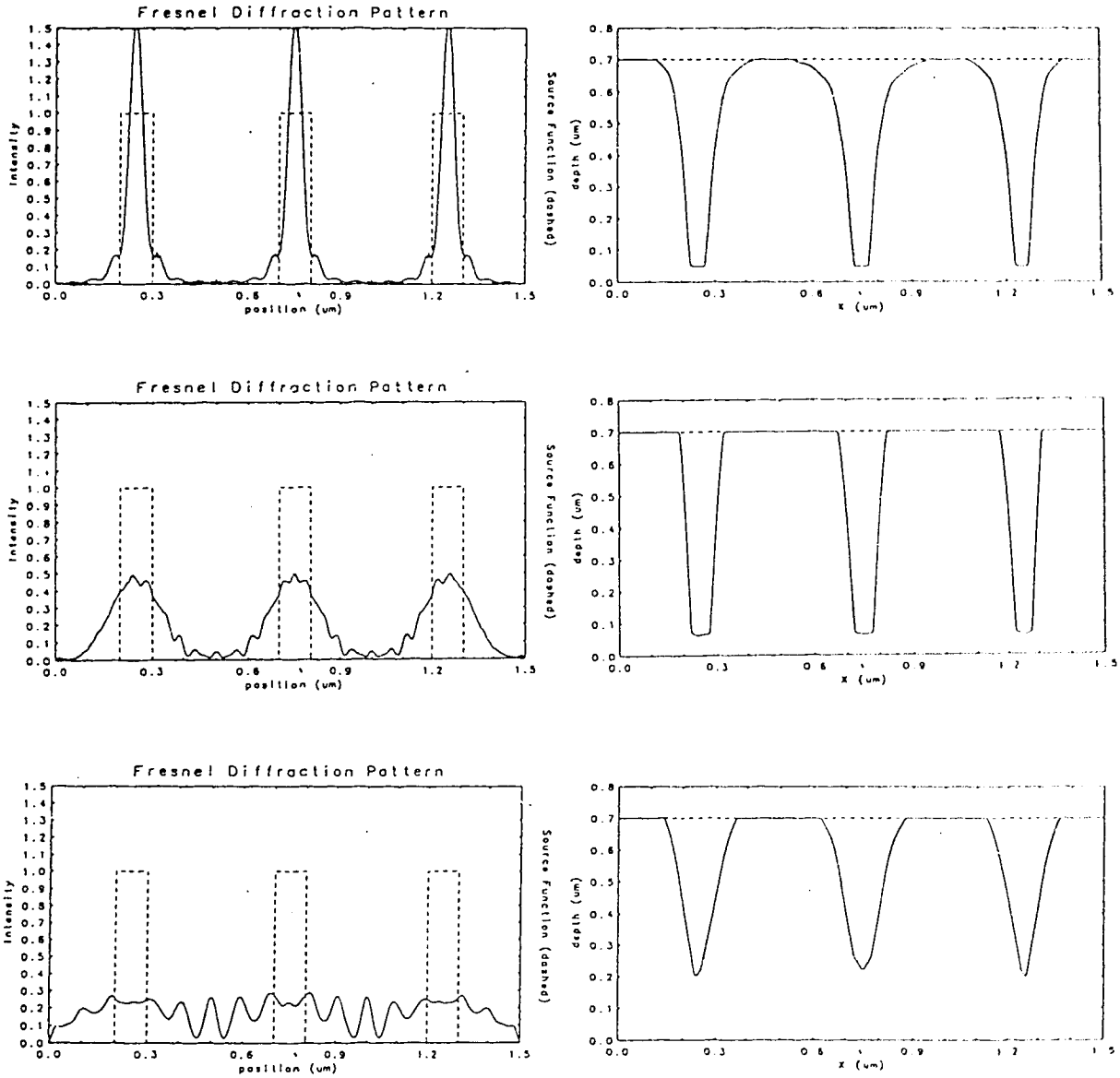


Figure 8.8. (a) Fresnel diffraction pattern and resultant resist lineshape at gaps = 5, 20, and 40 μm and corresponding exposures of 32, 19 and 17 mJ cm^{-2} .

Process latitude for 0.0 μm bias to achieve $0.1 \pm 10\%$ μm

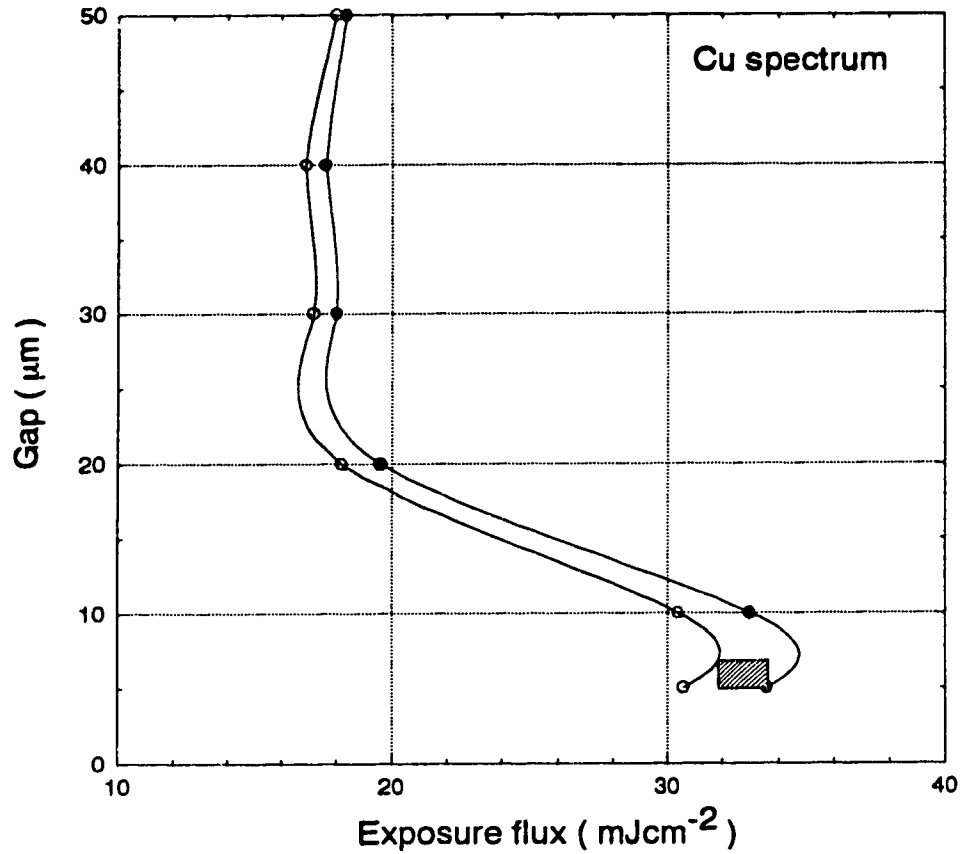


Figure 8.8. (b) Exposure-gap plots of $\pm 10\%$ linewidth contours to indicate allowed operating regimes and process latitude for the printing of $0.1 \mu\text{m}$ wide lines in XP90104C resist with $0.0 \mu\text{m}$ bias. Also shown is a potential operating window with an allowed exposure range of $32 - 34 \text{ mJ cm}^{-2}$ and a gap of $5 - 7 \mu\text{m}$.

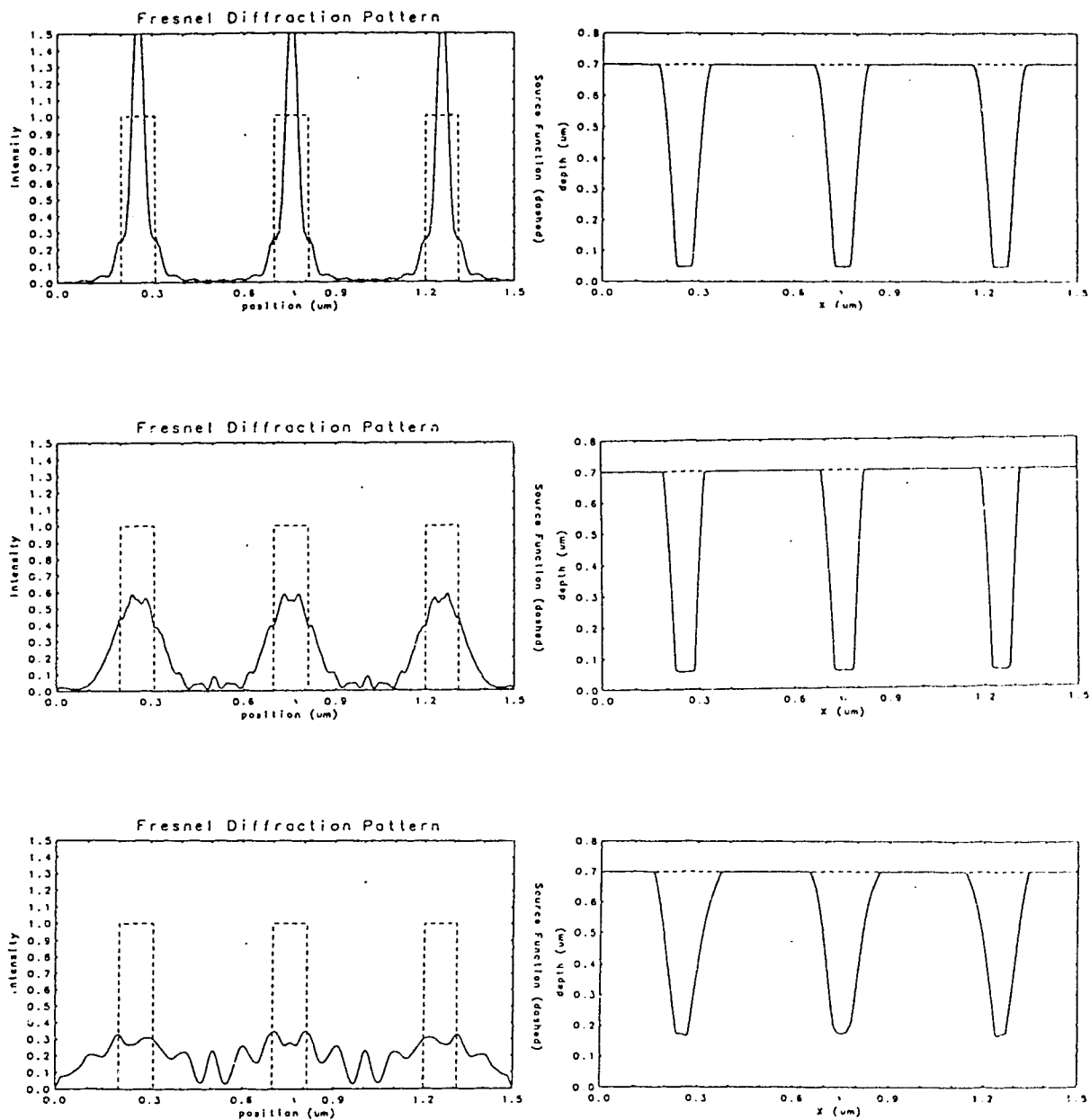


Figure 8.9. (a) Fresnel diffraction pattern and resultant resist lineshape at gaps = 5, 20, and 40 μm and corresponding exposures of 28, 19 and 17 mJ cm^{-2} .

Process latitude for 0.01 μm bias to achieve $0.1 \pm 10\%$ μm

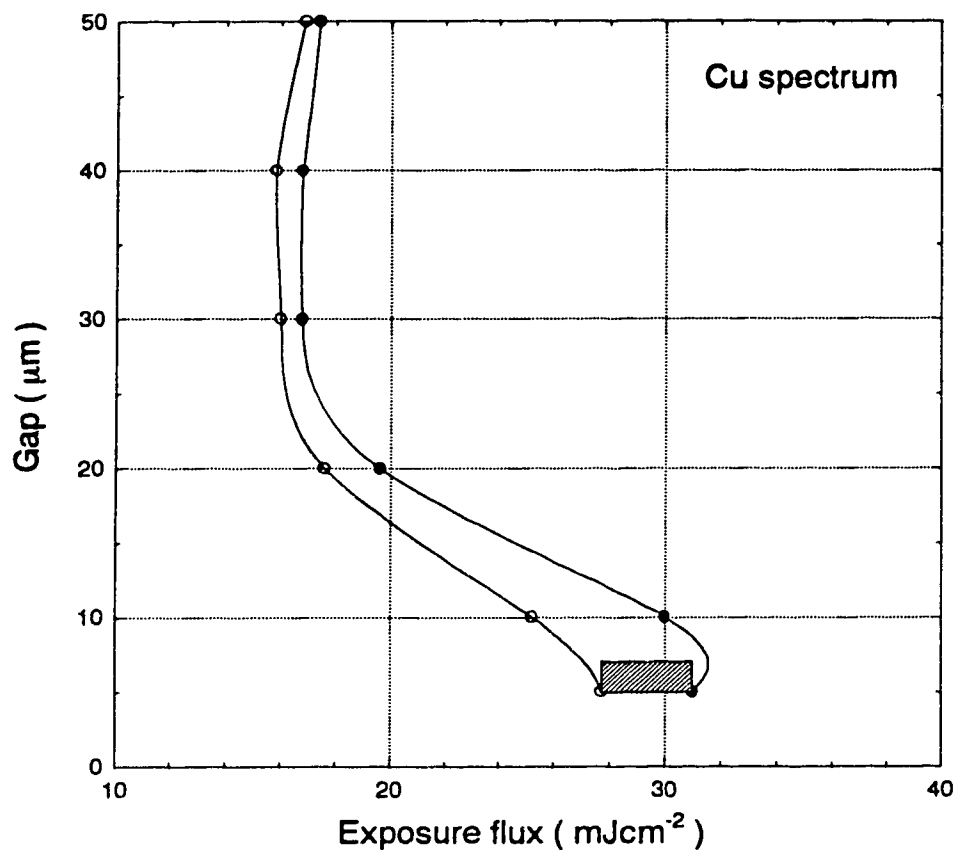


Figure 8.9.(b) Exposure-gap plots of $\pm 10\%$ linewidth contours to indicate allowed operating regimes and process latitude for the printing of 0.1 μm wide lines in XP90104C resist with 0.01 μm bias. A potential operating window with an exposure range of 28 - 31 mJ cm^{-2} and gap range of 5 - 7 μm is shown.

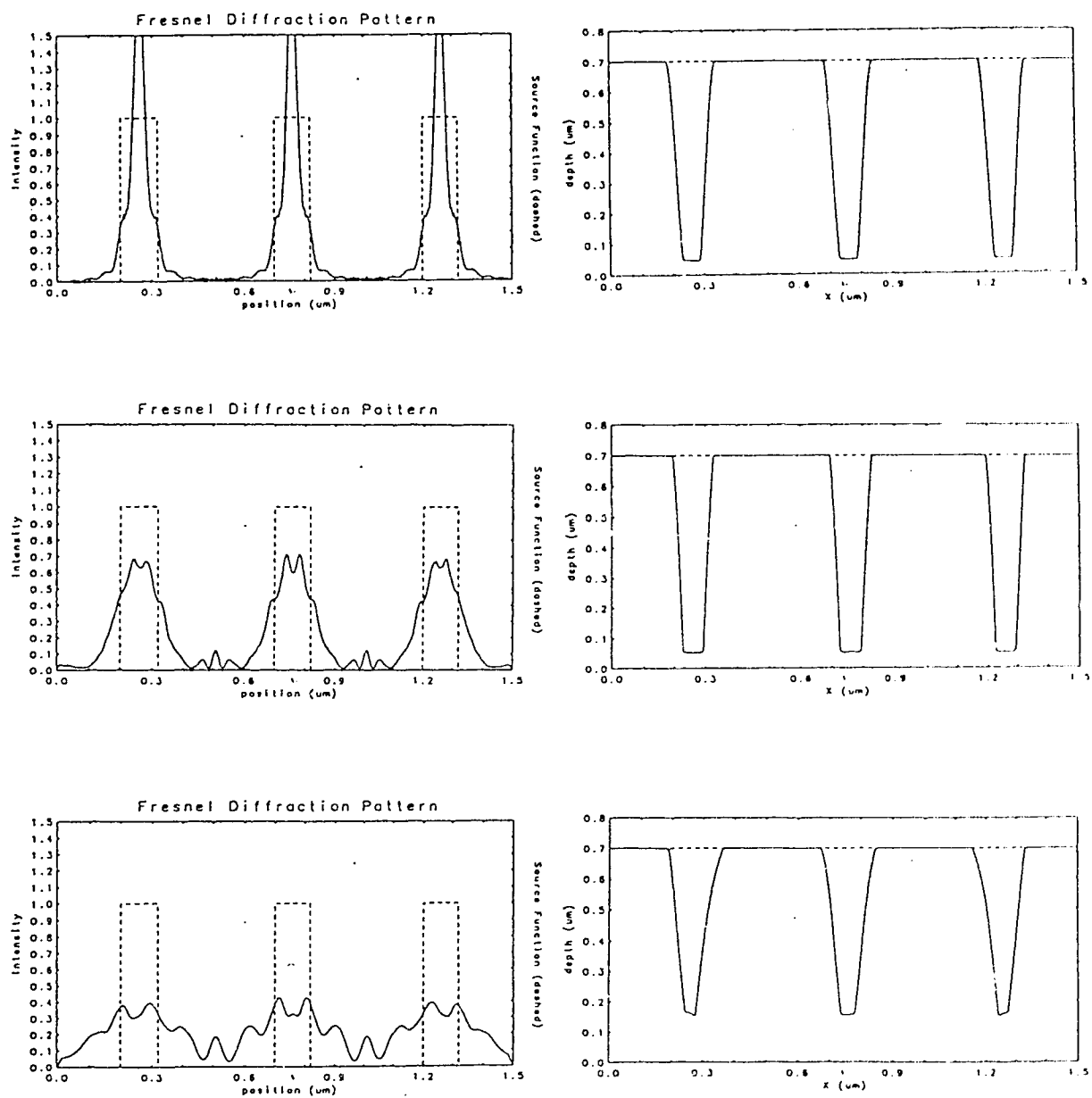


Figure 8.10. (a) Fresnel diffraction pattern and resultant resist lineshape at gaps = 5, 20, and 40 μm and corresponding exposures of 28, 18 and 16 mJ cm^{-2} .

Process latitude for 0.02 μm bias to achieve $0.1 \pm 10\% \mu\text{m}$

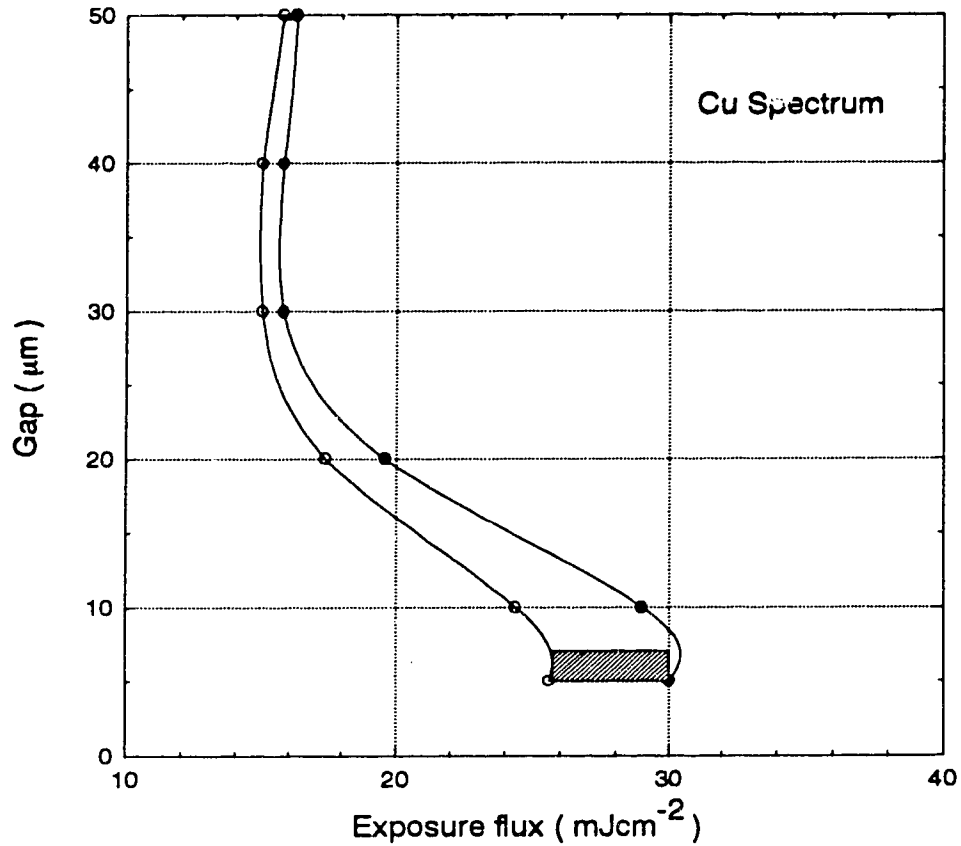


Figure 8.10. (b) Exposure-gap plots of $\pm 10\%$ linewidth contours to indicate allowed operating regimes and process latitude for the printing of $0.1 \mu\text{m}$ wide lines in XP90104C resist with $0.02 \mu\text{m}$ bias. A potential operating window with an exposure range of $26 - 30 \text{ mJ cm}^{-2}$ and gap range of $5 - 7 \mu\text{m}$ is shown.

From Figures 8.8 - 8.10, various operating regions with over $\pm 5\%$ latitude in exposure and $\pm 10\%$ latitude in mask to wafer gap can be chosen in order to achieve the desired $0.1 \mu\text{m}$ linewidth. Such exposure windows are shown in Figures 8.9 and 8.10. As the bias is increased the required exposure dose decreases slightly as explained before. Also, the operating window is significantly smaller than those with $0.25 \mu\text{m}$ linewidth.

8.3.2 Process latitude for a synchrotron x-ray source

The spectrum of a synchrotron source is harder and much broader than that of a laser plasma source. The spectrum used for the present calculation is that of the Aladdin synchrotron in University of Wisconsin as used for a previous study on the XP90104C resist⁽⁷¹⁾. The copper spectrum is centered at about 1150 eV as shown in Figure 6.5(c) whereas the synchrotron spectrum is centered at about 1700 eV. The latter spectrum is shown in Figure 8.11.

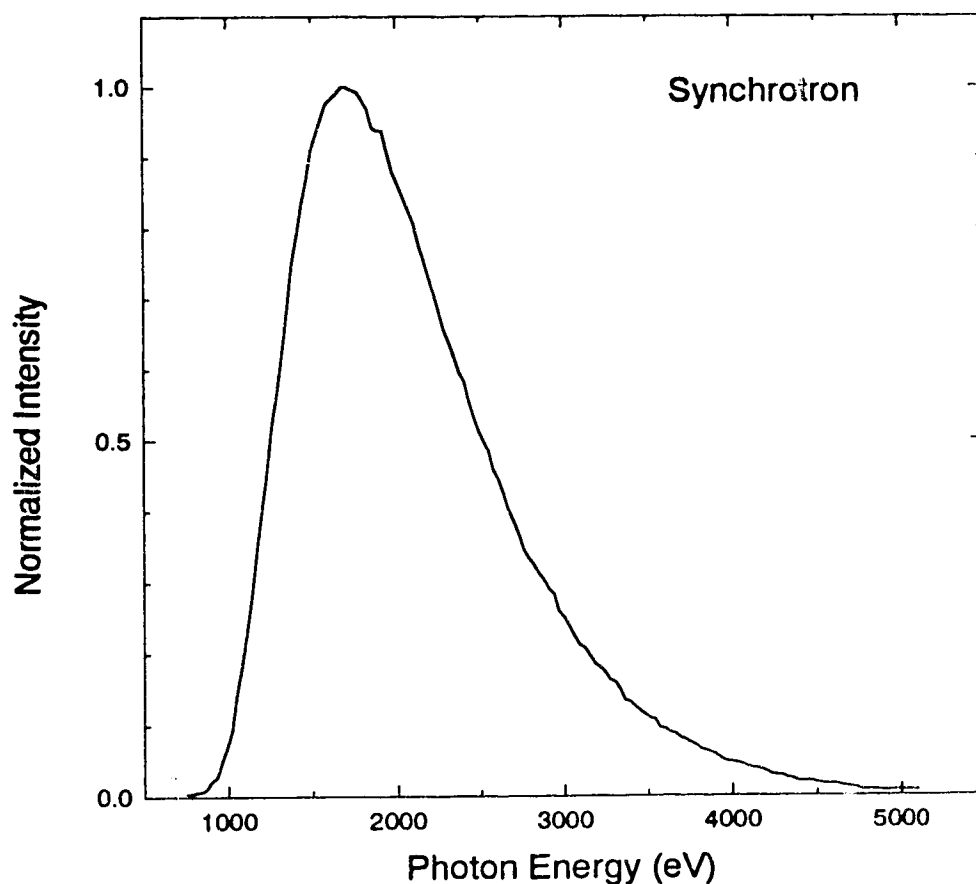


Figure 8.11. Spectrum of keV x-rays from a synchrotron

(i) 0.25 μm linewidth

The exposure-gap plots with 0.0, 0.05 and 0.1 μm bias to achieve $0.25 \pm 10\%$ linewidth using the synchrotron source are shown in Figures 8.12 - 8.14.

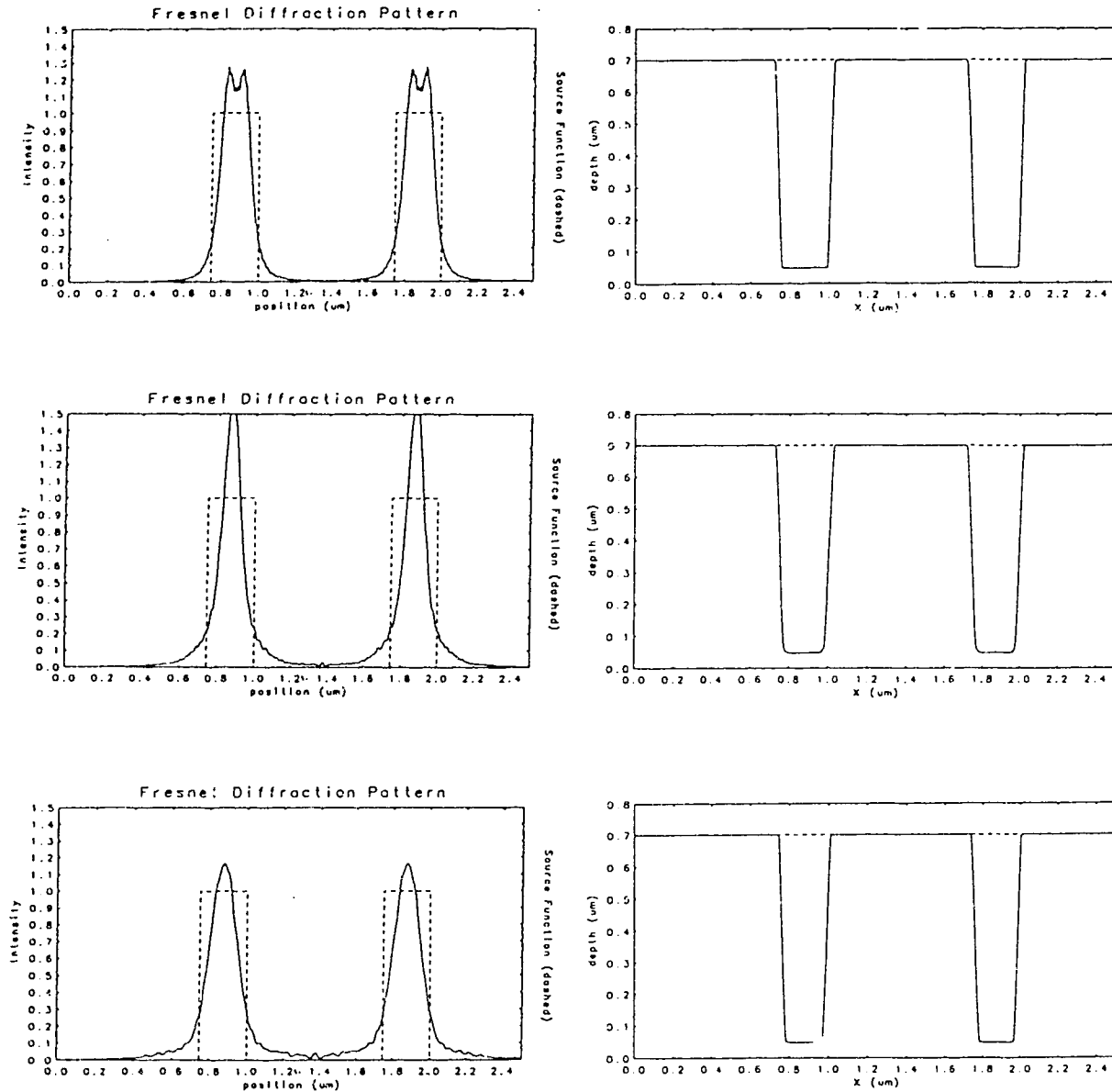


Figure 8.12. (a) Fresnel diffraction pattern and lineshape at gap = 20, 50, and 80 μm and corresponding exposures of 100, 68 and 52 mJ cm^{-2} .

Process latitude for 0.0 μm bias to achieve $0.25 \pm 10\%$ μm

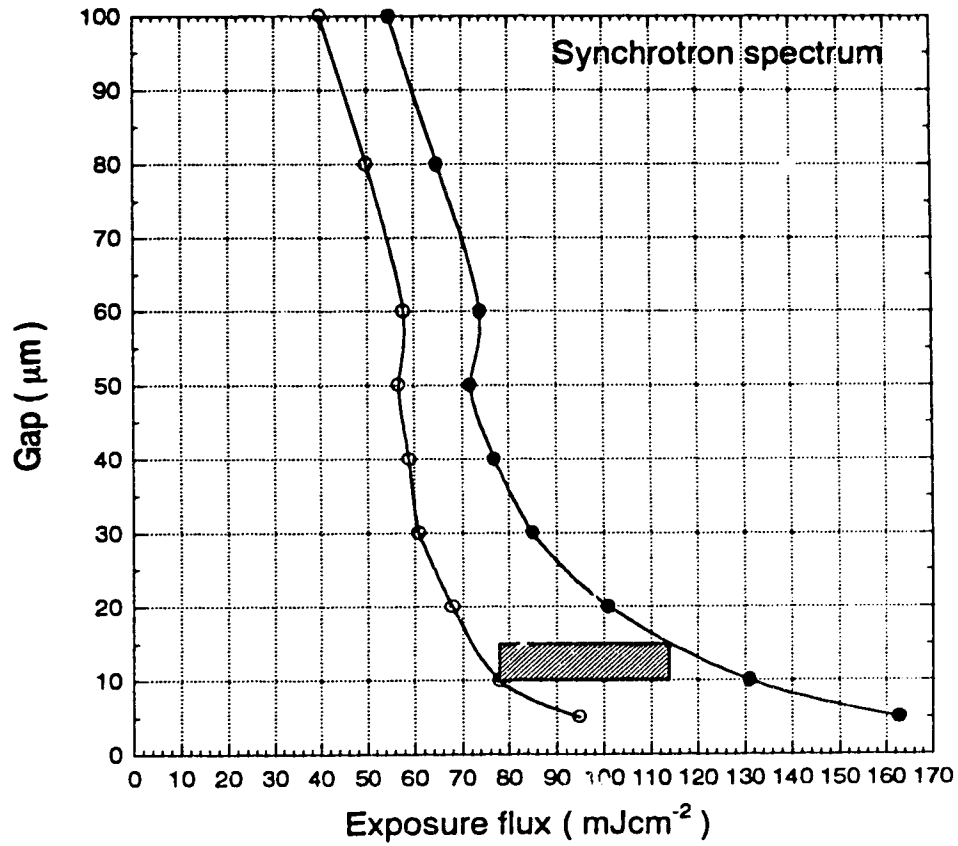


Figure 8.12. (b) Exposure-gap plots of $\pm 10\%$ linewidth contours to indicate allowed operating regimes and process latitude for the printing of $0.25\ \mu\text{m}$ wide lines in XP90104C resist with $0.0\ \mu\text{m}$ bias. A potential operating window with an exposure range of $78 - 114\ \text{mJ cm}^{-2}$ and gap range of $10 - 15\ \mu\text{m}$ is shown.

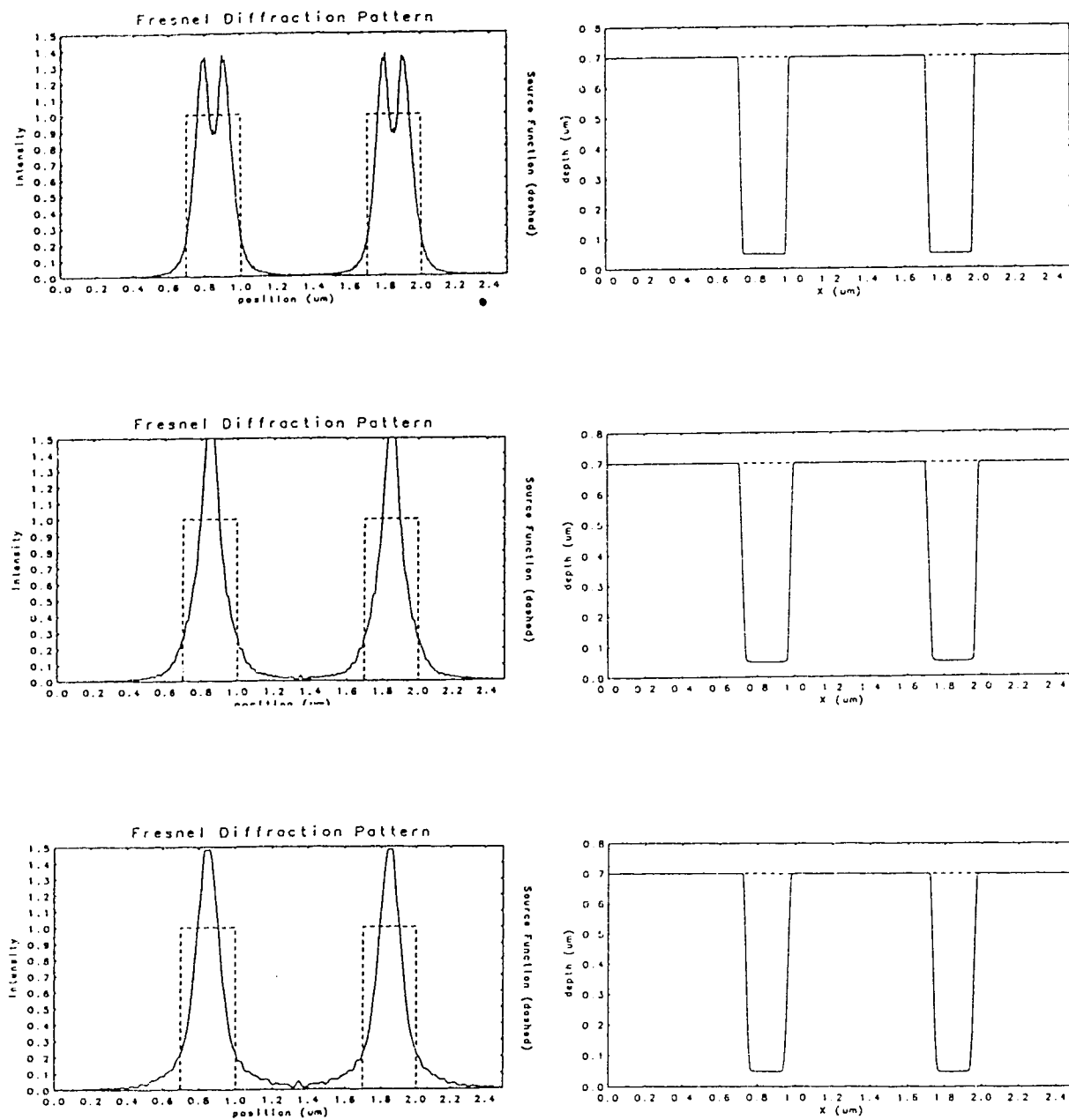


Figure 8.13. (a) Fresnel diffraction pattern and lineshape at gap = 20, 50, and 80 μm and corresponding exposures of 56, 50 and 42 mJ cm^{-2} .

Process latitude for 0.05 μm bias to achieve $0.25 \pm 10\%$ μm

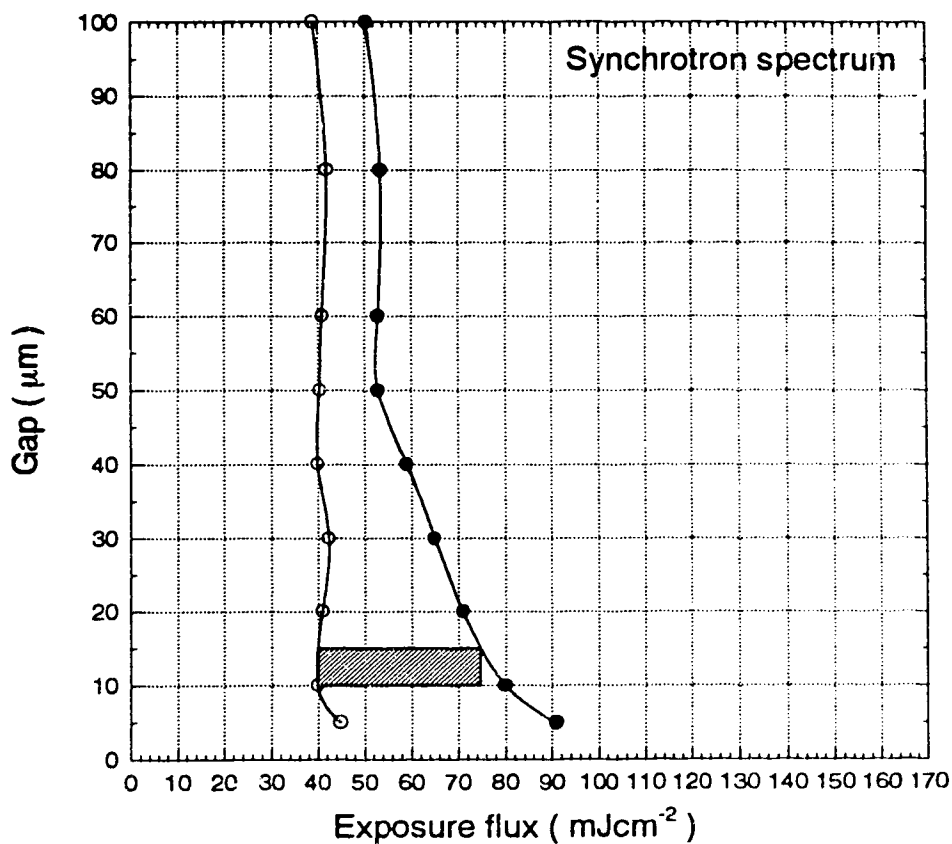


Figure 8.13. (b) Exposure-gap plots of $\pm 10\%$ linewidth contours to indicate allowed operating regimes and process latitude for the printing of $0.25\ \mu\text{m}$ wide lines in XP90104C resist with $0.05\ \mu\text{m}$ bias. A potential operating window with an exposure range of $40 - 74.5\ \text{mJ cm}^{-2}$ and gap range of $10 - 15\ \mu\text{m}$ is shown.

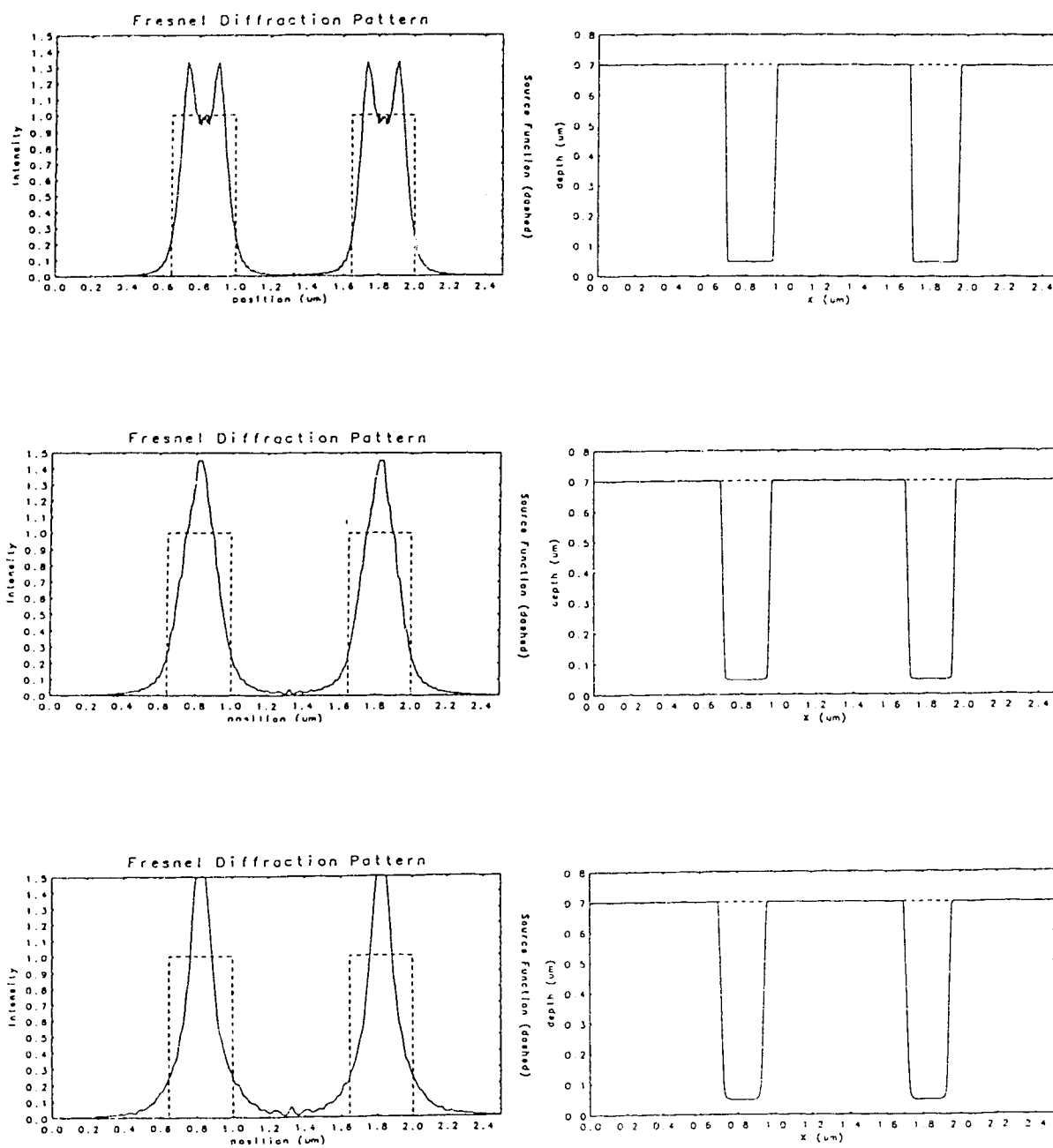


Figure 8.14. (a) Fresnel diffraction pattern and lineshape at gap = 20, 50, and 80 μm and corresponding exposures of 37, 35 and 33 mJ cm^{-2} .

Process latitude for 0.10 μm bias to achieve $0.25 \pm 10\% \mu\text{m}$

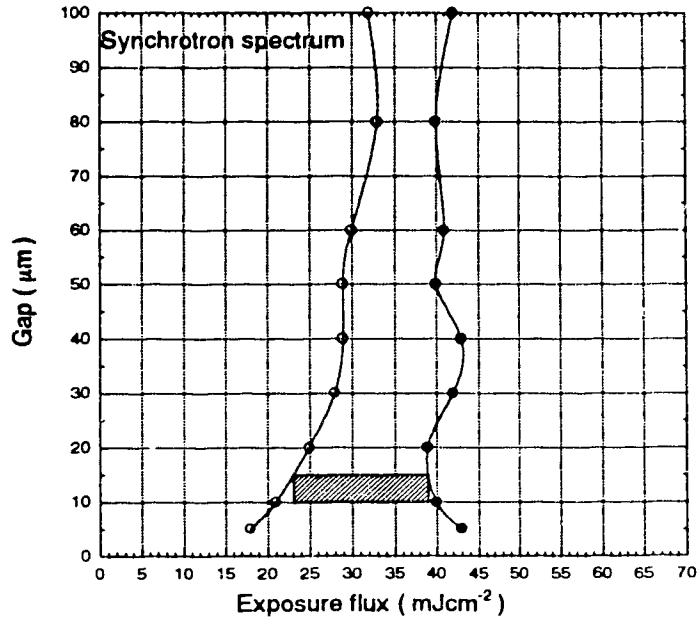


Figure 8.14. (b) Exposure-gap plots of $\pm 10\%$ linewidth contours to indicate allowed operating regimes and process latitude for the printing of $0.25 \mu\text{m}$ wide lines in XP90104C resist with $0.10 \mu\text{m}$ bias. A potential operating window with an exposure range of $23 - 39 \text{ mJ cm}^{-2}$ and gap range of $10 - 15 \mu\text{m}$ is shown.

Comparing Figures 8.5 - 8.7 with Figures 8.12 - 8.14, the general trend of the exposure-gap diagram produced by laser-plasma source and synchrotron source to achieve the $0.25 \mu\text{m}$ linewidth are the same. That is, the required exposure dose decreases and the range of the exposure flux becomes smaller as the bias is increased. However, the boundaries defining the incident flux are more vertical for the synchrotron source. It implies that the exposure flux is less affected by the mask to wafer gap. This is because the synchrotron spectrum is broader and has a larger average photon energy than that of the laser produced copper plasma spectrum. This broad synchrotron spectrum smooths out the bumps in the diffraction profile giving less variation as the Fresnel number is increased.

Comparing to the previous process latitude measurements on XP90104C using a $0.2 \mu\text{m}$ line/ $0.4 \mu\text{m}$ space pattern by Babcock⁽⁷¹⁾, the exposure latitude was found to be

40 to 55 mJ cm^{-2} which is consistent with our simulated exposure-gap plot for printing 0.25 μm lines using 0.0 μm bias.

(ii) 0.1 μm linewidth

The exposure-gap plots with 0.0, 0.01 and 0.02 μm bias to achieve $0.10 \pm 10\%$ linewidth using the synchrotron source are shown in Figures 8.15 - 8.17.

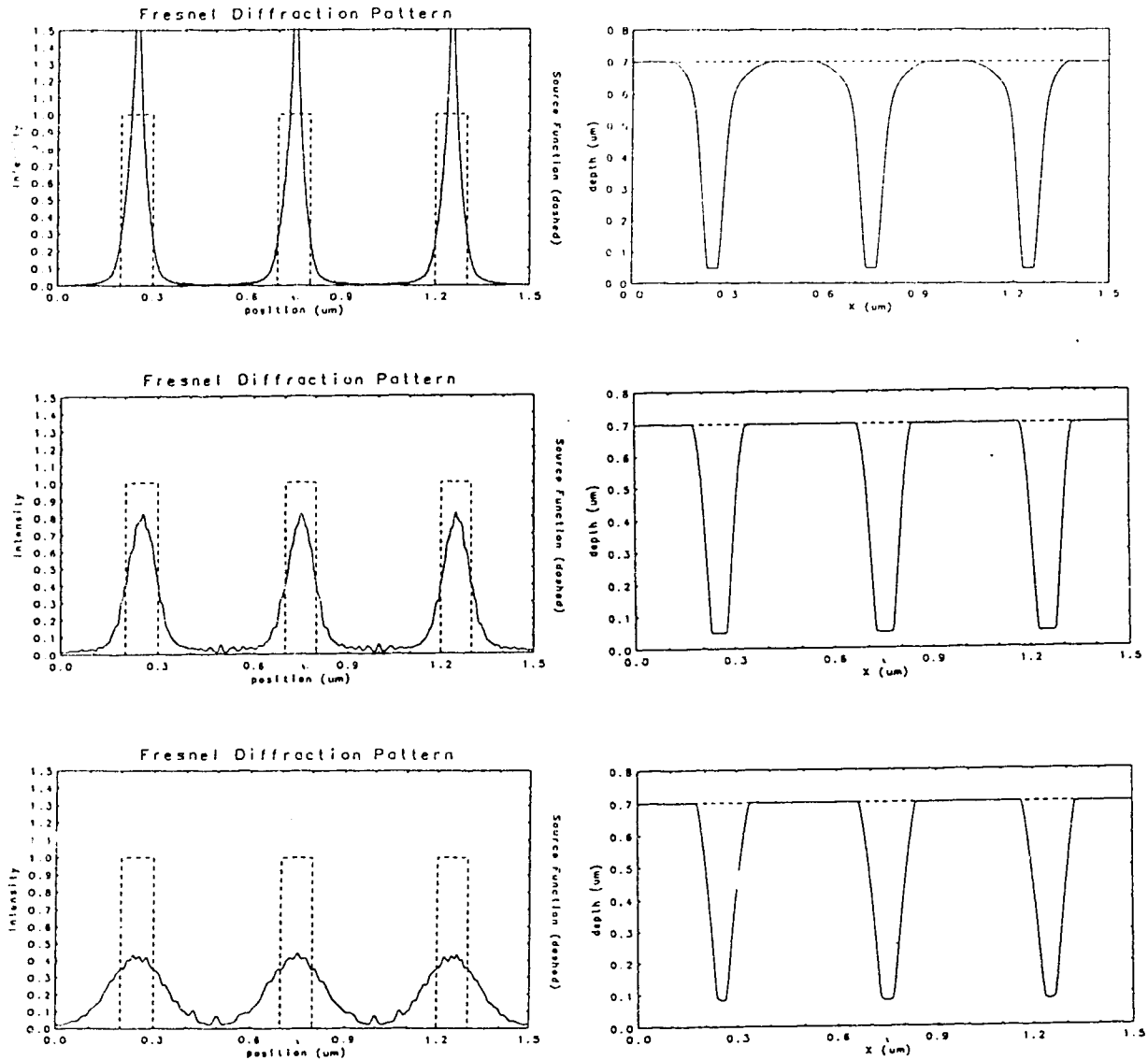


Figure 8.15. (a) Fresnel diffraction pattern and lineshape at gap = 5, 20 and 40 μm and corresponding exposures of 60, 46 and 35 mJ cm^{-2} .

Process latitude for 0.0 μm bias to achieve $0.1 \pm 10\%$ μm

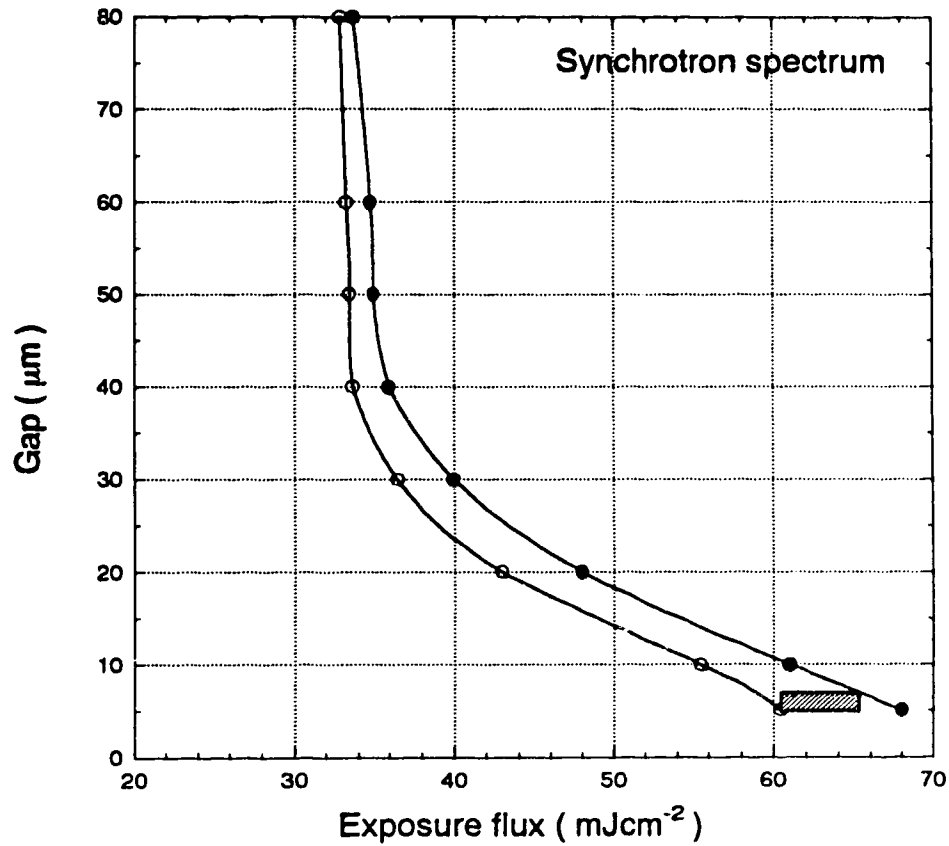


Figure 8.15. (b) Exposure-gap plots of $\pm 10\%$ linewidth contours to indicate allowed operating regimes and process latitude for the printing of $0.10\ \mu\text{m}$ wide lines in XP90104C resist with $0.0\ \mu\text{m}$ bias. A potential operating window with an exposure range of $60.5 - 65.5\ \text{mJ cm}^{-2}$ and gap range of $5 - 7\ \mu\text{m}$ is shown.

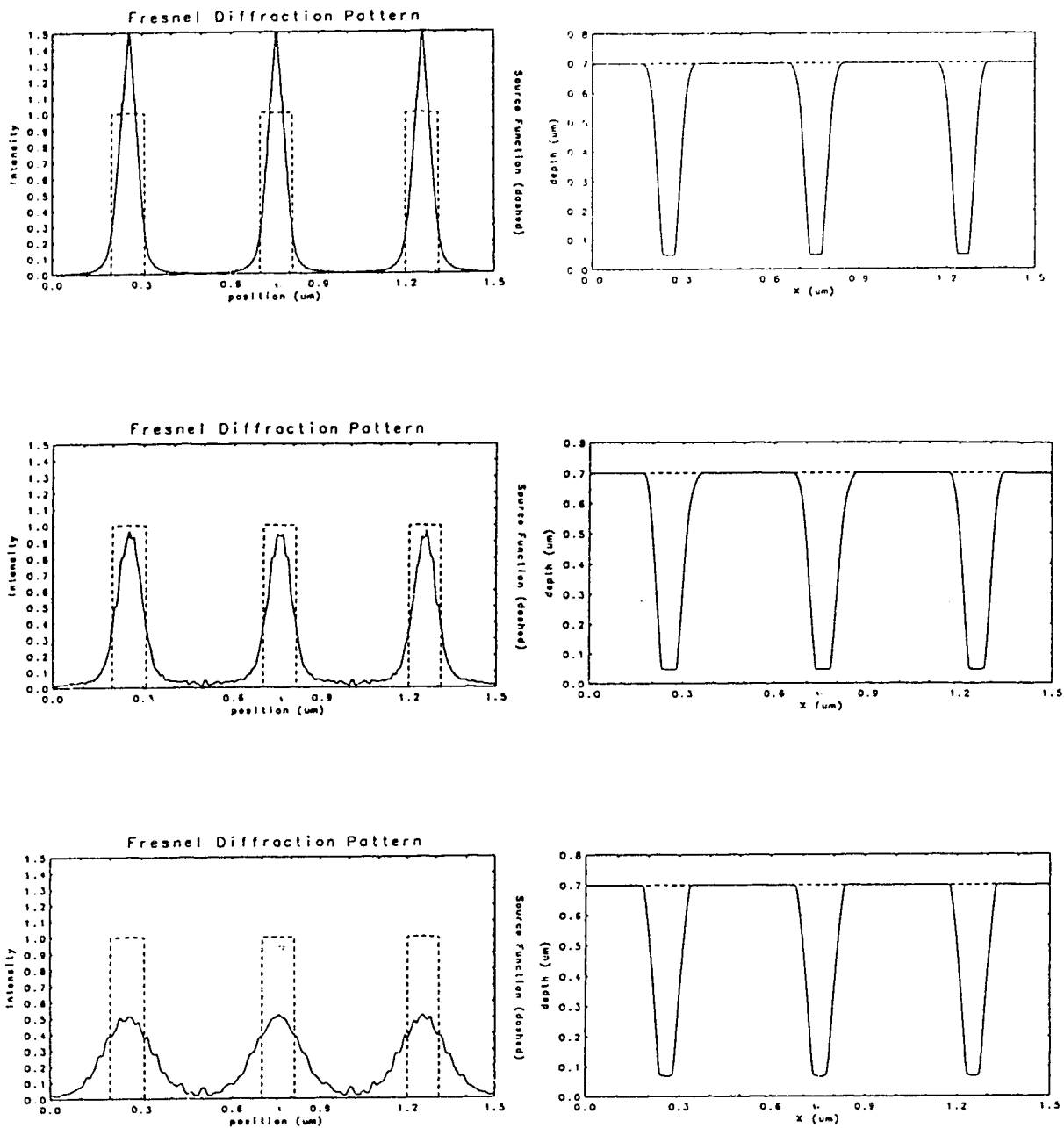


Figure 8.16. (c) Fresnel diffraction pattern and lineshape at gap = 5, 20 and 40 μm and corresponding exposures of 56, 46 and 35 mJ cm^{-2} .

Process latitude for 0.01 μm bias to achieve $0.1 \pm 10\% \mu\text{m}$

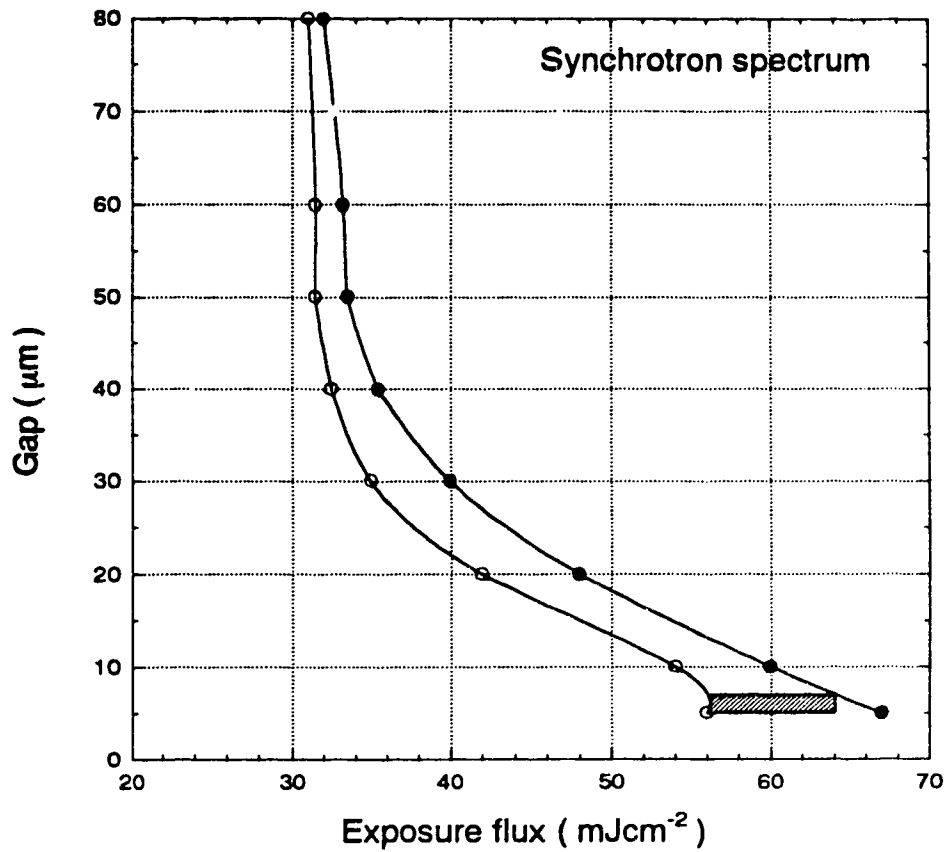


Figure 8.16. (b) Exposure-gap plots of $\pm 10\%$ linewidth contours to indicate allowed operating regimes and process latitude for the printing of $0.10 \mu\text{m}$ wide lines in XP90104C resist with $0.01 \mu\text{m}$ bias. A potential operating window with an exposure range of $56 - 64 \text{ mJ cm}^{-2}$ and gap range of $5 - 7 \mu\text{m}$ is shown.

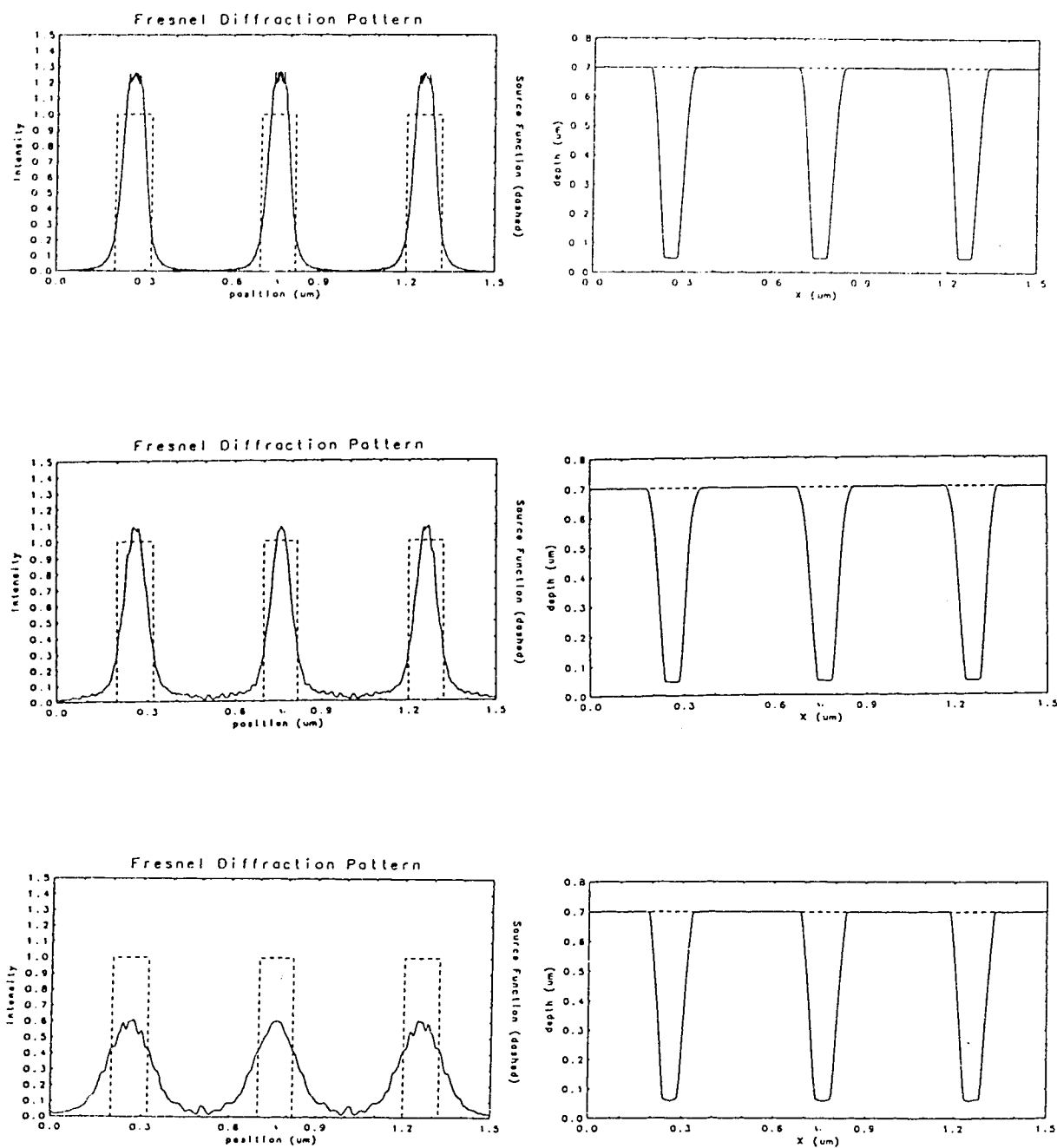


Figure 8.17. (a) Fresnel diffraction pattern and lineshape at gap = 5, 20 and 40 μm and corresponding exposures of 53, 44 and 33 mJ cm^{-2} .

Process latitude for 0.02 μm bias to achieve $0.1 \pm 10\%$ μm

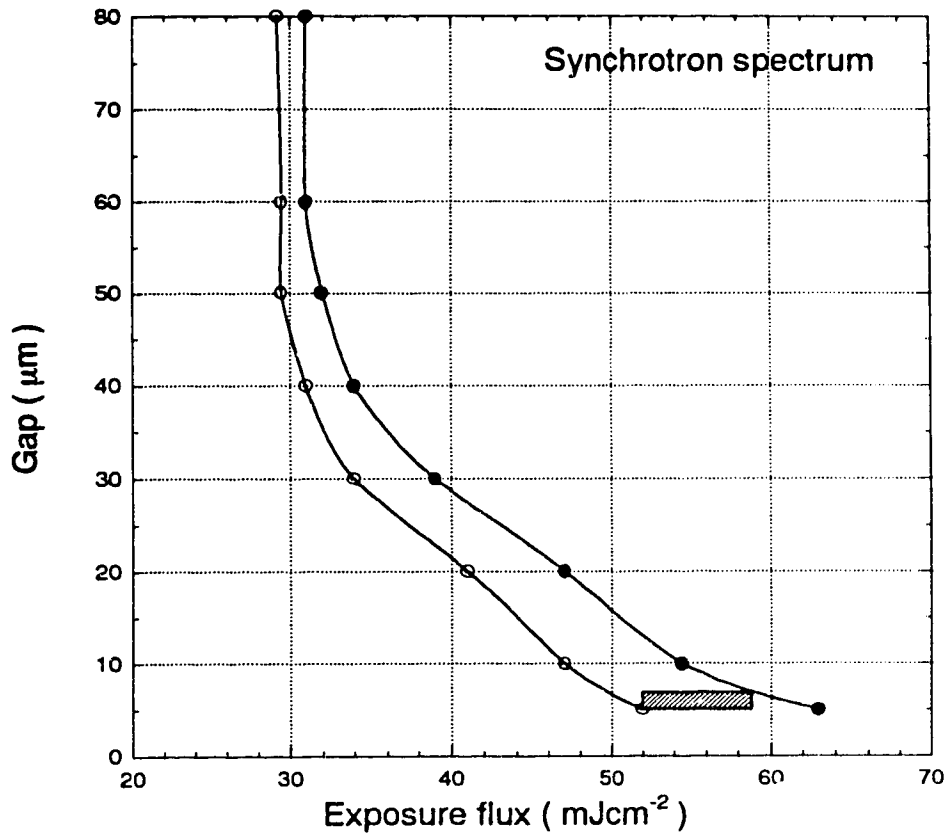


Figure 8.17. (b) Exposure-gap plots of $\pm 10\%$ linewidth contours to indicate allowed operating regimes and process latitude for the printing of $0.10\ \mu\text{m}$ wide lines in XP90104C resist with $0.02\ \mu\text{m}$ bias. A potential operating window with an exposure range of $52 - 59\ \text{mJ cm}^{-2}$ and gap range of $5 - 7\ \mu\text{m}$ is shown.

From Figures 8.15 - 8.17, it can be seen that the required exposure dose decreases as the bias is increased. The incident fluxes required to print the lineshape are larger than that of the laser-plasma source. Also, the operating window is smaller compared to the $0.25\ \mu\text{m}$ linewidth.

8.3.3 Discussion of the process latitude ranges

The process latitude for exposure and mask to wafer gap for producing 0.25 and 0.1 μm linewidth using laser plasma and synchrotron sources with different biases are summarized in table 8.1.

| Linewidth (μm) | Bias (μm) | Thickness of gold mask (μm) | | Exposure (mJ cm^{-2}) | | Gap (μm) |
|--------------------------------|---------------------------|------------------------------------------|-------------|----------------------------------|----------------|--------------------------|
| | | Laser-plasma | Synchrotron | Laser-plasma | Synchrotron | |
| 0.25 | 0.00 | 0.7 | 1.25 | 49.5 ± 9.5 | 96 ± 18 | 12.5 ± 2.5 |
| 0.25 | 0.05 | 0.7 | 1.25 | 30 ± 6 | 57 ± 17 | 12.5 ± 2.5 |
| 0.25 | 0.10 | 0.7 | 1.25 | 18 ± 4 | 31 ± 8 | 12.5 ± 2.5 |
| 0.10 | 0.00 | 0.4 | 0.8 | 33 ± 1 | 63 ± 2.5 | 6.0 ± 1.0 |
| 0.10 | 0.01 | 0.4 | 0.8 | 29.5 ± 1.5 | 60 ± 4 | 6.0 ± 1.0 |
| 0.10 | 0.02 | 0.4 | 0.8 | 28 ± 2 | 55.5 ± 3.5 | 6.0 ± 1.0 |

Table 8.1. Exposure and Gap Latitude in printing 0.25 and 0.1 μm lines using laser-plasma and synchrotron source with different biases.

Since the synchrotron spectrum is harder than the laser produced plasma spectrum, the thickness of the mask used in the simulation is thicker for the synchrotron case than the laser plasma case. It can be seen from Table 8.1 that, in general, as the bias increases the nominal exposure dose decreases whereas the relative exposure latitude increases. There is a clear advantage in using the technique of biasing to reduce the exposure dose and enlarge the exposure tolerance. The laser plasma x-ray source requires about half of the exposure dose than the synchrotron x-ray source in printing a particular linewidth for the same bias. This means the resist is two times more sensitive to the laser produced copper plasma spectrum than the synchrotron spectrum. This is mainly due to the strong dependence of x-ray absorption with x-ray energy as discussed in section 7.5. The exposure latitude for laser plasma and synchrotron sources is around 20 % depending on the bias in printing the 0.25 μm linewidth for the same gap of $12.5 \pm 2.5 \mu\text{m}$. However, the exposure latitude in both cases is about 5 % in printing the 0.1 μm linewidth for the gap of $6 \pm 1 \mu\text{m}$. The exposure window is smaller as the linewidth becomes narrower. The exposure and gap must be well controlled for 0.1 μm feature sizes.

8.4 Alignment Techniques

There are a number of techniques being developed to achieve high accuracy alignment within 20 % of the linewidth. The first technique used by Karl Suss⁽⁷⁵⁾ and others^(76, 77) is by using standard optical microscopes to sight marks on the wafer and the mask. A second technique employed at the Aladdin synchrotron uses diffraction from alignment grating bar patterns on the wafer through linear Fresnel lens on the mask to achieve alignment^(78, 79). The next more complicated techniques employ interference between beams diffracted from grating patterns on both the mask and the wafer⁽⁸⁰⁾. Other more speculative alignment techniques have also been suggested such as using x-ray imaging itself or through the use of micro-machined microscopic silicon e-beam columns mounted right on the mask⁽⁸¹⁾.

Overall, the present alignment techniques are adequate for the production of 0.2 μm linewidths and with further improvements should allow the alignment down to 0.1 μm linewidths.

8.5 Throughput calculation of the laser-plasma x-ray source

One of the most important parameters for any future industrial scale x-ray lithography system is the net throughput in wafer-layers per hour which can be processed. The time required to expose an 8" wafer is calculated to demonstrate the effectiveness of using a laser-plasma as the x-ray source in lithography. A number of factors are important in such a calculation: the x-ray emission power, the size of each exposure field, the distance from the source to the wafer, the attenuation of mask substrate and filters, and the required exposure of the resist. Typically, an exposure field of 20 mm \times 20 mm is envisaged for future ULSI circuits. To minimize geometric shadowing effects at the edge of field of view as shown in Figure 2.4 and to give a reasonable stopping distance for debris in the helium background gas a minimum source to wafer distance is around 10 cm. Transmission for 640 torr of helium at 10 cm is 93 %. Transmissions for the mask substrate of 50 % and aluminized plastic debris shield of 50 % can be used. Assume that a state of the art commercial 200 W KrF laser firing at 100 Hz repetition rate is used with a 2% x-ray conversion efficiency. Thus we start with a point source of keV x-rays with a power of $P_x = 4 \text{ W}$.

The intensity of x-rays in vacuum 10 cm from the point source is

$$I_{xv} = \frac{P_x}{2\pi r^2} = 6.37 \text{ mWcm}^{-2}$$

The real intensity at the surface of the resist is reduced by the transmission factors of the mask substrate, debris filters and background helium gas to give

$$I_{xr} = I_{xv} \times T_M \times T_F \times T_{he} = 1.48 \text{ mW cm}^{-2}$$

From the process window calculations a flux of $F_r = 20 \text{ mJ cm}^{-2}$ is required to expose the resist thus giving an exposure time per field of

$$t_{exp} = \frac{F_r}{I_{xr}} = 135 \text{ s}$$

Assume that 20 cm diameter wafers are being processed with 55 fields per wafer (a 70 % fill density). If the stepper system takes $t_{align} = 2 \text{ s}$ to align each field and $t_{chg} = 20 \text{ s}$ to change wafers the total time to process one wafer layer is:

$$\begin{aligned} t_{WL} &= 55 \times (t_{exp} + t_{align}) + t_{chg} \\ &= 873 \text{ s} \\ &= 14.6 \text{ minutes} \end{aligned}$$

Thus with the above system 4.1 wafer levels can be processed per hour.

The desired throughput required to match present day production speeds is on the order of 10 - 20 wafer levels per hour. To meet this throughput a system 3 to 5 times more powerful than presently could be fabricated with commercial KrF lasers would be required. Such a requirement could be met with more powerful KrF lasers such as 1 kW research excimer lasers being developed in Europe at the present time. Alternatively, the requirement could be met with an improved conversion efficiency of laser light into x-rays of $\eta_x = 6 - 10 \%$. In optimized, single picosecond pulse experiments conversion efficiencies of $\eta_x > 10 \%$ have been demonstrated⁽⁸²⁾. However with high energy pulse trains, extraction conversion efficiencies of only up to the order of 2 % have been achieved to date. It is expected that with further work these conversion efficiencies can be improved towards the optimized value of $\sim 10 \%$.

Overall, while a KrF laser-plasma x-ray source based on current technology will fall short of full scale industrial requirements, such systems are attractive for research and development work. With future improvements in laser technology and conversion efficiencies it is expected that such systems could potentially be competitive for industrial scale production.

8.6 Future Fabrication of $0.1\ \mu\text{m}$ Surface Acoustic Wave Devices

Based on the results of the previous section it appears feasible to reproduce patterns down to $0.1\ \mu\text{m}$ linewidth. A surface acoustic wave (SAW) devices is an example of simple device which can be fabricated with submicron linewidth using x-ray lithography. One of the next stages of the x-ray lithography project will be the fabrication of such devices with linewidth down to $0.1\ \mu\text{m}$. Surface acoustic waves can be generated at the free surface of an elastic solid. The generation of such waves is achieved by application of a voltage to a metal film interdigital transducer (IDT) placed on the surface of a piezoelectric solid. Two IDTs are then required in the basic SAW device configuration sketched in Figure 8.18.

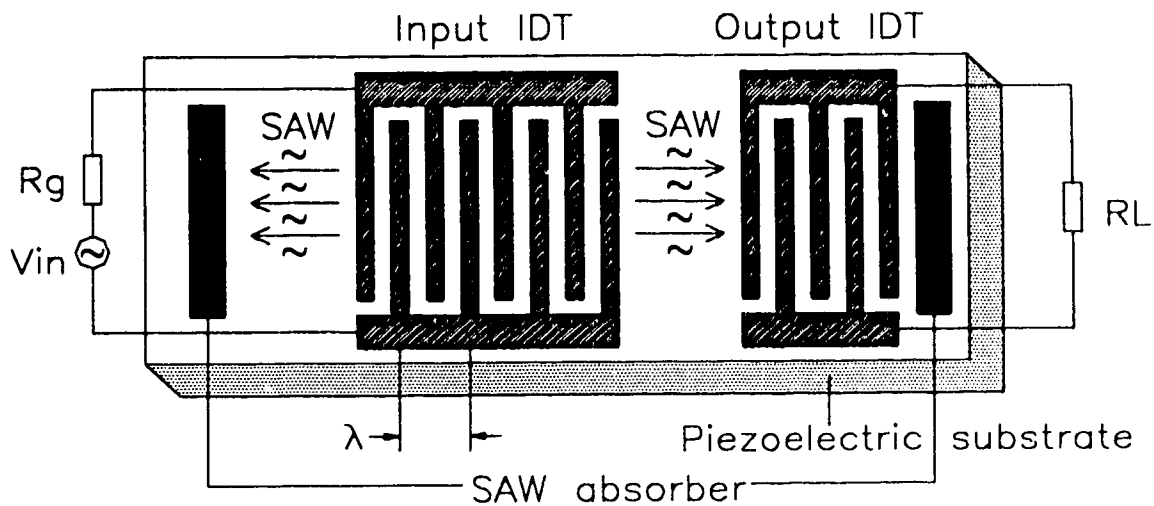


Figure 8.18 : Outline of a basic SAW filter on a piezoelectric substrate⁽⁸³⁾.

One of the IDTs acts as the device input and converts signal voltage variations into mechanical surface acoustic waves. The other IDT is employed as an output receiver to convert mechanical SAW vibrations back into output voltages. Wax absorbers are often used in such designs to suppress spurious SAW transmissions due to the bidirectionality of the IDTs. Because the generation and detection of the acoustic waves depends on the coherent addition from many sequential electrodes the peak response is obtained when the wavelength of the acoustic wave exactly matches the transducer period. Thus maximum response is obtained in a narrow range around this center frequency.

SAW-based devices and systems have several excellent features when compared to competing narrow band filter technologies. Some of these are:

1. SAW devices can have outstanding reproducibility in performance, from device to device.
2. SAW devices can be mass produced using semiconductor microfabrication techniques and thus they can be cost competitive in mass-volume applications.
3. SAW devices can generally be designed to provide quite complex signal processing functions within a single package containing a single piezoelectric substrate with superimposed thin-film input and output interdigital transducers.
4. SAW filters can be made to operate very efficiently at high-harmonic modes. As a result, gigahertz frequency devices can be fabricated using relatively inexpensive photolithography⁽⁷⁶⁾.

Due to the above merits of SAW devices, surface acoustic wave filters are extensively applied in today's communication technology. The feature size of the finger structures and the type of the substrate determine the frequency characteristic of the SAW device. A SAW filter with 0.3 μm lines and spaces has been printed on a quartz substrate using ion projection lithography. This narrow band SAW filter has been designed to demonstrate a filter characteristic at 3.5 GHz⁽⁷⁷⁾. However, with the advent of wireless local area networks, cellular phone communications and multigigabit fiber communication rates the communication spectrum is expanding towards 10 GHz and beyond extending the frequency requirements for such devices. By applying x-ray lithography, 0.1 μm linewidths could be achieved and fabrication of 10 GHz SAW filter should be possible.

8.7 Radiation Damage

The radiation flux absorbed by the underlying wafer material is significant and can lead to radiation damage of the underlying circuit structures such as preformed semiconductor junctions and gates. The absorbed dose in sensitive resists is on the order of 50 J cm⁻² which is equivalent to 5 Mrad of radiation exposure. These levels of radiation are known to cause defects in semiconductor materials and lead to some degradation of performance. However, the radiation damage can be repaired to a large extent by post process annealing of the wafer⁽⁸⁵⁾. In addition, the development of higher sensitivity resists has decreased the dose which is required during exposure so that the damage is much less to begin with. The fabrication of 0.35 μm SRAM devices by IBM⁽⁸⁶⁾ has proven that radiation damage is not a limiting factor in the production of microchips.

Chapter 9 : Conclusions

The primary objective of this research project was to characterize and model the process latitude for a high sensitivity x-ray lithography resist using a laser plasma x-ray source. This involved the setup and testing of the x-ray exposure station. The Lumonics 430 XeCl, Lambda Physik FL4000 dye laser and Lumonics 540 KrF laser modules were employed to produce amplified trains of 50 ps KrF laser pulses at a rate of 20 Hz giving a laser output power of up to 6 W. The x-rays are generated by plasma produced by focusing the laser onto a copper tape target. The target chamber is flushed with helium to remove debris and x-ray flux is monitored by a PIN diode which is recorded on a computer.

To carry out this study, a high sensitivity negative (Shipley XP90104C) resist was chosen and characterized in x-ray lithography experiments so that optimum parameters were established for resist performance and pattern replication. A sensitivity of 6 mJ cm^{-2} and a contrast of 3.3 was determined for this resist using a copper plasma x-ray source. This sensitivity is quite high compared to the existing resists. The measured experimental results were then used to determine the resist parameters for an x-ray lithography simulation code called XD3. The code was used to predict the experimentally measured lineshapes for various conditions. Both the measured and simulated results agreed reasonably well with each other. In particular it has been demonstrated that very sensitive resists with sensitivity of 6 mJ cm^{-2} can be used in x-ray lithography for producing very fine line structure. A resolution down to $0.1 \text{ }\mu\text{m}$ has been demonstrated with an aspect ratio of 14 to 1. The estimated throughput using an optimized exposure station and the high sensitivity XP90104C resist is about 4 wafers (8" in diameter) per hour which could potentially be improved several times by employing more powerful excimer lasers and improving the x-ray conversion efficiency of the laser system.

Modelling calculations show that one can reduce the exposure dose and increase the exposure latitude by choosing a suitable bias. The exposure dose is less for the laser plasma x-ray source than the synchrotron x-ray source for the same biasing condition. The exposure latitude for laser plasma and synchrotron x-ray source are around 20 % depending on the bias for a mask to wafer gap in the range of 10 to $15 \text{ }\mu\text{m}$ in order to remain within 10 % tolerance of the $0.25 \text{ }\mu\text{m}$ linewidth. For $0.1 \text{ }\mu\text{m}$ linewidth, the exposure latitude is reduced to about 5 % for both laser plasma and synchrotron x-ray sources. This means tight control of both exposure and mask to wafer gap is required for feature sizes of $0.1 \text{ }\mu\text{m}$.

There were a number of difficulties in this project which should be overcome in the future. The major difficulty came from the mask. There were no masks suitable for our proximity x-ray lithography tests available commercially. The masks used were free standing gold gratings which were not perfectly flat. Furthermore, the cross-section of the gold bar is slightly rounded so that x-rays could penetrate through the edge region of the bars. This could lead to some discrepancy in the simulation of experimental results. A technique using the electron microscope located at the Alberta Microelectronic Center as an e-beam writing tool is under development to make the x-ray masks. In addition, there was no accurate control of the mask to wafer gap, an alignment system to measure the exact mask to wafer gap should be used for future work. The modelling code is still not complete since it did not take both the diffusion of the catalyst and phase shift of the leakage x-ray spectrum into consideration. These may introduce some modifications into the calculated results.

In summary, this project demonstrated the feasibility of using an inexpensive, small scale x-ray lithography system employing a laser-plasma source to produce patterns in resist down to 0.1 μm linewidth. The throughput can potentially be quite reasonable because of the high speed x-ray resist (Shipley XP90104C) which has been characterized in terms of its etch rate, contrast and sensitivity.

References

1. W. Arden, "Optical versus X-ray lithography for future device fabrication", *Microelectronic Engineering*, volume 13, pp.231-241 (1991).
2. D.J. Elliott, "Microlithography: process technology for IC fabrication", McGRAW-Hill Book, New York (1986).
3. R. Henderson, "Electron beam technology in microelectronic fabrication", Academic Press, p.200 (1980).
4. L. Geppert, "The new contenders - Not your father's CPU", *IEEE Spectrum*, December, pp.20-25 (1993).
5. W.M. Moreau, "Semiconductor lithography: Principles, Practices, and Materials", Plenum Press, New York, p.3 (1988).
6. M.J. Bowden, "A perspective on resist materials for fine line lithography", *ACS Symposium Series*, volume 266, p.39 (1984).
7. L.F. Thompson, "An introduction to lithography", *ACS Symposium Series*, volume 219, p.9 (1983).
8. G. Zorpette, "Rethinking x-ray lithography", *IEEE Spectrum*, June, pp.33-36 (1992).
9. H.I. Smith and M.L. Schattenburg, "Why bother with x-ray lithography", *SPIE* volume 1671, pp.282-298 (1992).
10. H.I. Smith, K.Ismail, M.L. Schattenburg and D.A. Antoniadis, "Sub-100 nm electronic devices and quantum-effects research using x-ray nanolithography", *Microelectronic Engineering*, volume 11, pp.53-59 (1990).
11. H.I. Smith and M.L. Schattenburg, "X-ray lithography, from 500 to 30 nm: X-ray nanolithography", *IBM Journal of Research and Development*, volume 37, number 3, pp 319-329 (1993).

12. E. Spiller, "Physics, Fabrication, and Applications of Multilayered Structures, edited by P. Dhez and C. Weisbuch", Plenum, New York, p.271 (1987).
13. J.H. Underwood, "The renaissance of x-ray optics", Physics Today, April, pp.44-51 (1984).
14. J.E. Bjorkholm, J. Bokor, L. Eichner, R.R. Freeman, J. Gregus, T.E. Jewell, W.M. Mansfield, A.A. MacDowell, E.L. Raab, W.T. Silfvast, L.H. Szeto, D.M. Tennant, W.K. Waskiewicz, D.L. White, D.L. Windt, O.R. Wood and J.H. Bruning, "Reduction imaging at 14 nm using multilayer-coated optics: Printing of features smaller than 0.1 μm ", J. Vac. Sci. Technol. B8 (6), pp.1509-1513 (1990).
15. M.A. Kumakhov and F.F. Komarov, "Multiple reflection from surface x-ray optics", Physics Reports, volume 191, No. 5, pp.289-350 (1990).
16. M. Vartanian, D. Gibson, R.D. Frankel and J. Drumheller, "Development of a polycapillary collimator for point source x-ray lithography", SPIE volume 1924, pp.335-345 (1993).
17. D.W. Berreman, J.E. Bjorkholm, L. Eichner, R.R. Freeman, T.E. Jewell, W.M. Mansfield, A.A. MacDowell, M.L. O'Malley, E.L. Raab, W.T. Silfvast, L.H. Szeto, D.M. Tennant, W.K. Waskiewicz, D.L. White, D.L. Windt and O.R. Wood II, "Soft-x-ray projection lithography: printing of 0.2 μm features using a 20:1 reduction", Optics Letters, volume 15, pp.529-531 (1990).
18. D.L. White et al., " Soft X-ray Projection Lithography with 20x Reduction and 0.1 μm Resolution", SPIE volume 1343, pp.204-213 (1991).
19. B.E. Newman, " Development of xuv projection lithography at 60-80 nm ", SPIE volume 1671, pp.419-436 (1992).
20. V.K. Viswanathan, " Practical tolerancing and performance for XUV projection lithography reduction steppers ", SPIE volume 1671, pp.437-441 (1992).

21. J.E. Bjorkholm, J. Bokor, L. Eichner, R.R. Freeman, J. Gregus, T.E. Jewell, W.M. Mansfield, A.A. MacDowell, M.L. O'Malley, E.L. Raab, W.T. Silfvast, L.H. Szeto, D.M. Tennant, W.K. Waskiewicz, D.L. White, D.L. Windt and O.R. Wood, "Experiments in projection lithography using soft x-rays", *Microelectronic Engineering*, volume 13, pp.243-250 (1991).
22. M. Feldman, "Alignment techniques in optical and x-ray lithography", *VLSI Electronics: Microstructure Science*, volume 16, p.232 (1987).
23. S. Okazaki, "Comparison of optical, x-ray electron and ion beam lithography", *Microelectronic Engineering*, volume 9, pp.297-304 (1989).
24. S. Okazaki, "Lithographic technologies for future ULSI", *Applied Surface Science*, volume 70/71, pp.603-612 (1993).
25. M.D. Levenson, N.S. Viswanathan and R.A. Simpson, "Improving resolution in photolithography with a phase-shifting mask", *IEEE Trans. Electron Devices*, volume ED-29, No. 12, pp.1828-1836 (1982).
26. Y.C. Ku, E.H. Anderson, H.I. Smith and M.L. Schattenburg, "Use of a pi-phase shifting x-ray mask to increase the intensity slope at feature edges", *J. Vac. Sci. Technol. B*, volume 6, Jan/Feb, pp.150-153 (1988).
27. J. Lamb and M.G. Moss, "Expanding Photolithography Process Latitude with Organic AR Coatings", *Solid State Technology*, September, pp.79-83, (1993).
28. K.A. Cooper, "Why should IC makers pursue x-ray lithography", *Karl Suss Report Q3*, pp.5-7 (1991).
29. K. Early and W.H. Arnold, "Cost of ownership for x-ray proximity lithography", *SPIE volume 2194*, pp.22-33 (1994).
30. G.E. Flores and B. Kirkpatrick, "Optical lithography stalls x-ray", *IEEE Spectrum*, October, pp.24-27 (1991).

31. D.L Spears and H.I. Smith, "X-ray lithography - A new high resolution replication process", Solid State Technology, July, pp.21-26 (1972).
32. R.K. Watts, "X-ray lithography", VLSI Handbook Chapter 21, Academic Press, New York, pp.365-380 (1985).
33. J.R. Maldonado, "X-ray lithography, where it is now, and where it is going", Journal of Electronic Materials, volume 19, number 7, pp.699-709 (1990).
34. D.J. Nagel, "Comparison of x-ray sources for exposure of photoresists", Annals of the New York Academy of Sciences, volume 342, p.235-251 (1980).
35. K. Nguyen, D. Attwood and T.K. Gustafson, "Sources issues relevant to x-ray lithography", OSA Proceedings on Soft-X-Ray Projection Lithography, volume 11, pp.62-67 (1991).
36. D.J. Nagel, "Plasma sources for x-ray lithography", VLSI Electronics: Microstructure Science, Volume 8, Chapter 6, pp.137-170 (1983).
37. J. Matsui, "Use of synchrotron radiation for x-ray lithography and semiconductor materials characterization", Vacuum volume 41, number 4-6, pp.996-1002 (1990).
38. V.H. Pitt, "The Penguin Dictionary of Physics", Penguin books, England, p.371 (1984).
39. E.M. Rowe, C.J. Sparks, H. Winick, G. Brown, K. Halbach, J. Harris, D.E. Eastman and F.J. Himpsel, "Special issue: synchrotron radiation", Physics Today, May, pp.27-72 (1981).
40. M. Chaker, S. Boily, B. Lafontaine, J.C. Kieffer, H.Pepin, I. Toubhans and R. Fabbro, "X-ray wavelength optimization of the laser plasma x-ray lithography source", Microelectronic Engineering, volume 10, pp.91-105 (1990).
41. I.H. Hutchinson, "Principles of plasma diagnostics", Cambridge University Press, Cambridge, (1990).

42. R. Bobkowski and R. Fedosejevs, "Debris emission from laser plasma x-ray sources", Canadian Association of Physicist Annual Congress, Regina, June 26-29, (1994).
43. R.K. Watts and J.R. Maldonado, "X-ray lithography", VLSI Electronics : Microstructure Science, Volume 4, p.71 (1982).
44. E. Bassous, R. Feder, E. Spiller and J. Topalian, "High transmission x-ray masks for lithographic applications", Solid state technology, September, pp.55-58 (1976)
45. M. Chaker, S. Boily, Y. Diawara, M.A. El Khakani, E. Gat, A. Jean, H. Lafontaine, H. Pepin, J. Voyer and J.C. Kieffer, "X-ray mask development based on SiC membrane and W absorber", J. Vac. Sci. Technol. B 10 (6), pp.3191-3195 (1992).
46. F. Cerrina, "Short Course Notes - X-Ray Lithography", SPIE 1994 Symposium on Microlithography, 27 February - 4 March 1994, San Jose, California USA (1994).
47. M.J. O'Brien and D.S. Soane, "Resists in microlithography", Microelectronics processing: Chemical Engineering Aspects, Chapter 7, pp.325-376 (1989).
48. C.G. Willson, "Organic resist materials - Theory and chemistry", ACS Symposium Series, volume 266, p.90 (1984).
49. J. Lingnau, R. Dammel and J. Theis, "Recent trends in x-ray resists: Parts I and II", Solid State Technology, pp.105-112, September (1989), and pp.107-111, October (1989).
50. R.C. Bracken and S.A. Rizvi, "Resist technology in VLSI device processing", VLSI Handbook, Chapter 19, Academic Press (1985).
51. M.J. Bowden, "A perspective on resist materials for fine line lithograph", ACS Symposium Series, volume 266, pp.43-47 (1984).
52. G.N. Taylor, "Guidelines for publication of high resolution resist parameters", Solid State Technology, June, pp.105-110 (1984).

53. W.B. Glendinning and J.N. Helbert, "Handbook of VLSI Microlithography - Principles, Technology and Applications", Noyes Publications, New York (1991).
54. G. Owen, "Introduction to Electron-Beam Lithography", Short course - SPIE's 1994 Symposium on Microlithography, Feb (1994).
55. E.D. Roberts, "Recent developments in electron resists", Solid State Technology, June, pp.135-141 (1984).
56. W.M. Moreau, "State of art of acrylate resists: an overview of polymer structure and lithographic performance", Optical Engineering, Volume 22, Number 2, pp.181-184 (1983)
57. H.S. Choong and F.J. Kahn, "Molecular parameters and lithographic performance of poly(chloromethylstyrene) - a high-perfromance negative electron resist", J. Vac. Sci. Technol., volume 19, pp.1121-1126 (1981).
58. J. Pacansky and J. Lyeila, "Photodecomposition mechanisms for AZ-type photoresists," IBM Jour. Res. Dev., volume 23, number 1, pp.42-55 (1979).
59. D. Seligson, "The impact of high sensitivity resist materials on x-ray lithography", J. Vac. Sci. Technol. B6, pp.2268-2273 (1988).
60. M. Weiss, H. Oertel and H.L. Huber, "Influence of phase shift on pattern transfer in x-ray lithography", Microelectronic Engineering, volume 6, pp.265-271 (1987).
61. D.H. Ziger, "Generalized characteristic model for lithography: application to negative amplified resists", Optical Engineering, volume 31, pp.98-104 (1992).
62. R. Fedosejevs, R. Bobkowski, J.N. Broughton and B. Harwood, "keV x-ray source based on high repetition rate excimer laser-produced plasma", SPIE volume 1671, pp.373-382 (1992).
63. M. Chaker, H. Pepin, V. Bareau, B. Lafontaine, I. Toubhans, R. Fabbro and B. Farral, "Laser plasma x-ray source for microlithography", J. Appl. Phys. volume 63, pp.892-899 (1988).

64. Quantrad Corp., Los Angeles, California.
65. R.H. Day, P. Lee, E.B. Saloman and D.J. Nagel, "Photoelectric quantum efficiencies and filter window absorption coefficients from 20 eV to 10 keV", J. Appl. Phys. volume 52, pp.6965-6973 (1981).
66. J.N. Broughton and R. Fedosejevs, "X-ray generation from 50 mJ, 120 ps KrF laser-produced plasma", J. Appl. Phys. volume 71, pp.1153-1162 (1992).
67. B10 filter material, Alexander Vacuum Research, Greenfield, Mass.
68. Shipley Co. Ltd., Newton, Mass.
69. Olin Hunt Specialty Products, East Providence, Rhode Island.
70. W.J. Daughton and F.L. Givens, "An investigation of the thickness variation of spun-on thin films commonly associated with the semiconductor industry", J. Electrochem. Soc. : Solid-State Science and Technology, volume 129, number 1, January, pp.173-179 (1982)
71. C.P. Babcock, J.W. Taylor, M. Sullivan, D. Suh and D. Plumb, "Process latitude measurements on chemically-amplified resists exposed to synchrotron radiation", SPIE volume 1466, pp.64-73 (1991).
72. J.W. Taylor, C.P. Babcock, and D.C. Mancini, "Sensitivity / resolution variables in x-ray chemically amplified resists exposed to synchrotron radiation", J. Vac. Sci. Technol. B8 (6), Nov/Dec, pp.1547-1550 (1990).
73. A.E. Siegman, "Laser", University Science Books, California (1986).
74. H.K. Oertel, M. Weib and H.L. Huber, "Investigation of the process latitude for sub-half-micron pattern replication in x-ray lithography", Microelectronic Engineering, volume 13, pp.339-342 (1991).

75. Karl Suss XRS200 x-ray stepper system.
76. K. Simon, H.-U. Scheunemann, H.-L. Huber and P. Kaiser, "Alignment accuracy improvement by consideration of wafer processing impacts", SPIE volume 2194, pp.63-72 (1994).
77. S. Hamada, K. Ito, T. Miyatake, F. Sato and K. Yamazaki, "22-nm overlap accuracy of synchrotron radiation stepper using an improved chromatic bifocus alignment system", SPIE volume 2194, pp.73-82 (1994).
78. G. Chen et, D. Bodoh, J. Wallace, P. Anderson, M. Reilly, R. Nachman and F. Cerrina, "Implementation of two-state alignment system into CXrL aligner", SPIE volume 1671, pp.471-485 (1992).
79. R. Nachman, G. Chen, M.T. Reilly, G.M. Wells, J.P. Wallace, H.H. Li, A.A. Kraznoperova, P.D. Anderson, E. Brodsky, E. Ganin, S.A. Campbell, J.W. Taylor and F. Cerrina, "X-ray lithography processing at CXrL from beamline to quarter-micron NMOS devices", SPIE volume 2194, pp.106-119 (1994).
80. N. Uchida, O. Kuwabara, Y. Ishibashi, N. Kikuri, R. Hirano, J. Nishida, T. Nishizaka and Y. Kikuchi, "X-ray stepper aiming at 0.2 μm synchrotron orbital radiation lithography", J. Vac. Sci. Technol. B11, pp.2997-3002 (1993).
81. A.D. Feinerman, D.A. Crewe, D.-C. Perng, P.R. Schwoebel and A.V. Crewe, "Miniature electron microscopes for lithography", SPIE volume 2194, pp.262-273 (1994).
82. J.N. Broughton and R. Fedosejevs, "Efficient keV x-ray generation from 50 mJ KrF laser plasma", Applied Physics Letters, Volume 60, Number 15, April, pp.1818-1820 (1992).
83. C. Campell, "Surface acoustic wave devices and their signal processing applications", Academic Press, New York (1989).

84. W.H. Brunger, L.M. Buchmann, M. Kreutzer, M. Torkler, G. Zwicker and B. Fleischmann, "Fabrication of 3.5 GHz surface acoustic wave filters by ion projection lithography", *Microelectronic Engineering* 17, pp.245-248 (1992).
85. P.A. Miller, D.M. Fleetwood and W.K. Schubert, "Damage due to electron, ion and x-ray lithography", *J. Appl. Phys.*, volume 69, pp.489-494 (1991).
86. R. Viswanathan, D. Seeger, A. Bright, T. Bucelot, A. Pomerene, K. Petrillo, P. Blauner, P. Agnello and J. Warlaumont, "Fabrication of high performance 512 K static-random access memories in 0.25 μm complementary metal-oxide semiconductor technology using x-ray lithography", *J. Vac. Sci. Technol. B* 11(6), pp.2910-2919 (1993).

Appendix 1 : Summary of operating procedures for the X-ray Lithography System

A1.1 Laser System

1. Pump out the old laser mixture from the KrF laser module
 - * Open "read vacuum" valve to read very low pressures ONLY IF the main gauge reads ~ 0 psi
2. Fill the KrF laser module with the proper gas mixture:

| Final pressure | F ₂ (5%)+Ne(95%) | Kr(30%)+Ne(70%) | Ne (100%) |
|----------------------------------------|-----------------------------|----------------------|--------------|
| 40 psi (for single shot) | 1.2 psi 62 Torr | 3.6 psi 184 Torr | up to 40 psi |
| 50 psi (for high repetition rate) | 1.5 psi 78 Torr | 4.45 psi 230 Torr | up to 50 psi |
| 60 psi (for high repetition rate) | 1.8 psi 93 Torr | 5.33 psi 276 Torr | up to 60 psi |

Table A1.1 : Proportion of gas mixture in KrF laser module

- * CLOSE the " read vacuum " valve before filling Ne (100 %) gas
3. Close all valves and turn off roughing pump
 4. Turn on water cooling
 5. Turn on laser module power (wait ~ 5 minutes)
 6. Activate the laser system

A1.2 Vacuum Chamber

1. Mount the target and samples in the chamber
 - * SWITCH OFF all lights before opening the sample
2. Close all valves and turn on the roughing pump and evacuate the chamber
 - * Open the small green exhaust pump valve about 1/3 turn first until the pressure is ~ 100 Torr, then open the big metal exhaust pump valve
3. Monitor the pressure reading by a pirani gauge
4. Refill the chamber with Helium and set at constant flow at 640 torr.

A1.3 Computer data acquisition system

1. Turn on the power supply for the three photodiode detectors (One Hamatsu vacuum photodiode (PD9) and two solid state photodiodes (PD13 and PD30)), the bias box of the PIN diode, and target rotation motor.
2. Turn on the power supply of the small trigger unit to the computer (Channel 8 IN)
3. Turn on the power supply of the large laser triggering system and the cooling fan for the power supply unit by plugging it into the power bar
4. Check injection on the Tektronix 7104 oscilloscope by turning off the KrF laser module but turning on the XeCl and dye lasers while blocking the laser beam to the vacuum chamber
5. Computer firing:
 - i. Switch the triggering system to the EXT. (external) mode for computer triggering.
 - ii. Type on the Packard Bell 386 control computer C:> las ↵ (note : las is a batch file which will change to the directory C:\USRS\KEVIN\LASER\LASER 2)
h (help)
S (set parameters)
f (fire the laser)
 - iii. Channel 3 is calibrated to record the x-ray energy at the target
computer conversion factor for Cu = 0.67
computer conversion factor for Fe = 1.74
 - iv. For continuous firing at high repetition rate, press F. One should watch the energy reading and should also ensure injection by adjusting the “ns delay”
 - v. Press space bar to stop. Use print screen to get the hard copy of the exposure parameters

Please refer to the “Users Manual for Operating X-ray Lithography System and Resist processing, by R. Tam” for detailed step by step instructions.

A1.4 X-ray energy at the samples

Converting computer ADCchan 3 total energy at the target to the x-ray flux at the sample;

Let E (mJ)be the total energy recorded in channel 3 in the computer

L (cm)be the distance from target to the sample

T_1 be the transmission of p torr of helium

T_2 be the transmission of B10 filter

Then the x-ray flux \mathcal{F} (mJ cm⁻²)at the sample will be

$$\mathcal{F} = E \times \frac{1}{2\pi L^2} \times T_1 \times T_2 \quad (\text{A1.1})$$

where T_1 and T_2 are given by the following tables:

| Pressure | Target | Helium Transmission T_1 | | | | | |
|----------|--------|---------------------------|--------|--------|--------|--------|--------|
| (torr) | | 3 cm | 4 cm | 5 cm | 6 cm | 7 cm | 8 cm |
| 600 | Cu | 0.9798 | 0.9731 | 0.9665 | 0.9599 | 0.9535 | 0.9470 |
| 640 | Cu | 0.9784 | 0.9713 | 0.9643 | 0.9574 | 0.9505 | 0.9436 |
| 700 | Cu | 0.9764 | 0.9687 | 0.9611 | 0.9535 | 0.9459 | 0.9385 |
| 760 | Cu | 0.9744 | 0.9660 | 0.9578 | 0.9521 | 0.9415 | 0.9334 |

Table A1.2 : Transmission of Helium for copper spectrum

| | Transmission T_2 | | |
|--------|--------------------|------|------|
| Target | B10 | 2B10 | 4B10 |
| Cu | 0.67 | 0.46 | 0.21 |

Table A1.3 : Transmission of B10 filter for copper spectrum

A1.5 X-ray transmission program

The x-ray transmission program xresp is used to calculate the combined transmission of a source spectrum through thin filters. For example : To find the transmission of 4 cm of He at 600 Torr to the Cu spectrum type:

C: \filter> xresp ↵

ENTER INDEX TO CHOOSE NEXT DESIRED COMPONENT

- 1 - FILTER USING CUBIC FIT TABLES
- 2 - FILTER USING INPUT ABSORPTION COEF FILE
- 3 - MIRROR/FILTER USING TRANSMISSION FILE
- 4 - INPUT SPECTRUM FILE
- 5 - OUTPUT RESPONSE FUNCTION
- 6 - DISPLAY RESPONSE FOR ONE ENERGY
- 7 - QUIT

2 ↵

ENTER NAME OF FILTER/RESPONSE FILE (no quotes)

hema01.txt ↵

ENTER FILTER THICKNESS IN mg/cm²

(density of He = 0.1785 g/l at NTP, i.e. at 760 Torr

$$= 178.5 \text{ mg/1000 cm}^3$$

$$= 0.1785 \text{ mg/cm}^2 \text{ for 1 cm column at 760 torr}$$

$$= 0.1785 \times \frac{600}{760} \text{ mg/cm}^2 \text{ for 1 cm column at 600 torr}$$

$$= 0.1409 \text{ mg/cm}^2 \text{ for 1 cm column at 600 torr}$$

$$= 0.5636 \text{ mg/cm}^2 \text{ for 4 cm column at 600 Torr)}$$

0.5636 ↵

ENTER INDEX TO CHOOSE NEXT DESIRED COMPONENT

- 1 - FILTER USING CUBIC FIT TABLES
- 2 - FILTER USING INPUT ABSORPTION COEF FILE
- 3 - MIRROR/FILTER USING TRANSMISSION FILE
- 4 - INPUT SPECTRUM FILE
- 5 - OUTPUT RESPONSE FUNCTION
- 6 - DISPLAY RESPONSE FOR ONE ENERGY
- 7 - QUIT

4 ↵

ENTER NAME OF FILTER/RESPONSE FILE (no quotes)

cu02.tgt ↵ (or fe01.tgt)

ENTER INDEX TO CHOOSE NEXT DESIRED COMPONENT

- 1 - FILTER USING CUBIC FIT TABLES
- 2 - FILTER USING INPUT ABSORPTION COEF FILE
- 3 - MIRROR/FILTER USING TRANSMISSION FILE
- 4 - INPUT SPECTRUM FILE
- 5 - OUTPUT RESPONSE FUNCTION
- 6 - DISPLAY RESPONSE FOR ONE ENERGY
- 7 - QUIT

5 ↵

ENTER NAME OF OUTPUT FILE (no quotes)

cuhe4cm.out ↵

ENTER INDEX TO CHOOSE NEXT DESIRED COMPONENT

- 1 - FILTER USING CUBIC FIT TABLES
- 2 - FILTER USING INPUT ABSORPTION COEF FILE
- 3 - MIRROR/FILTER USING TRANSMISSION FILE
- 4 - INPUT SPECTRUM FILE
- 5 - OUTPUT RESPONSE FUNCTION
- 6 - DISPLAY RESPONSE FOR ONE ENERGY
- 7 - QUIT

7 ↵

ARE YOU SURE YOU WANT TO QUIT Y/N ?

y ↵

STOP - PROGRAM TERMINATED

The program xdisp is used to plot the resultant spectral files and calculate the area under the curves.

C:\filter> xdisp ↵

ENTER INPUT FILE NAME (no quotes)

cuhe4cm.out ↵

The area under the spectrum = 16247

C:\filter> xdisp ↵

ENTER INPUT FILE NAME (no quotes)

cu02.tgt ↵

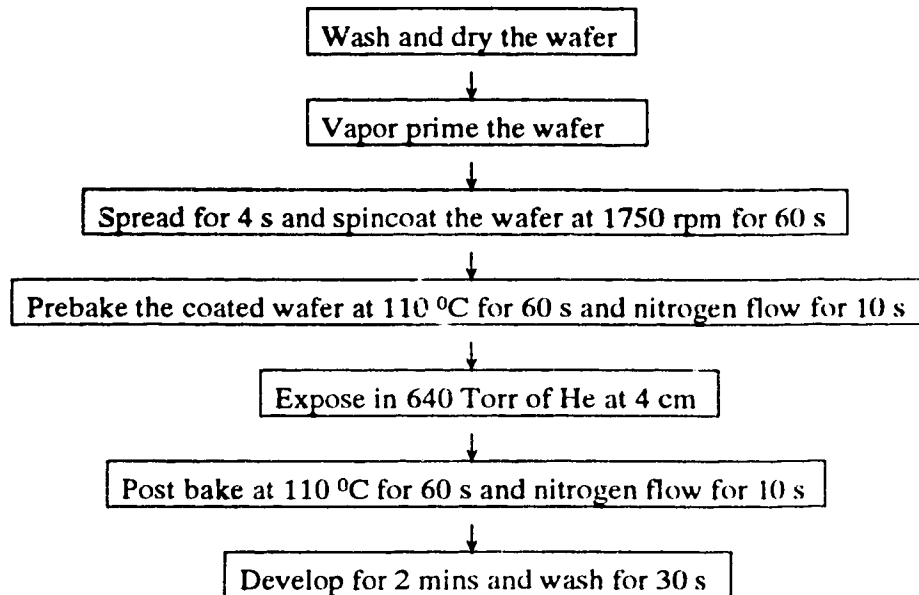
The area under the spectrum = 16696

$$\therefore \text{transmission} = \frac{16247}{16696} = 0.9731$$

Appendix 2 : Resist Exposure and Processing

A2.1 Flowchart summary of the lithographic processing

The lithographic processing is done in the fabrication laboratory of the second floor of the Alberta Microelectronic Center (AMC).



A2.2 Substrate Cleaning

1 Washing of the wafer

- i. **Turn on the flow of water and nitrogen** for spin rinse dryer (ST1) at the backroom of the fabrication lab.
- ii. Choose the **Auto mode** (Main/Off/Auto) of the **Semitool PCM 328** in the **“Wet Etch” Laboratory room**.
- iii. **Turn on the power** and wait for about 10 seconds to open the door of the Semitool PCM 328.
- iv. Put the wafer in the plastic cabinet and close the door.
- v. Adjust the **“Rinse time”** to **120 seconds at 800 rpm**.
- vi. Adjust the **“Dry 1 time”** to **80 seconds at 2700 rpm**.
- vii. Adjust the **“Dry 2 time”** to **40 seconds**.
- viii. **Press “START”** to activate the washing and drying process.

2 Vapor prime process

The vapor prime process is performed by using the Yield Engineering Systems' LP-III in the "Photolithography" Laboratory room, which is a vacuum bake/vapor prime system to help in making photoresist adhere to a variety of thin film structures.

- i. **Transfer the wafer into a metal cassette.**
- ii. **Add a dump wafer at the front and back of each cassette.**
- iii. **Load a maximum of 4 cassettes into the system horizontally on the top shelf only.**
- iv. **Oven temperature must be $150^{\circ}\text{C} \pm 1^{\circ}\text{C}$.**
- v. **Press "START" to start the pre-programmed process:**
- vi. **The whole process takes about 36 minutes.**
- vii. **"Complete" light turns on when finish.**
- viii. **Press "Reset" to stop.**
- ix. **Wafers must sit to cool for at least 10 minutes and must be spun within 2 hours.**

A2.3 Spincoat of the resist on the wafer

A negative resist, XP90104C is spun at a speed of 1750 rpm or 6400 rpm for 60 s to achieve a film thickness of either $1.4\text{ }\mu\text{m}$ or $0.7\text{ }\mu\text{m}$ on silicon wafer. The average final film thickness as a function of final spin speed for the Shipley 90104C resist is shown in Figure 2.1.

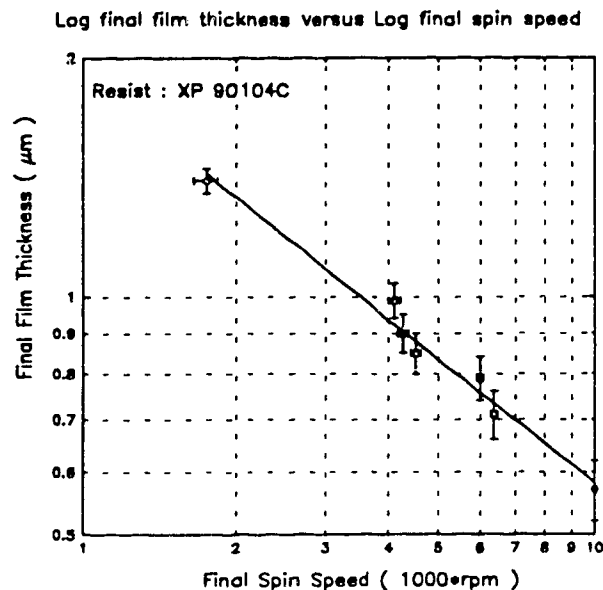


Figure A2.1 : Dependence of resist thickness on the spin speed

- i. In the “photolithography” laboratory room, wrap the two pieces of plastic cover of the centrifuge with aluminum foil.
- ii. **Turn on the power of the centrifuge.**
- iii. **Turn on the nitrogen flow.**
- iv. Use the wafer twister to take the wafer from the box (make a record on the box) and use the semi-circular arc holder to **center the wafer on the metallic platform of the centrifuge.**
- v. **Press “VACUUM”** to suck the wafer on the platform.
- vi. **Press “SPIN”** to turn it on and adjust it to **30 seconds** (maximum time limit) for half the time spin of the wafer.
- vii. **Press “SPREAD”** to turn it on and adjust it to **4 seconds** for the time of the slow rotation of the wafer for spreading of the resist solution.
- viii. **Press “START”** to start spinning and adjust the speed to **1750 rpm** for thick resist or **6400 rpm** for thin resist.
- ix. When the centrifuge stops, **transfer the resist solution on the wafer using a dropper or syringe.** Use as little as possible, ~ 1 - 2 ml (the excess will be spun off the wafer edge and wasted).
- x. **Press “START”** to start spinning.
- xi. It will stop after 30 seconds. **Press “SPREAD”** again to turn it off and then press **“START”** to **restart the spinning for another 30 seconds.**
- xii. **Press “VACUUM”** to turn it off and put the wafer in a wafer container for the next step.

A2.4 Prebake of the resist coated wafer

The XP90104C resist is prebaked at a temperature of 110°C for 60 seconds.

- i. **Turn on the power of the Solitec vacuum hot plate in the “photolithography” laboratory room.**
- ii. **Turn on the nitrogen flow valve.**
- iii. Open the cover of the vacuum hot plate and put the resist coated wafer on the hot plate and then close the cover.
- iv. Adjust the **pre-exposure bake time to 60 seconds.**
- v. Adjust the **nitrogen flow time to 10 seconds.** (nitrogen will flow for 10 seconds after 60 seconds of prebake, then the alarm will be heard when finish.)
- vi. Adjust the **bake temperature to 110°C .**
- vii. **Press “START”** to start the pre-exposure bake.
- viii. **Press “START”** again when finished.

A2.5 Exposure of the resist

Refer to Appendix 1.

A2.6 Post-exposure bake of the exposed resist

The XP90104C resist was post-baked at 110 °C for 60 s in the vacuum hot plate as in section 2.4.

A2.7 Development of the Shipley 90104C resist

After exposure, XP90104C resist is developed in MF-312 developer for 2 minutes and rinsed in water for 30 s and then dried in nitrogen gas.

- i. Use a high precision twister to hold the exposed resist and rinse in the developer for 2 minutes in the “photolithography” laboratory room.
- ii. Wash the developed resist in water for 30 seconds.
- iii. Dry the wetted resist in nitrogen.

A2.8 Measurement of the thickness of the resist

1. Turn on the power of the profilometer in the “Metal Deposition” laboratory room.
2. Press table down “↓” to lower the platform and put the developed resist on it.
3. Rotate the platform so that the needle is right above the sample.
4. Press table up “↑” continuously to raise the platform until the needle line moves up on the screen.
5. Adjust the platform so that the needle can scan across the pattern on the resist.
6. Press table down “↓” to check the alignment of the sample and press “START” when ready.
7. Rescale the plot:
 - I) Press “LEVEL” and then press “←” or “→” to define one position for one level.
 - ii) Press “CUR” to move the other cursor and again press “←” or “→” to define another position of the same level.
 - iii) Press “ENT” to resume the change.
8. Press “PRINT” to get the printout.

Appendix 3 : Explanation of Parameter files of XD3 modelling code

The program XD3 contains three parameter files: xdepos.par, xprof.par and xetch.par for the three sub-programs xdepos, xprof and xetch respectively. All parameters in each parameter file must be chosen properly in order to simulate various experimental conditions and run the program. The parameter files are duplicated below with the explanation written inside the brackets.

A3.1 Explanation for the x-ray deposition parameter file (xdepos.par)

XP, Cu Spec, 4cm He, 0.25/2.0 Au/2B10

(Title of the graph : XP is the type of resist. Cu is the source spectrum. 4cm is the distance from plasma to resist. He is the working gas. 0.25 and 2.0 are the multiplication factors for the pre-assigned standard (all files are assumed to give transmission of 1 μm thick layers) of the mask and filter, i.e. 0.25 μm of gold and 4 layers of B10 filter.)

1 vgdemn iswplt and plotfile name

(1 is the number of iswplt : 1 — autoscaled linear plot, 2 — user scaled linear plot, 3 — autoscaled with $y_{\min} = 0$; vgdemn is the filename (vgdemn01.POS, vgdemn02.POS,..., m,n = 0, 1, .., 9) for storing the output graph. Different parameter files should have different plotfile names; iswitch plot is a plot control switch but is not used in this parameter file.)

cu02.tgt

(cu02.tgt is the target source spectrum data file.)

2 mask substrate and filter layers:

(2 is the number of layers from the laser produced plasma x-ray source to the resist.)

0.32 he10cm01.txt

(0.32 is the multiplication factor for the first layer encountered, he10cm01.txt is the text filename of the first layer encountered by the x-ray.

e.g. resist is at 4cm from the plasma and in 600 torr of flowing helium;

text file is 10 cm of helium at 1 atmosphere (760 torr) :

$$\therefore \text{multiplication factor} = \frac{4}{10} \times \frac{600}{760} = 0.32)$$

2.0 twob1001.txt

(2.0 is the multiplication factor for the second layer. twob1001.txt is the filename of the second layer encountered by the x-rays.

Note that the filename must begin with a letter (i.e. 2b1001.txt is not a valid filename).

e.g. 4 layers of b10 filter and the text file is for two layers of b10 filters :

∴ multiplication factor = $4/2 = 2$.)

1 mask opaque metal layers:

(1 is the number of mask opaque metal layers.)

0.25 au1um02.txt

(0.25 is the multiplication factor for the mask thickness; au1um02.txt is the transmission text file for 1 µm of gold.)

2 resist and wafer layers:

(2 is the number of resist and wafer layers.)

1.4 xp1um.txt

(1.4 is the multiplication factor for the resist thickness. xp1um.txt is the transmission file for 1µm of Shipley 90104C negative resist, i.e. the resist is 1.4 µm thick.)

1.0 si1um.txt

(1.0 is the multiplication factor for the wafer thickness. si1um.txt is the transmission file for 1µm of silicon wafer, i.e. the wafer is 1 µm thick.)

A3.2 Explanation for the x-ray diffraction parameter file (xprof.par)

&INITNL

(& is a special read statement and NL means namelist. INIT is the name for the namelist. They assign the same name for the variables used in the program and in the parameter file.)

runtit='XP, Copper Target, Au/SiC mask'

(use the title 'XP, Copper Target, Au/SiC mask' for the output graph.)

fmnpr='xprof.out'

(output the diffraction distribution to the file 'xprof.out'.)

fmnsp='xmnspec.out'

(input the spectrum 'xmnspec.out' as the main input spectrum.)

fhcplt='vgprmn'

(store the output graph in the filename vgprmn01.POS.)

d1=4.d4

(d1 is the distance from plasma to the surface of the mask in microns. It should be consistent with the length of helium in the xdepos.par file, i.e. $4 \times 10^4 \mu\text{m} = 4 \text{ cm.}$)

d2=10

(d2 is the distance from the bottom surface of mask to the resist, $10 \mu\text{m}$)

xlam=1.d0

(xlam is the wavelength of the x-rays when a binned spectrum is not chosen using iswspc as described below.)

srcdia=20.0

(srcdia is the diameter of the plasma source in μm (20 for Cu and Fe).)

x1=0.d0

(x1 is the starting position of the output field, in μm)

x2=1.25d0

(x2 is the ending position of the output field, $1.25 \times 10^0 = 1.25 \mu\text{m}$)

nx=1001

(nx is the number of output points, the bigger the nx, the better the resolution but longer the run time.)

nslit=4

(nslit is the number of slits opening in the mask, i.e. there are 4 slits opening)

iswplt=1

(iswplt turns on(1) or off(0) the screen plot of the Fresnel diffraction pattern.)

ihcplt=1

(ihcplt turns on(1) or off(0) the screen plot of the energy density contours plot)

iswspc=1

(iswspc turns on(1) or off(0) the calculation of the 10 frequency weighting bins. If

iswspc = 0 only the average x-ray wavelength given by the parameter xlam is used.)

slit = 0.25 0.75 1.25 0.0 0.0 0.0 0.0 0.0 0.0 0.0 (Start position of slit opening, μm)

0.50 1.00 1.50 0.0 0.0 0.0 0.0 0.0 0.0 0.0 (End position of slit opening, μm)

(e.g. 2000 $\text{\AA}/\text{mm}$ gold grating : thickness of (bar + space) = $1/2000 \text{ mm} = 0.5\mu\text{m}$

thickness of a bar or space = $0.25\mu\text{m}$

\therefore slit opening at every $0.25 \mu\text{m}$ interval)

&end

(end statement)

A3.3 Explanation for the x-ray development parameter file (xetch.par)

&initnl

runtit='XP etch test run'

fprof='xprof.out'

(diffraction deposition profile across the surface)

fmndep='xmndep.out'

(deposition profile into resist/substrate from main radiation spectrum)

flkdep='xlkdep.out'

(deposition profile into resist/substrate from leakage radiation spectrum)

fresis='resist.txt' (dissolution versus energy deposition values for the resist)

fhcplt='vgetmn' (file name header for the plot output files)

iswprt=0 (turns on(1) or off(0) the printing of dissolution rate at a fixed value of x)

iswplt=1 (turns on(1) or off(0) the resist profile screen plot)

iswcon=1 (turns on(1) or off(0) the energy contour screen plot)

iswtrp=1

(turns on(1) or off(0) routine to handle converging sets of triple points on the development front)

iswisl=0 (turns on(1) or off(0) the island checking subroutine)

ihcplt=1 (saves (1) all or does not save (0) the output plots to files)

xmin= 0. (start output field x-coordinate in μm)

xmax= 1.25 (end output field x-coordinate in μm)

ymin= 0. (start output field y-coordinate in μm)

ymax= 2.0 (end output field y-coordinate in μm)

nx= 100 (number of output points in the x direction)

ny= 100 (number of output points in the y direction)

ntstep=1100 (number of time steps)

delt=0.05 (time step Δt in s; $\text{ntstep} \times \text{delt}$ = total run (development) time)

resdev=.01

(resolution parameter in μm , $0.01\mu\text{m}$ is generally fine enough)

itrack=30

(number of points surrounding the etch front in checking for etch cross-over)

rdepth=1.0

(resist depth in μm , which must be consistent with that in the parameter file **xdepos.par**)

moddev=2

(development model:

1- development proceeds along the y direction only, and the etching is quite stable.

2- development moves perpendicular to the current surface with island checking.)

modres=3

(resist model: 1- straight line, 2-values in the file 'fresis', 3- positive resist rate model,

4- negative resist)

esourc=60.0

(energy flux (mJ cm^{-2}) at the resist without any attenuation:

transmission of 4B10 filter for Cu target = 0.21

transmission of 640 torr of He for Cu target at 4 cm = 0.9713

\therefore energy at the resist = $0.2040 \times \text{esourc}$)

devrmn=0.0005

(minimum development rate without exposure [$\mu\text{m/s}$]: 0.0005, etching rate increases slightly with devrmn)

devrmx=0.010

(maximum development rate without exposure [$\mu\text{m/s}$]: .005-.02 etching rate increases largely with devrmx)

devrcl=0.0075

(development rate just to clear the resist = $\frac{\text{resist thickness}}{\text{development time}} \mu\text{m/s}$)

devecl=2.0

(dose to just clear the resist in the development period, [J cm^{-3}]

i.e. the dose to give correct intercept at zero thickness)

devn=20.0

(n parameter in resist models, which typically controls the contrast factor)

deveth=50.0

(threshold energy in J cm^{-3} . It is related to the sensitivity of the resist: the more sensitive the resist, the smaller the value of deveth.)

tout=1. 5. 10. 15. 20. 0. 0. 0. 0. 0.

(output time in seconds for the simulated resist profiles)

&end

(end of the program)